https://doi.org/10.1016/j.cej.2023.147098

Revolutionizing Material Design for Protonic Ceramic Fuel Cells: Bridging the Limitations of Conventional Experimental Screening and Machine Learning Methods

Idris Temitope Bello[a], Daqin Guan[a], Na Yu[a], Zheng Li[a], Yufei Song[b], Xi Chen[a], Siyuan Zhao[a], Qijiao He[a], Zongping Shao [c,]*, Meng Ni[a,]*

[a]Department of Building and Real Estate, Research Institute for Sustainable Urban Development (RISUD) & Research Institute for Smart Energy (RISE), The Hong Kong Polytechnic University, Hung Hom, Kowloon, Hong Kong, China

[b]Department of Mechanical and Aerospace Engineering, The Hong Kong University of Science and Technology, Clear Water Bay, Hong Kong, China

[c]WA School of Mines: Minerals, Energy and Chemical Engineering, Curtin University, Perth, Western Australia, 6845, Australia.

*Corresponding authors: meng.ni@polyu.edu.hk; shaozp@njtech.edu.cn

Highlights

- Proposed statistical EDP approach efficiently develops PCFC cathode materials.
- EDP determines optimal composition with minimal data and experiments.
- EDP optimizes BCCFY and BSCF compositions to achieve excellent ORR and stability.
- EDP identifies the interaction between Co & Ce and Ba & (Co or Fe or Sr) to enhance ORR.

Graphical Abstract

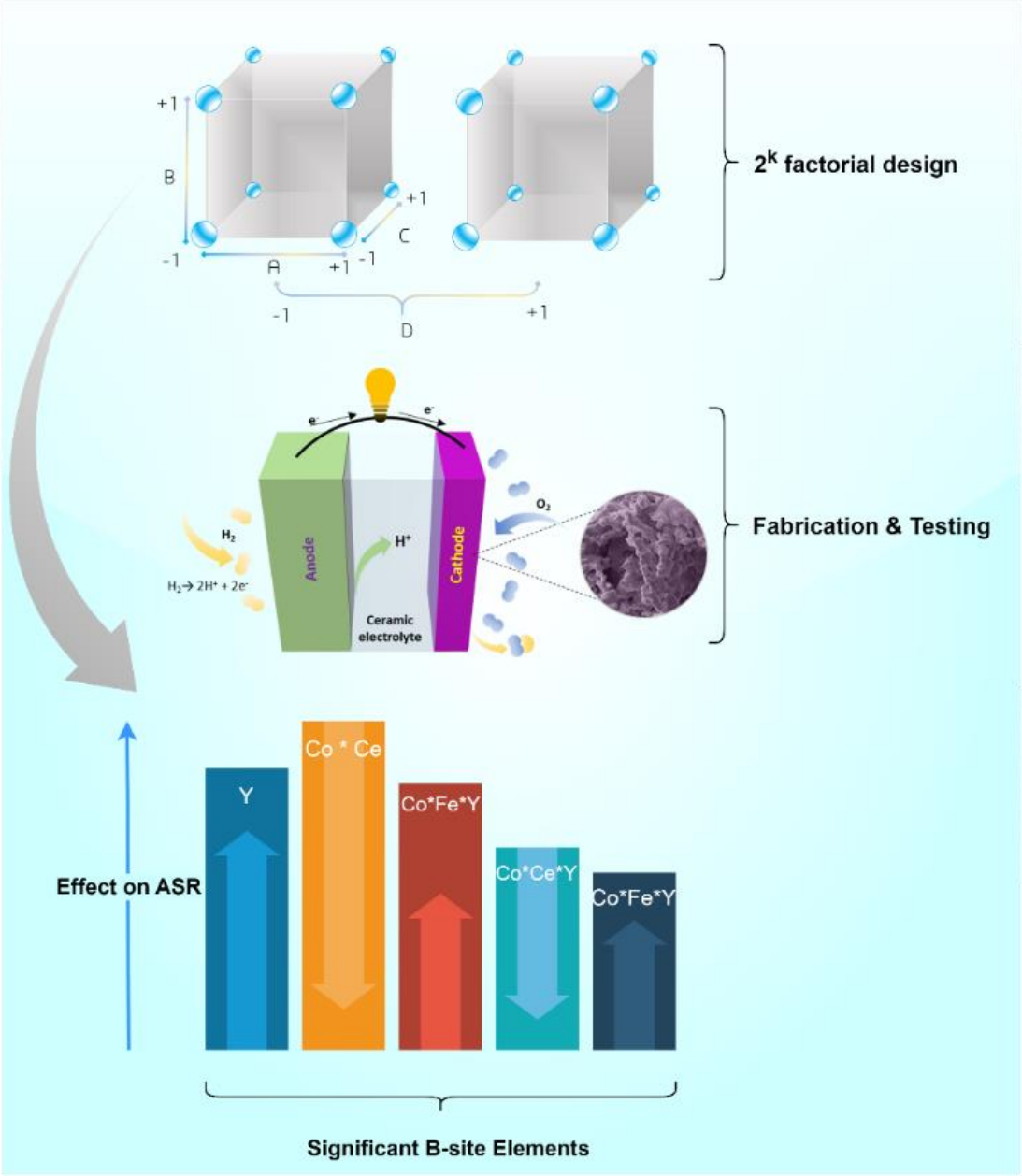

A novel Experimental Design Paradigm (EDP) was introduced to design cathode materials for ceramic fuel cells. A 2^k factorial design was implemented to optimize and determine the elements-ORR performance relationships in $BaCo_{\alpha}Ce_{\beta}Fe_{\gamma}Y_{\zeta}O_{3-\delta}$ (BCCFY) and $Ba_{\alpha}Sr_{\beta}Co_{\gamma}Fe_{\zeta}O_{3-\delta}$ (BSCF) cathode materials. The interaction between Co & Fe, and Y were found to be significantly detrimental to ORR, while the interaction between Co & Ce and Ba & (Co or Fe or Sr) were found to promote ORR significantly.

Abstract

The commercial viability of protonic ceramic fuel cells (PCFCs) is contingent upon developing highly active and stable cathode materials. The conventional trial-and-error process is time-consuming and costly for cathode material development, while the availability of sufficient and reliable datasets limits the recently emerging machine learning (ML) method. Here, we propose a novel approach based on the experimental design paradigm (EDP) to efficiently facilitate PCFC cathode materials' development with a minimal dataset. As a rigorous systematic statistical approach, we employ the EDP for strategic variation of multiple elements and measure their effect on desired performance characteristics. We generate empirical models that reveal the optimal concentrations and interactions of the elemental composition and performance characteristics. In this study, we select the $BaCo_{\alpha}Ce_{\beta}Fe_{\gamma}Y_{\zeta}O_{3-\delta}$ series as a proof-of-concept, and the optimal composition, $BaCo_{0.667}Ce_{0.167}Fe_{0.083}Y_{0.083}O_{3-\delta}$, was promptly determined—guided by the EDP—using only 16 independent conditions and 32 randomized experimental runs. We further demonstrate the EDP's versatility by optimizing the widely-used and high-performing $Ba_{0.5}Sr_{0.5}Co_{0.8}Fe_{0.2}O_{3-\delta}$ cathode material for solid oxide fuel cells. Our results highlight the potential of the EDP for effectively designing superior materials for solid-state electrochemical power generation systems, offering a reliable and practical alternative to conventional trial-and-error screening and ML methods.

Keywords: Protonic ceramic fuel cells; Experimental design paradigm; Cathode; Solid oxide fuel cells

1.0 Introduction

Adopting renewable energy resources and developing clean and efficient energy conversion technologies are critical for realizing the carbon-neutrality goal and alleviating the global climate problem [1,2]. Protonic ceramic fuel cells (PCFCs) are highly promising for power generation due to their high efficiencies and low emissions[3]. At an operating temperature range of 400-600 ^{o}C, PCFCs show much higher reaction kinetics than room-temperature proton exchange membrane fuel cells (PEMFCs)[4]. Compared with high-temperature (usually above 800 ^{o}C) solid oxide fuel cells (SOFCs), PCFCs are potentially more cost-effective with a simplified thermal management system and a much-improved cell durability [5–10].

The primary performance loss of PCFC is due to the high polarization resistance of the cathode for oxygen reduction reaction (ORR)[5–8,11]. Thus, developing a highly active and stable ORR cathode is crucial in achieving high-performance PCFCs[3]. There are currently two approaches for new cathode material development, i.e., trial-and-error experimental screening process and machine learning (ML)-based method[5,12,13]. The mainstream trial-and-error approach is time-consuming, costly, and extremely difficult to identify the optimal composition from thousands of choices in a system [14,15]. Although the ML approach can facilitate the identification of potential cathodes for SOFCs from thousands of possible perovskite-oxide compositions[12], its accuracy heavily depends on the availability of a broad and reliable dataset [12]. Unfortunately, the current dataset for PCFC cathode materials is limited, resulting in a lack of data to support the accuracy of the ML approach in predicting suitable cathode materials for PCFCs. Therefore, the limitations of current methods for PCFC cathode material development (trial-and-error process and ML) urgently call for an alternative, reliable, efficient, and practical approach to address the issue of efficient development of highly active and stable ORR cathodes for PCFCs. Here, for the first time, we present a new approach based on the universal experimental design paradigm (EDP) [16,17] that promises to revolutionize the way that cathode materials are

discovered for PCFCs, paving the way for the widespread adoption of PCFCs in the energy industry.

Experimental design (ED), popularly known as the design of experiments (DOE), is a rigorous systematic statistical paradigm that attempts to explain the changes in single or multiple outcomes of interest under controlled conditions that are hypothesized to cause the changes[16]. The EDP process comprises planning, implementing, analyzing, and interpreting controlled experiments to evaluate the hypothesized factors and interactions that cause a deviation in the outputs of interest[16,17]. Even though limited SOFC modeling studies have employed the EDP[18,19], its application to developing new materials remained largely untapped. As far as we know, there have been no previous endeavors to implement the EDP for cathode material screening, optimization, and discovery, particularly for PCFCs.

Given that the oxygen reduction reaction (ORR) activity and stability of perovskite-oxide cathodes in ceramic fuel cells (CFCs) are closely linked to the composition and stoichiometric ratios of the A- and B-site cations, we selected the advanced $BaCo_{\alpha}Ce_{\beta}Fe_{\gamma}Y_{\zeta}O_{3-\delta}$ family as a proof-of-concept to thoroughly demonstrate the effectiveness of the EDP for material screening. The ceramic material, with a nominal composition of $BaCo_{0.667}Ce_{0.167}Fe_{0.083}Y_{0.083}O_{3-\delta,}$ demonstrates exceptional performance, as evidenced by its composite desirability score of 0.9918. This ceramic material exhibits a low area-specific resistance (ASR), high bulk diffusion coefficient (D_{chem}), high surface exchange constant (k_{chem}), optimal electronic conductivity (EC), and high-power output. The ED analysis reveals that the interaction between Co and Ce contributes the most to decreasing ASRs. The primary effect of Co is found to be the most influential in enhancing the EC, while the interaction between Co and Y has the most significant impact on improving the D_{chem} and k_{chem} of $BaCo_{\alpha}Ce_{\beta}Fe_{\gamma}Y_{\zeta}O_{3-\delta}$ (BCCFY) nanocomposites. These findings suggest that Co and its interactions with Ce and Y play a crucial role in the electrocatalytic performance of the

nanocomposites. We further prove the versatility of the EDP by examining the popular $Ba_{0.5}Sr_{0.5}Co_{0.8}Fe_{0.2}O_{3-\delta}$ material system[10], identified as a high-performing and promising cathode material for SOFCs. By simultaneously optimizing the stoichiometric ratios of the A- and B-site cations of the $Ba_{\alpha}Sr_{\beta}Co_{\gamma}Fe_{\zeta}O_{3-\delta}$ (BSCF), we achieved an optimal composition of $Ba_{0.8}Sr_{0.2}Co_{0.5}Fe_{0.5}O_{3-\delta}$ that exhibited superior cathodic performance for oxide ion conducting SOFCs. At 650 ^{o}C, $Ba_{0.8}Sr_{0.2}Co_{0.5}Fe_{0.5}O_{3-\delta}$ shows a very low ASR of 0.0164 Ω cm^2, and the peak power density exceeds 2000 mA cm^{-2}, surpassing the ORR activity of the pristine $Ba_{0.5}Sr_{0.5}Co_{0.8}Fe_{0.2}O_{3-\delta}$ by over 55 %.

Compared with the conventional trial-and-error approach, this empirical model-based paradigm offers an expedited process for effectively screening and optimizing the energy materials and their general fabrication processes with a lower cost, shorter time, and fewer experimental runs. Unlike the ML-based method, which relies on a vast amount of quality data and algorithms to make predictions, EDP reveals the optimal material composition and causal relationships and interactions among the components of a material, promoting a more systematic and informed screening and optimization of materials with scarce data. Thus, the EDP methodology can serve as a promising alternative to the conventional trial-and-error and ML-based approaches for developing high-performance PCFC cathodes and other functional materials for solid-state electrochemical power generation technologies.

2.0 Methods

2.1 Experimental design

The complete ED analysis was performed on the Minitab statistical package[20]. A two-level full factorial and two-level resolution IV (2_{IV}^{4-1}) fractional factorial designs with two replicates, one block, and zero center points per block were utilized to create the factorial design matrices. A principal fraction without folding was adopted, and the experimental runs were randomized.

A two-sided confidence interval at a 95% confidence level was adopted for all intervals, with no Box-Cox transformation. The entire research framework is detailed in **Figure S1.**

2.2 Material synthesis

The electrode materials based on the normalized designed factor level combinations of $BaCo_{\alpha}Ce_{\beta}Fe_{\gamma}Y_{\zeta}O_{3-\delta}$ series and $Ba_{\alpha}Sr_{\beta}Co_{\gamma}Fe_{\zeta}O_{3-\delta}$ from **Tables S6-7**, including the electrolyte powders, $BaCe_{0.7}Zr_{0.1}Y_{0.1}Yb_{0.1}O_{3-\delta}$ (BCZYYb) and $Ce_{0.8}Sm_{0.2}O_{3-\delta}$ (SDC), were synthesized using the one-pot sol-gel EDTA-citric acid complexing method [21]. This method involves dissolving nitrates of the ceramic precursors in deionized water at 100 °C under stirring conditions. After the metal nitrates were dissolved in deionized water, EDTA and citric acid were then added to the solution, with the molar ratio of the metal ions, EDTA, and citric acid being 1:1:1.5. Ammonium hydroxide (NH_4OH_2) was used to adjust the pH of the solution to 7-8, and the resulting gel was collected and dried at 176°C for 15 hours. The precursors were then crushed and calcined at 1000°C for 10 hours in ambient air to obtain the final electrodes and electrolyte materials.

2.3 Cell fabrication

The preparation of the proton-conducting electrolyte pellets involved the addition of 1% NiO to the as-synthesized BCZYYb powders via a ball milling process for 4 hours. The milled powders were then dried, pressed into a dense pellet form, and sintered at 1450°C for 10 hours in ambient air. The cathode slurries were then prepared by ball milling ethanediol, isopropanol, glycerol, and the calcinated $BaCo_{\alpha}Ce_{\beta}Fe_{\gamma}Y_{\zeta}O_{3-\delta}$ and $Ba_{\alpha}Sr_{\beta}Co_{\gamma}Fe_{\zeta}O_{3-\delta}$ precursors, followed by uniform spray application on both sides of the electrolyte pellet to generate symmetrical cells. The assembled structure (of the electrode-electrolyte) was then subjected to a sintering process at 850°C for 2 hours in ambient air. The anode-supported single cells were prepared by co-pressing and sintering the anode and electrolyte powders at 1450°C for 10 h (proton conducting

cells) and at 1350°C for 10 h for the oxide ion conducting cells. The cathode slurry was then applied onto the sintered anode-electrolyte structure via spraying, followed by another sintering process at 850°C for 2 hours in ambient air. The anode comprised NiO, BCZYYb or SDC, and starch in a ratio of 6.5:3.5:1, and Ag-paste was used as the current collector for the symmetrical and single cells.

2.4 Characterizations

The structural and morphological characterization of the $BaCo_{\alpha}Ce_{\beta}Fe_{\gamma}Y_{\zeta}O_{3-\delta}$ series and $Ba_{\alpha}Sr_{\beta}Co_{\gamma}Fe_{\zeta}O_{3-\delta}$ was performed using X-ray diffraction (XRD) patterns collected using a Rigaku SmartLab 9kW-advance instrument. The XRD patterns were analyzed using the Rietveld refinement method with the open-source Fullprof Suite software [22]. In addition, scanning electron microscopy (SEM) with a TESCAN MAIA3 and high-resolution transmission electron microscopy (HR-TEM) with an American FEI Talos F200S were employed to observe the morphological features of the samples (BCCFY series). Surface chemistry was analyzed using X-ray photoelectron spectroscopy (XPS) with a Thermo Fisher Scientific Nexsa instrument.

Inductively coupled plasma optical emission spectrometry (ICP-OES) was conducted to obtain supplementary elemental composition data using an Agilent 5110 ICP-OES instrument. The key parameters were: RF power - 1.20 KW; Plasma flow - 15.0 L/min; Auxiliary flow - 1.50 L/min; Nebulizer flow - 0.75 L/min; Sample uptake delay - 15 s; Instrument stabilization delay - 15 s; Replicate read time - 2 s; Replicates - 3 times. Samples were prepared by dissolving the cathode powders in dilute nitric acid followed by suitable dilutions to obtain solutions within the calibration range. The emission intensities of Ba, Co, Ce, Fe, and Y were measured at wavelengths of 455.403 nm, 228.616 nm, 413.764 nm, 238.204 nm, and 371.029 nm respectively. Triplicate readings were taken and averaged for each sample. The final elemental

compositions were calculated based on the calibration curves. This partial ICP-OES analysis provided supplementary validation of the relative concentration trends determined through EDP screening.

The electrical conductivity and electrical conductivity relaxation (ECR) properties of the dense bars of $BaCo_{\alpha}Ce_{\beta}Fe_{\gamma}Y_{\zeta}O_{3-\delta}$ series were evaluated using the DC standard four-probe configuration with a Keithley 2440 source meter. The samples were prepared for testing by pressing and sintering them at 1120 ^{o}C for 10 h in ambient air to obtain dense bars. The gas flow rate used in each test was 200 cm^3 min^{-1}. The D_{chem} and k_{chem} were estimated from the ECR results using a previously described approach [23].

2.5 Electrochemical testing

The symmetrical cells were characterized using electrochemical impedance spectroscopy (EIS) with the Solarton 1260 and 1287 frequency response analyzer. The EIS measurements were conducted in a 3 % H_2O-air environment with a flow rate of 100 cm^3 min^{-1} (for the PCFCs). While for the oxide ion conducting cells, synthetic air with a PO_2 of 0.21 atm at a flow rate of 100 cm^3 min^{-1} ambient conditions was employed. The performance of the single cell was evaluated using a Keithley 2440 source meter in a four-probe configuration. During the test, the cathode side was exposed to ambient air, while the anode chamber was supplied with hydrogen (H_2) at a flow rate of 110 cm^3 min^{-1}.

3. Results and discussion

3.1 Research Framework

The methodological screening and optimization process for cathode materials based on the EDP is schematically simplified in **Figure 1**. It comprises a knowledge-guided selection of the compositional elements and design matrix, synthesis of the cathode material series, fabrication

and testing of the samples, and the analysis and interpretation of the results. The elaborate framework for developing functional materials for PCFCs based on the EDP is outlined in **Figure S1**.

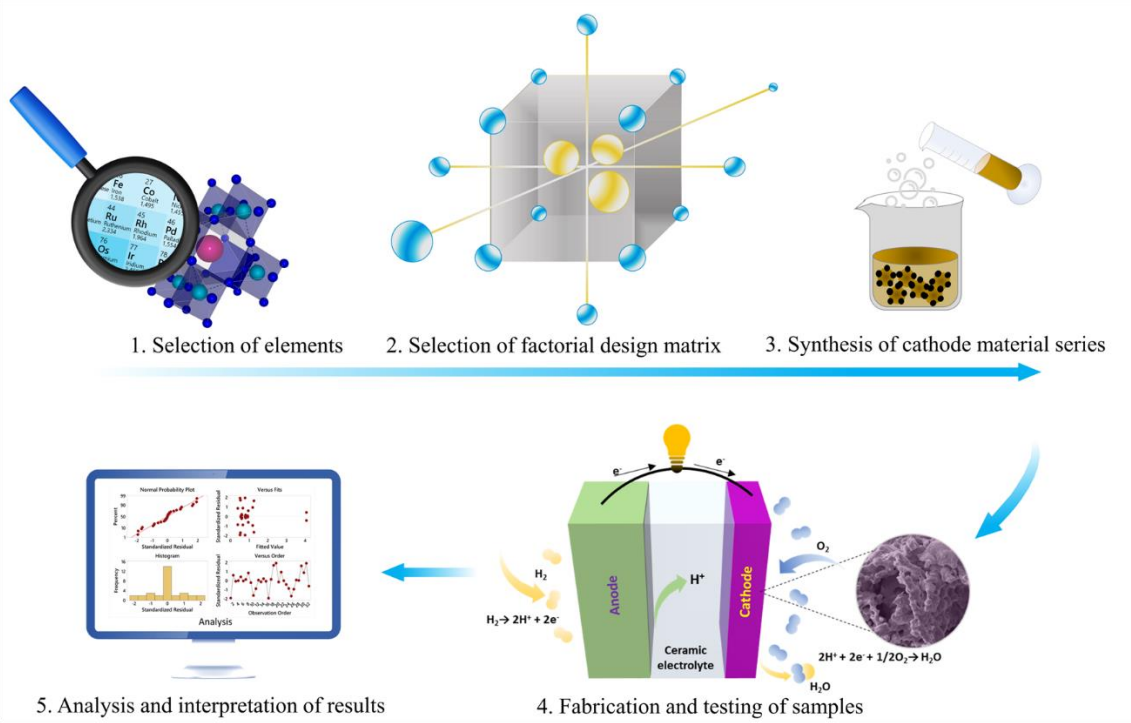

Figure 1: Simplified cathode material development framework based on the EDP. Selection of elements, selection of factorial design matrix, synthesis of cathode materials series, fabrication and testing of samples, and analysis of results.

3.2 Selection of elements

The selection of B-site elements in the BCCFY nanocomposites was carried out with a focus on the stabilizing and catalytic enhancement effects of the Ba element[24,25]. The large ionic radius of Ba (1.61Å) makes it an essential stabilizing agent and a crucial control variable in perovskite oxide structures [25,26]. The structural stability of perovskite oxides is paramount for ceramic fuel cells operating at elevated temperatures, which is critical to maintaining their electrocatalytic performance.

For PCFCs, triple ionic-electronic conductivity (TIEC) is essential for their cathode materials because it ensures the amplification of the active electrochemical reaction sites for ORR beyond the triple phase boundary[3,25,27,28]. Achieving TIEC in a typical perovskite oxide material requires that the material possesses sufficient oxygen vacancies that can be easily hydrated to create protonic carriers[29]. One possible strategy for realizing this TIEC is incorporating proton transport-enhancing dopants, in an optimal proportion, into pre-existing mixed ionic and electronic conducting (MIEC) cathode materials[3].

Co is a transition element with high electronic conductivity, making it promising for promoting efficient electron transfer in cathode materials. Studies have shown that Co-containing cathode materials have substantially improved electronic conductivity[28]. Ce is a rare earth element with excellent ionic conductivity, facilitating a high oxygen vacancy concentration in Ce-containing perovskite oxide materials[15,25]. Also, Ce plays a significant role in stabilizing protons in perovskite oxides, potentially mitigating an excessive migration of electron holes and promoting the transport of ionic species, which could contribute to the overall stability and performance of PCFC cathode materials [29]. Fe has a considerable reduction potential, making it a viable candidate that could enhance catalyzing cathodic reactions in PCFCs[30]. The capacity of Fe to form a mixed-valence compound with oxygen further underscores it as a desirable component for improving the ionic conductivity of cathode materials[11]. The rare earth element Y enhances high ionic conductivity in perovskite oxide structures by positively impacting their stability[31–33].

Hence, in a TIEC material, the mobile carriers: oxygen vacancies (Vö), electron holes (ḣ), and protonic defects (OHȯ) are in dynamic equilibrium[27]. In proton-generating atmospheres such as H_2O, the dynamic equilibrium of the mobile carriers shifts through the dissociative incorporation of water into the Vö, producing OHȯ [28]. Eqn. 1 illustrates this phenomenon in an acid-base reaction, where $O_O^{\times}$ is the lattice oxygen [28].

$$H_2O + O_O^{\times} + V\ddot{o} \leftrightharpoons 2OH\dot{o} \qquad 1$$

Ba, Co, Ce, Fe, and Y have been selected as an example to illustrate the EDP due to their unique and promising features in potentially achieving superior TIEC in PCFC cathode materials. Their unique properties, such as the large ionic radius of Ba, the high electronic conductivity of Co, the excellent ionic conductivity of Ce, the high reduction potential of Fe, and the stability-enhancing properties of Y, make them suitable candidates for simultaneously promoting efficient transfer of the mobile carriers ($V\ddot{o}$, $\dot{h}$, and $OH\dot{o}$). The EDP requires the experimenter to have foundational knowledge to identify principal factors that may trigger the desired variability in the outcomes of interest [16]. We have also selected a pre-existing high-performing composition, $Ba_{\alpha}Sr_{\beta}Co_{\gamma}Fe_{\zeta}O_{3-\delta}$[10], under the SOFC mode to investigate the efficacy and versatility of the EDP.

3.3 Selection of factorial design matrix

The selection of a factorial design matrix is an integral part of well-designed experimental planning in cathode material design[16]. After identifying the important factors (elements), it is crucial to designate control variables (if any) and precisely identify the responses of interest and whether they need to be minimized or maximized[16]. Selecting a suitable factorial design matrix is a pivotal step in applying the EDP. It ensures the validity and reliability of the experimental results and optimizes the cathode material design for superior performance.

For the BCCFY series, the factors are the B-site cations (Co, Ce, Fe, and Y), and the A-site cation (Ba) is the control variable. While for the BSCF series, both A- and B-site cations (Ba, Sr, Co, and Fe) are the factors. The response variables based on the BCCFY series for PCFCs are ASRs, electronic conductivity, D_{chem}, and k_{chem}, all in the temperature range of 500 - 650°C. These factors were selected to comprehensively evaluate the electrochemical performance, covering reaction kinetics, electrical transport, and surface exchange phenomena critical for

the PCFC cathode[3,15,23,34,35]. Since the BSCF series is only for methodological validation purposes, the only response variables considered are the ASRs from 500-650 ^{o}C under SOFC mode. We aim to minimize the ASRs and maximize the D_{chem}, $k_{chem,}$ and EC responses to achieve superior cathodic performance.

To achieve the desired goal, we adopted a two-level factorial design[16]. Since we have four factors in each case, a 2^4 full-factorial design with two replicates is adopted for both cathode material series for the ASR response variables and electronic conductivity responses for the BCCFY series to eliminate confounding bias from the factor interactions[16]. A 2^4 full-factorial design with two replicates implies that 16 independent conditions will be randomly examined twice.

On the other hand, the complexity of fabricating the samples and testing the D_{chem} and k_{chem} responses necessitates employing 2_{IV}^{4-1} (two-level resolution four) fractional factorial design with a single replicate [16]. The knowledge from the full-factorial design may aid in drawing more accurate conclusions from the factors-response analysis of the D_{chem} and k_{chem}. A 2_{IV}^{4-1} design implies that only eight (8) independent conditions will be examined instead of a full-factorial design with 16 independent conditions. This results in the main effects being aliased with three-variable interaction effects and two-variable interaction effects being confounded, as shown in **Table S1**[17].

The hypothesized upper and lower concentration limits for the factors are summarized in **Table S2.** Thus, 32 experimental runs are required to determine the effects of the factors on the ASR and electronic conductivity of the cathode electrodes, and eight (8) experimental runs to investigate the effects of the factors on the other response parameters (D_{chem} and k_{chem}), as shown in the matrix of experiments in **Table S(3-5)**.

Following the ABO_3 perovskite oxides convention (i.e., $\sum_{i=1}^{n} A_i = 1$ and $\sum_{i=1}^{n} B_i = 1$), the cationic concentrations can be normalized using Eqn. 2.

$$P_C = \frac{jC_i}{\sum_{i\in\{\alpha,\beta,\gamma,\zeta,\dots\}} jC_i} \times 100 \qquad 2$$

where P_C represents the normalized stoichiometric molar percentage of any of the cations in the perovskite oxide material, j represents the cation site (A- or B-site), C_i denotes the raw concentration value of cation C, with the raw concentration values being a subset of $\alpha, \beta, \gamma, \zeta,$ and so on. The estimated values are expressed in the matrix of experiments in **Tables S(6-7).**

3.4 Synthesis of cathode material series

As determined by the matrix of experiments in **Tables S(6-7)**, the cathode material series with normalized compositions were synthesized via a one-pot sol-gel approach. Subsequently, the resulting materials were subjected to a calcination process at 1000°C for 10 h in ambient air, after which their X-ray diffraction (XRD) patterns were obtained. As depicted in **Figure 2a**, the BCCFY materials exhibited well-defined peaks and self-assembled nanocomposite structures **(Figure S2)**. While not further explored here, the XRD refinements revealed some minor unassigned peak shifts (**Figures S2c, S2d, S2h**), which may indicate the presence of secondary phases not detectable in the primary analysis. However, the critical conclusion of the initial structural characterization was that varying the B-site stoichiometry triggered changes across the BCCFY series rather than comprehensively profiling all subtle structural variations. Meanwhile, the XRD patterns in **Figure 2b** indicated that the BSCF series mainly consisted of single-phase materials. Notably, not all powders in the BSCF series formed a pure crystal phase, even though they were subjected to the same conditions, which could be empirically attributed to their differing stoichiometric ratios[36].

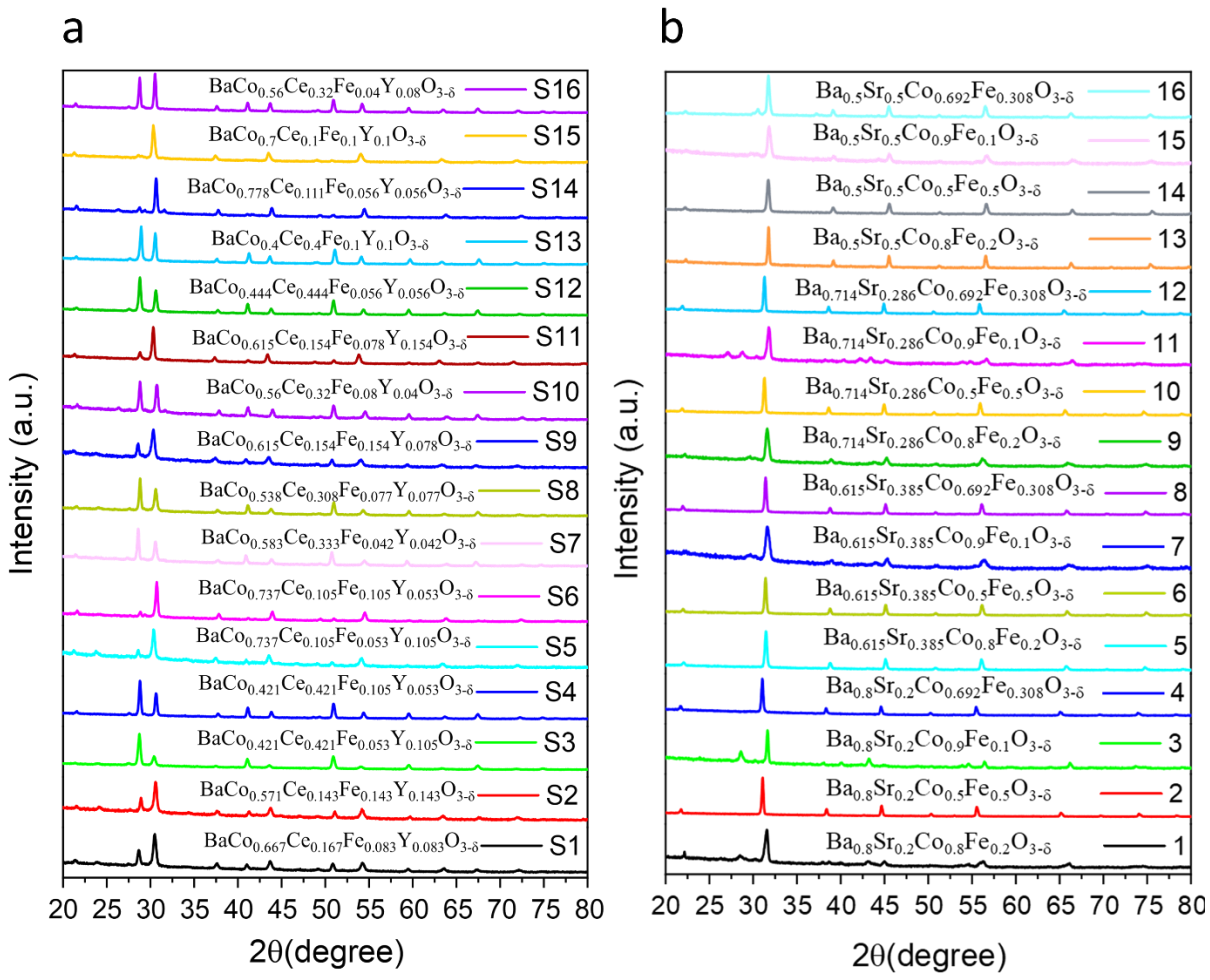

Figure 2: Crystallographic structures of all as-synthesized materials after calcination at 1000 °C for 10 h. (a) $BaCo_{\alpha}Ce_{\beta}Fe_{\gamma}Y_{\zeta}O_{3-\delta}$ series and (b) $Ba_{\alpha}Sr_{\beta}Co_{\gamma}Fe_{\zeta}O_{3-\delta}$ series where samples 1, 3, 7,9,11,15, and 16 are not pure phase.

Figure 2 suggests that the material compositions and stoichiometric ratios significantly contribute to variability in the crystallographic structure of cathode materials. ICP-OES was conducted on two BCCFY specimens to quantify the elemental compositions as a supplementary validation step. While absolute concentrations showed some divergence from expected values, the relative elemental trends matched well with those in the experimental design matrix (**Tables S56-57, Figure S55**). This partial compositional analysis further supports the composition-dependent relationships revealed through EDP screening. However,

comprehensive quantitative characterization of all samples is recommended in future systematic EDP studies.

3.5 Fabrication and testing of samples

Symmetrical cells were fabricated based on the cathode material series, following the combinations of factors and levels outlined in the experimental design matrices in **Tables S(3,4)**. The BCCFY series were tested using proton-conducting $BaCe_{0.7}Zr_{0.1}Y_{0.1}Yb_{0.1}O_{3-\delta}$ (BCZYYb) electrolytes, while oxide ion conducting $Ce_{0.8}Sm_{0.2}O_2$ (SDC) electrolytes were employed for the BSCF series. The testing conditions for the BCZYYb-based symmetrical cells were 3 % H_2O-air, while the SDC-based symmetrical cells were tested under synthetic air (with PO_2 = 0.21 atm), all within the temperature range of 500 - 650 ^oC.

Dense rectangular block samples were fabricated to conduct electronic conductivity and electrical conductivity relaxation (ECR) tests for the BCCFY material series. The ECR test data were subsequently used to calculate the samples' D_{chem} and k_{chem} parameters according to the run order in **Table S5**. The preparation and testing of the symmetrical cells (BCCFY and BSCF series) and the dense rectangular block samples for electronic conductivity were based on the run order in the experimental design matrices in **Tables S(3,4).** It was ensured that randomization and replication conditions for quality experimental designs were fulfilled[17]. **Table S9** shows the results matrix with D_{chem} and k_{chem} as the response variables in the temperature range of 500 - 650 ^oC, with just one replicate. **Table S10** presents the matrix of results for the BCCFY series comprising eight (8) response variables (ASRs from 500 - 650 ^oC, and electronic conductivity from 500 - 650 ^oC). **Table S11** shows the results matrix for the BSCF series with four (4) response variables (ASRs from 500 - 650 ^oC). The results in **Tables S(9-11)** will be used for the ED analysis, followed by relevant discussions in the later sections.

3.6 Factorial ED analysis

The purpose of conducting the factorial ED analysis is to understand the influence of individual factors or factor combinations on the response variables, determine the most significant factors contributing to variability in the response variables, and evaluate the validity of the statistical models used for making inferences.

3.7 Hierarchy of terms triggering variability in the ORR of the cathode material series

Pareto charts are commonly used in determining the statistical impact of main and interaction effects in experimental designs (EDs)[16,20]. Hence, a hierarchical examination of the standardized effects from the Pareto charts was conducted to analyze the interaction effects between elements. The orientation and magnitude of the effects reveal how the interactions between elements impact the responses. **Figures (3a, S5-6)** show the chart presenting the standardized effects in decreasing order of absolute values, considering the error term in the statistical model. However, when the model does not incorporate an error term, such as with the D_{chem} and k_{chem} regression models, the chart displays the absolute values of the unstandardized effects, as illustrated in **Figure S7**. The reference line on the Pareto chart differentiates between significant and non-significant effects. If the error term is not included in the model, Lenth's method (Pseudo Standard Error) is applied to determine the reference line (**Supplementary note 1**). A significance level of 0.05 was used to evaluate the statistical significance level of the effects[17]. Here, an effect is considered significant if it contributes to a variability of up to 5% in the response variable. The analysis of the effects contributing to variability in the response variables is illustrated in **Figure 3**. The Pareto charts of the standardized effects influencing the ASR of both material series and electronic conductivity of BCCFY at temperatures ranging from 500-650°C are displayed in **Figure 3a, S5-6)**. The Pareto chart of the effects of D_{chem} and k_{chem} at temperatures in the same range is presented in **Figure S7**, with effects arranged in decreasing absolute values. The reference line separates the

significant from the non-significant effects, with any term falling below the reference line deemed non-significant, as determined by the predefined significance level of 0.05. **Figure 3a, S5),** which visually represent the standardized effects contributing to the variability in the ASR and electronic conductivity of the BCCFY series at temperatures ranging from 500-650°C, demonstrate that all the main factors, namely Co, Ce, Fe, and Y, are statistically significant across all temperatures investigated. However, Ce*Y, Co*Ce*Y, and Co*Ce*Fe*Y interaction effects are statistically insignificant at 650°C, as evident from **Figure 3a.** It should be noted that, at 650°C, the non-significant terms should not be considered when making inferences based on the ASR response. The top five significant terms contributing to the variability in the ORR response of BCCFY-series at 650°C, in hierarchical order, are Co*Ce>Y>Co*Fe*Y>Ce*Fe*Y>Co*Ce*Y, which slightly differs at lower temperatures. At 600°C, the absolute order of the top five terms contributing to the variability in the ORR response is Co*Ce>Y>Co*Ce*Y>Co*Fe*Y>Ce*Fe*Y (**Figure S5a**), while at 550°C and 500°C the order is Co*Ce>Y>Co*Ce*Y>Co*Fe*Y>Fe, as shown in **Figures S5(b-c)**. This varying trend may be due to specific relationships between the B-site cations and the mobile carriers ($V_{\ddot{o}}$, $\dot{h}$, and $OH_{\dot{o}}$) in the BCCFY perovskite oxide lattice series at different temperatures[37]. Above 600 ^{o}C, it has been suggested that proton concentration in perovskite oxides, with varying Ce content, decreases [29]. It is evident from the analysis of the effects contributing to the variability in the ORR and electronic conductivity responses (**Figure 3a, S5,7)** that the interaction effect of Co*Ce had the most significant impact on the ORR of BCCFY under PCFC mode at all temperatures. On the other hand, the main effects of Co and Y were the primary contributors to the variability in the electronic conductivity responses of BCCFY. The Ba*Sr*Co*Fe interaction effect is identified to contribute the most to variability in the ORR responses of the BSCF series across all the temperature ranges **(Figure S6)**.

Figures S(8-10) attempt to differentiate the orientation of the effects on the ORR and electronic conductivity.

The analysis of the effects in **Figure 3b** shows that the interaction effect of Co*Ce also has the most significant impact on enhancing ORR activity in the $BaCo_{\alpha}Ce_{\beta}Fe_{\gamma}Y_{\zeta}O_{3-\delta}$ cathode material series at all temperatures. This result confirms previous findings that nanocomposite cathode materials rich in Co and Ce can attain superior catalytic ORR in PCFCs [14,15,38]. The terms contributing to the reduction of ASR, such as Co*Ce*Y, Ce*Fe*Y, Ce*Fe, and Fe*Y, are the same elements found in some reported triple-conducting cathode materials for PCFCs [11,14,39,40]. This finding supports the results obtained through the EDP model and indicates that the model can be utilized for more than just screening and optimizing materials. It can also identify promising elemental combinations for creating high-performing materials for various applications.

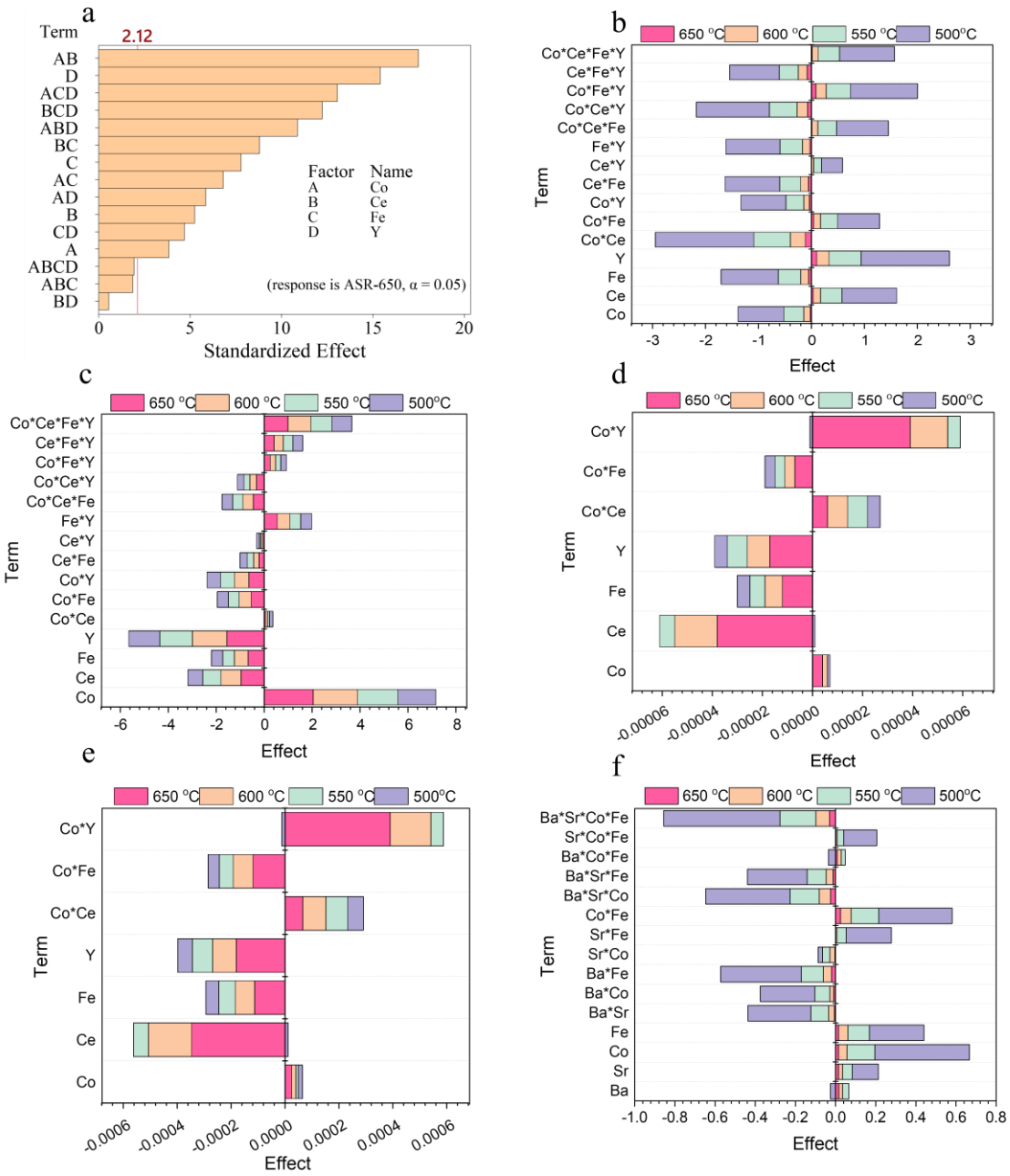

Figure 3: Analysis of effects contributing to the variability in the ORR of the $BaCo_{\alpha}Ce_{\beta}Fe_{\gamma}Y_{\zeta}O_{3-\delta}$ and $Ba_{\alpha}Sr_{\beta}Co_{\gamma}Fe_{\zeta}O_{3-\delta}$ series at temperatures between 500-650 °C. (a) Pareto chart of the standardized effects with a significance level of 0.05 for the ASR at 650°C. Coefficient of effects causing variability in (b) ASR of BCCFY series from 500 – 650 ºC (c) Electronic conductivity of BCCFY series from 500 – 650 ºC (d,e) D_{chem} and k_{chem} of BCCFY series at 650 ºC and (f) ASR of BSCF series from 500 – 650 ºC.

Figure 3(b-f) summarize the effects coefficients that contribute to the variability in ASR, EC, D_{chem}, and k_{chem} in the temperature range of 500 – 650 ºC, based on the effects column in **Tables**

S(13-31). The results presented in **Figure 3(b,c)** suggest that Co is the primary contributor to the increase in electronic conductivity at all temperatures, while Y has the most detrimental effect on both electronic conductivity and ORR. In maximizing electronic conductivity and ORR performance in the nanocomposites, we recommend significantly minimizing the concentration of Y. For the D_{chem} and k_{chem}, the interaction effects of Co*Y (confounded with Ce*Fe), Co*Ce (confounded with Fe*Y), and the main effect of Co (cofounded with Ce*Fe*Y) were found to have a substantial impact on enhancing these parameters, as indicated in **Figure 3(d,e)**. Even though BCCFY and BSCF series are dissimilar categories of materials tested under different conditions, it can be observed that the interaction effect of Co*Fe, common to both material families, negatively impacts the ORR, as depicted in **Figure 3b,f)**. The results of the Pareto charts and residual plots indicate that the statistical assumptions for the significant model analysis of the ORR are satisfied [20]. The residual plots in **Figures S(11-18)** support the inference that the residuals are normally distributed, with P-values above the significance level of 0.05 [20].

3.8 Examination of the statistically significant terms triggering variability in the response parameters

This examination can be accomplished by studying the p-values obtained from the analysis of variance (ANOVA) tables. In this context, the null hypothesis posits that the terms do not affect the variability of the response parameters, and statistical significance is determined using a significance level of 0.05. The ANOVA tables for the ASR of BCCFY and BSCF series and electronic conductivity responses of BCCFY series over the temperature range of 500-650°C are presented in **Tables S(32-43)**. These tables show that each term's p-value is less than 0.05, except for some ASR terms in both material series **(Table S32,40).** In the BCCFY series, the terms Co*Y, Co*Ce*Fe, and Co*Ce*Fe*Y are not significant at 650°C, while for the BSCF series, Sr*Fe and Sr*Co*Fe are not significant at 650°C. These observations suggest a

statistically significant relationship between these terms and the responses, implying that their mean levels are unequal.

On the other hand, terms with p-values greater than 0.05 are considered insignificant in producing variability and can be disregarded when drawing statistical inferences. On the other hand, the ANOVA results revealed that all the terms associated with the electronic conductivity response variables are statistically significant, with extremely large F-values consistently over 1000. Such high F-values provide definitive evidence against the null hypotheses, demonstrating the terms' significance with associated p-values well below 0.001. Calculating the miniscule precise p-values is unnecessary, as the F-statistics unambiguously signify high significance. However, it is impossible to determine the statistical significance of the terms related to the D_{chem} and k_{chem} response variables as the model lacks error terms. Nevertheless, the impact of these terms can still be identified by applying Lenth's method, as depicted in **Figure 3(d,e)**, which suffices for the current analysis.

3.9 Model equations and validation

The relationship between the significant effects and the response parameters is established using the model equations in **Table S(44,46)**. The reliability of these models can be evaluated by examining their goodness-of-fit statistics, as presented in **Table S(45,47)**. These statistics indicate that the models are highly accurate, with a minimum R^2 value of 99.30%. To provide additional validation of these models, predicted response parameters for the BCCFY series having an entity with the lowest R^2 value of 99.30% were calculated under the conditions listed in **Table S3,** and the results are shown in **Figure 4**.

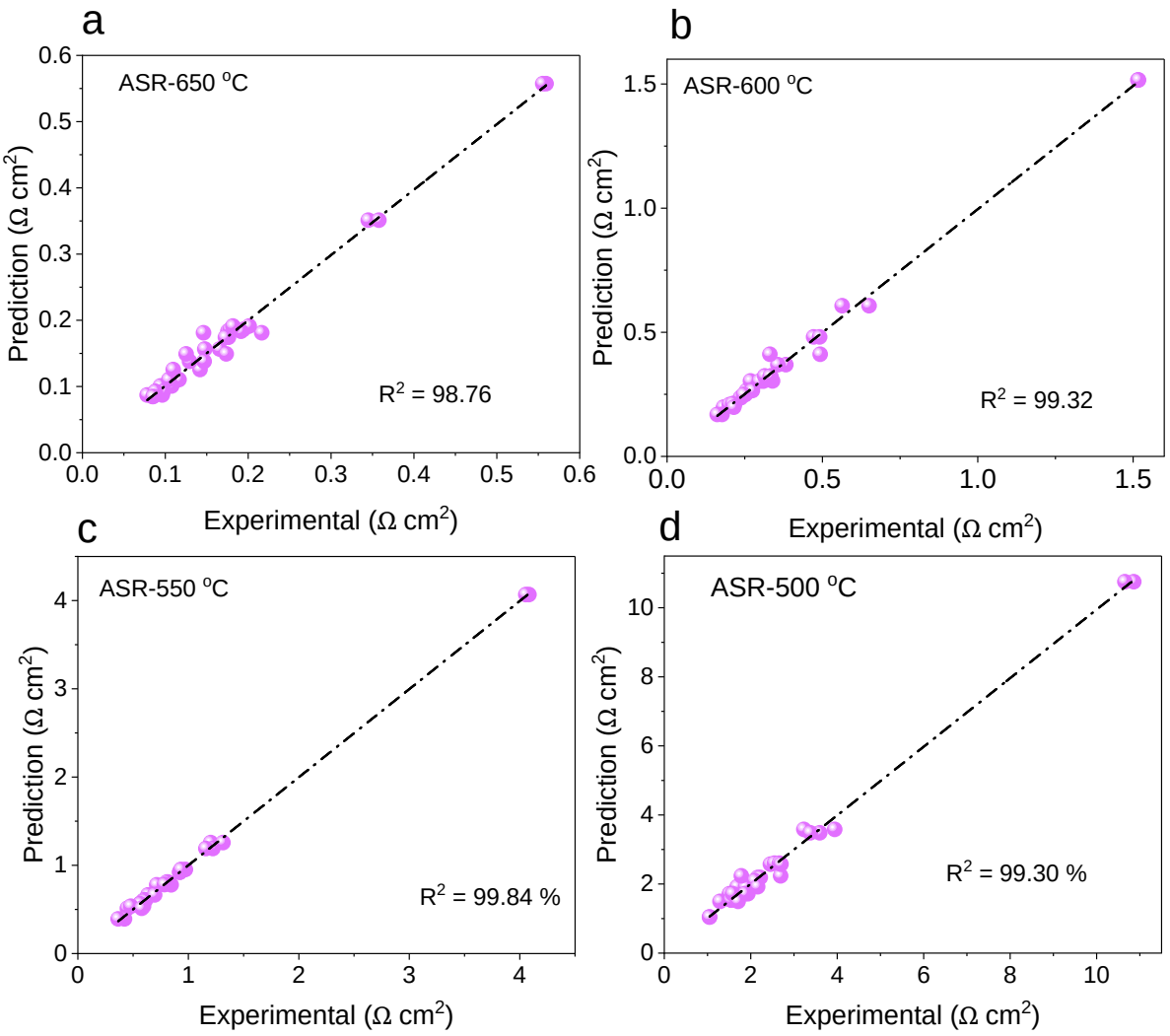

Figure 4: Comparison of the experimental and predicted response parameters based on the conditions and run-order in Table S3 for (a) ASR-650 °C (b) ASR-600 °C (c) ASR-550 °C (d) ASR-500 °C.

The high degree of consistency between the predicted response parameters and the experimental results further validates the reliability of the models, as evidenced by the minimum coefficient of determination (R^2) value of 99.30% in **Table S(45,47)**.

3.10 Contour and response surface analysis

Contour and response surface plots present the relationship between response variables and two predictor variables in a graphical manner, facilitating a more intuitive understanding of the data. These plots are created from the empirical model described in **Eqn. 3**, and they provide valuable insights into the interactions between variables and the impact of changes in one variable on the response variables.

$$y = \beta_0 + \sum_{i=1}^{k} \beta_i x_i + \sum_{i \le 1 \le j}^{k} \beta_{ij} x_i x_j + \varepsilon \qquad 3$$

Where y represents the response variable, β_0 is the intercept term, x_i are the predictor variables, β_i are the corresponding regression coefficients, β_{ij} are the coefficients for the interaction terms between predictor variables x_i and x_j, and ε is the residual error term.

Focusing on the BCCFY series, the plots in **Figure 5** demonstrate the relationship between the concentrations of the significant two-predictor variables (Co & Ce, Co & Fe, Co & Y, and Ce & Fe) and the ASR response variables at 550°C. The empirical models in **Table S45** were used to generate these plots. The plots illustrate that the ORR can be improved at two distinct regimes: (i) when the Co concentration is between 40 and 60 and the Ce concentration is less than or equal to 15, and (ii) when the Ce concentration is between 20 and 40 and the Co concentration is greater than 65, as shown in **Figure 5(a,b)**. The plots suggest that fixing the concentrations of Co and Fe at their maximum design values (70 and 10, respectively) and Ce and Y at 25 and 7.5, respectively, can result in a high ORR performance, as depicted in **Figure 5(c,d)**. In addition, the plots depict that a higher concentration of Fe and a lower concentration of Y in BCCFY leads to an improved ORR performance, as illustrated in **Figure 5(e-h)**.

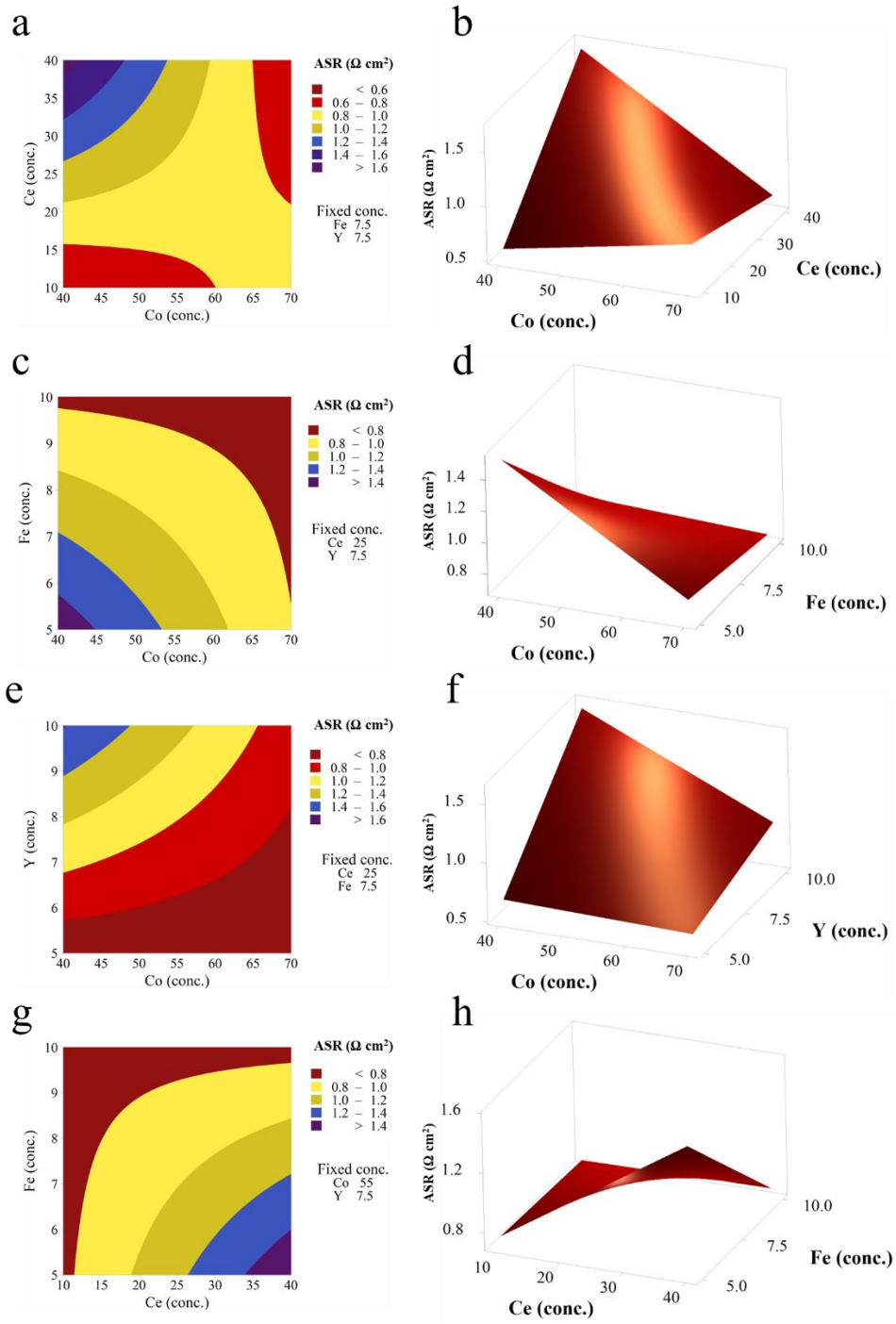

Figure 5: Contour and corresponding response plots of the significant two-factor interactions for ASR of BCCFY series at 550 ºC. (a,b) Co and Ce interaction. (c,d) Co and Fe interaction. (e,f) Co and Y interaction. (g,h) Ce and Fe interaction.

The results of the factorial ED analysis indicate that the interaction effect of Co*Ce has the most pronounced effect on enhancing the ORR performance in the $BaCo_{\alpha}Ce_{\beta}Fe_{\gamma}Y_{\zeta}O_{3-\delta}$

nanocomposites. Furthermore, the main effect of Co has the most significant impact on increasing EC. The Co*Y interaction, cofounded with Fe*Ce, Co*Ce interaction (confounded with Fe*Y), significantly contributed to the increase in both D_{chem} and K_{chem}. This information can be inferred from the contour and response surface plots displayed in **Figure 5**, as well as the supplementary **Figures S(19-21)** for ASR response variables, **Figures S(22-25)** for electronic conductivity response parameters, and **Figures S(26-33)** for D_{chem} and k_{chem} responses. It is observed that increased Co concentrations generally lead to an improvement in electronic conductivity. Conversely, higher concentrations of Ce and Y negatively impact electronic conductivity through their detrimental effects on electron-hole transport, as illustrated in **Figure S9**[15]. In attaining higher D_{chem} and k_{chem} values, reducing the concentrations of Ce below 12, Y below 5.5, Co below 45, and Fe below seven is recommended. However, the D_{chem} and k_{chem} trends at 500°C diverged from the other temperatures (**Figures S26-S33**), indicative of possible experimental artifacts or temperature-dependent material effects that warrant deeper investigation. As for the BSCF series, Ba*Fe is the most significant two-factor interaction **(Figure S10)**. Hence, setting the concentrations of Ba below 55 and Fe close to 10 while fixing Sr and Co at 35 and 65, respectively, leads to increased ORR **Figures S(34-37)**.

3.11 Structure and Morphology of $BaCo_{\alpha}Ce_{\beta}Fe_{\gamma}Y_{\zeta}O_{3-\delta}$ nanocomposites

The microstructural and morphological characteristics of the $BaCo_{\alpha}Ce_{\beta}Fe_{\gamma}Y_{\zeta}O_{3-\delta}$ nanocomposites were analyzed. The X-ray diffraction (XRD) patterns were analyzed through Rietveld refinement for half of the total independent conditions of the materials corresponding to S1-8 in **Figure S2**. The results indicated that all the materials were self-assembled nanocomposites with two or more cubic, rhombohedral, orthorhombic, and hexagonal phases. The lattice parameters of the phases in the materials are presented in **Table S8.** The high-resolution scanning electron microscopy (HR-SEM) images, depicted in **Figure S3**, reveal the

unique microstructural arrangements of the nanocomposites, which exhibit variations in grain size, shape, and color. These observations suggest that the variability in ORR can be attributed to the differences in material composition.

The oxidation states of the B-site cations in perovskite oxides are a key factor in determining the concentration of oxygen vacancies in functional energy materials[11]. Hence, X-ray photoelectron spectroscopy (XPS) characterization was conducted on half of the total independent conditions of the $BaCo_{\alpha}Ce_{\beta}Fe_{\gamma}Y_{\zeta}O_{3-\delta}$ nanocomposites. The results of this characterization, which include the binding energies of the adsorbed oxygen states of Co, Ce, Fe, Y, and O, are shown in **Figures S(41-45)** and **Table S48**. The XPS data aligns with the electrocatalytic performance of the samples, as demonstrated by the binding energies of the oxygen and relative percentages of the adsorbed oxygen in **Table S48**, as well as the factorial ED analysis. In particular, the lower binding energies of Co $2p_{1/2}$ and Co $2p_{3/2}$ in sample S1 **(Figure S42)** suggest that it has the highest oxygen vacancies, which is considered favorable for the adsorption of O_2 species [41]. The XPS characterization also revealed peculiar, highly oxidative oxygen species for S4 (**Table S48**), indicative of compositional effects on oxygen speciation warranting further analysis.

The ORR behavior of the $BaCo_{\alpha}Ce_{\beta}Fe_{\gamma}Y_{\zeta}O_{3-\delta}$ nanocomposite cathode materials was analyzed through the application of the distribution of relaxation time (DRT) model [42]. The EIS data, including the data at 500 ^{o}C, was used for the DRT analysis, as shown in **Figures S(38-39)**. The analysis showed that all samples' electrical impedance decreased with increasing temperature. The presence of peaks in the high-frequency regions beyond 10^4 Hz was attributed to the rate-limiting interfacial charge transfer process resulting from the ionic conduction at the electrode-electrolyte interface [43].

Optimizing $BaCo_{\alpha}Ce_{\beta}Fe_{\gamma}Y_{\zeta}O_{3-\delta}$ for PCFC applications

Optimizing the response parameters of the $BaCo_{\alpha}Ce_{\beta}Fe_{\gamma}Y_{\zeta}O_{3-\delta}$ nanocomposite cathode materials entails analyzing the correlations between the multiple input and output parameters. The relationship between the inputs and various response parameters was established through the model equations outlined in **Table S44**. The objective was to observe factor settings that would simultaneously minimize the ASR values over the temperature range of 500 – 650 ^{o}C, and maximize the D_{chem}, k_{chem}, and electronic conductivity values over the same temperature range.

The ASRs are the most critical responses in optimizing the response parameters, reflecting ORR activity. A comprehensive evaluation of the performance of the response parameters is carried out by computing the individual desirability of each response parameter, where the value of individual desirability ranges from 0 to 1, with 1 indicating the highest level of desirability and 0 reflecting non-desirability [20]. The composite desirability is then determined based on the aggregate individual desirabilities of the response parameters [20].

The optimization results for the various responses and their individual and composite desirabilities are summarized in **Figures S(46-49)** and **Tables S(49-52)**. The optimal solution for the ORR response was found, with a near-perfect composite desirability of 0.9918. The optimal setting was determined as $BaCo_{0.667}Ce_{0.167}Fe_{0.083}Y_{0.083}O_{3-\delta}$ (BCCFY-1), with Co, Ce, Fe, and Y being set to 40, 10, 5, and 5, respectively. The optimal setting for the D_{chem} and k_{chem} responses was also detected, but with a lower composite desirability of 0.8483 and 0.8578, respectively, due to a non-conformity of the D_{chem} and k_{chem} responses at 500 ^{o}C with the other response parameter trends (**Figure 3**). The electronic conductivity response's optimal setting differed from the ORR setting due to its strong dependence on Co content (**Figure S47**), with a composite desirability of 0.9887. The optimal electronic conductivity setting was achieved by setting Co, Ce, Fe, and Y to 70, 40, 5, and 5, respectively.

The morphology and elemental distribution of the optimal BCCFY-1 nanocomposite material are displayed in **Figure 6(a-c)**. The images demonstrate a noticeable difference in the distribution of Co and Ce within the lattice structure of BCCFY-1, indicating the material's multiphasic nature (**Figure 6b**). While not further probed here, the EDS mapping highlights some phase heterogeneity with localized depletion of Co and Fe (**Figure 6b**), which may arise from distinct Ce-rich regions exhibiting enhanced proton conduction as noted in prior works [15,38]. The refined X-ray diffraction data for the optimal BCCFY-1 nanocomposite is shown in **Table S53**. Based on prior work on similar phase chemistries[15,38], the cubic Co-containing first phase likely contributes to oxide ion and electronic conduction. The second rhombohedral Ce-containing phase potentially enhances proton and ionic conduction. The minor orthorhombic phase may promote proton conduction and water incorporation. The high-resolution transmission electron microscope (HR-TEM) image shown in **Figure 6c** further supports this multiphasic characterization of BCCFY-1, which consists of cubic, rhombohedral, and orthorhombic phases, with closely connected interfaces in the nanoscale domain. The inter-atomic spacings in the diffraction planes (111), (110), and (111) are shown to correspond to the Pm-3m, R-3c, and Pnma space groups in the material, as confirmed by the XRD results with values of 2.37, 3.14, and 4.24 Å, respectively. The collective synergistic effects of these tailored conduction pathways likely underpin the exceptional performance of BCCFY-1. However, detailed studies isolating these phase-specific influences remain an avenue for future work, as deconvoluting the individual phase contributions was beyond the scope of this initial EDP demonstration.

The performance of the optimal nanocomposite material BCCFY-1 was evaluated at 650 ^{o}C in 3% H_2O-air. The results showed that BCCFY-1 had a low ASR of 0.078 Ω cm^2, EC of 3.133 S cm^{-1}, D_{chem} of 1.21E-4 cm^2 s^{-1}, and k_{chem} of 1.118E-3 cm s^{-1}. The symmetrical cells' activation energy (Ea) based on the BCCFY-1 cathode was 16% better than the Ea of the S3 cathode

(**Figure 6d**). Similarly, the Ea of the electronic conductivity of S1 was 25% better than that of S3 (**Figure 6e**). To situate the performance of optimal BCCFY-1 against other compositions, Ea data for samples S1 to S8 are shown in **Figure S40**.

The outstanding performance of the BCCFY-1 cathode prompted further investigation into its thermodynamic and ORR stability under specified ambient conditions. A high-temperature XRD (HT-XRD) was conducted on the nanocomposite powders, and the results showed that the structure of S1 was thermodynamically stable (**Figure S46**). The ORR stability, which was examined by subjecting a symmetrical cell based on the BCCFY-1 cathode to an atmospheric condition of 3% H_2O-air at 550 ^oC (**Figure S47**), revealed that the cathode material has good ASR stability. Finally, the power output of a single cell based on the BCCFY-1 nanocomposite cathode material was evaluated under dry H_2 fuel (**Figure 6f-h**).

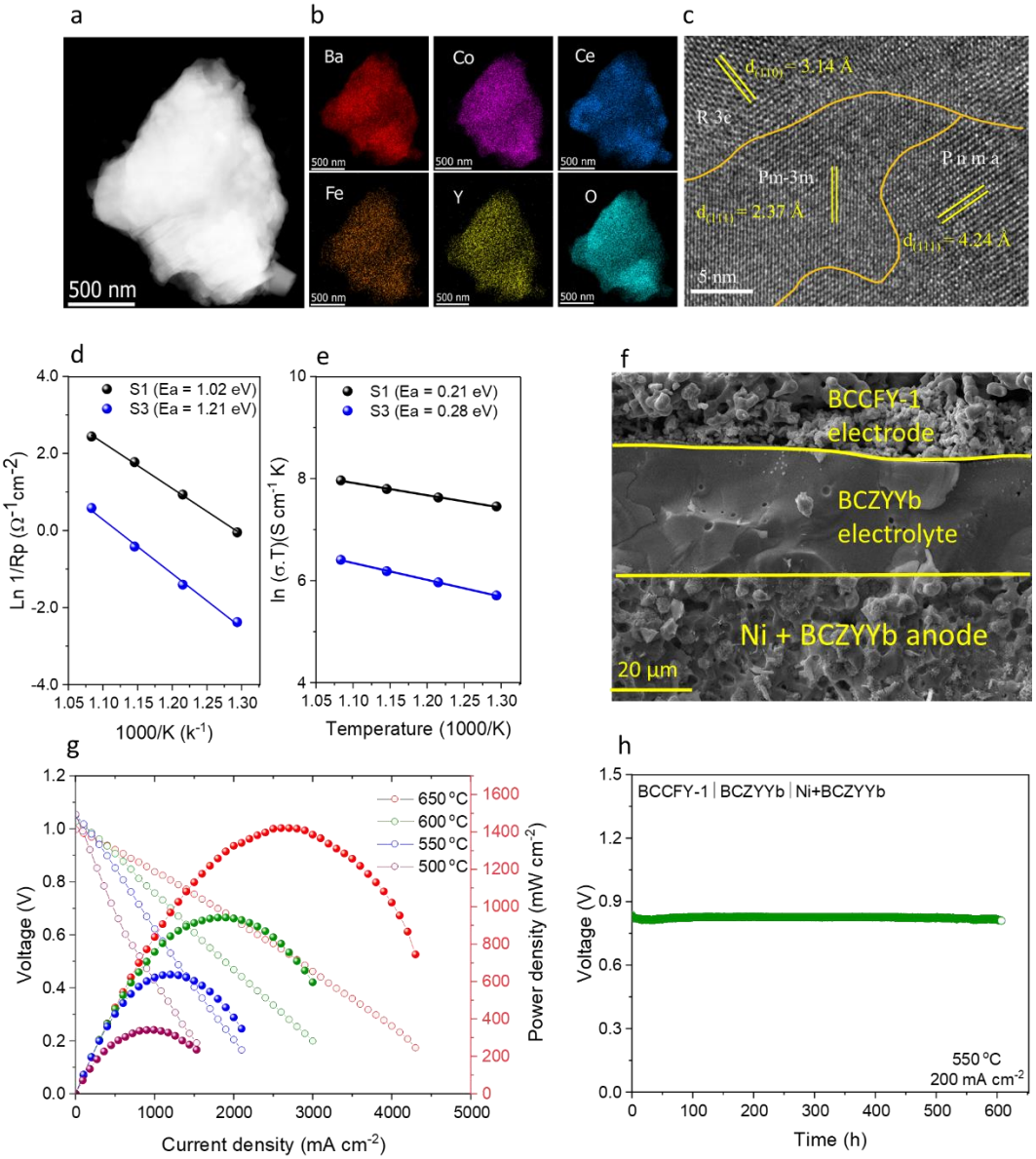

Figure 6: Morphology of the optimal BCCFY-1 (a) Scanning transmission electron microscopy (STEM) image, (b) Energy-dispersive X-ray (EDX) mapping, and (c) HR-TEM image. Arrhenius plots of the (d) ASR values of symmetrical cells based on S1 and S3 cathode materials. (e) electronic conductivity values of optimal S1 and S3 samples. (f) SEM image of a single cell cross-section based on Ni + BCZYYb | BCZYYb | BCCFY-1 configuration (g) I-V-P curves of Ni + BCZYYb | BCZYYb | BCCFY-1 single cell tested with H_2 fuel. (h) Stability of the single cell based on the configuration of Ni + BCZYYb | BCZYYb | BCCFY-1 at a current density of 200 mA cm^{-2} and 550 °C.

The performance of the proton-conducting single cell was found to be exceptional. The single cell achieved a peak power density (PPD) of 1421 mW cm^{-2} at 650 ^{o}C, surpassing the performance of most previous PCFC cathode materials **(Table S54)**. The mapping of the distribution of elements in the single cell after testing, as shown in **Figure S28,** indicated a good distribution of elements.

The operational stability of the BCCFY-1 cathode material was also evaluated, with the results showing that it was highly stable, with a span of operational stability exceeding 600 h under H_2 fuel. These results demonstrate the potential of using the EDP as a reliable approach for effectively screening, optimizing, and discovering correlations between elements in functional materials and the corresponding response variables of interest in various electrochemical material design applications.

3.13 Optimizing $Ba_{\alpha}Sr_{\beta}Co_{\gamma}Fe_{\zeta}O_{3-\delta}$ series for SOFC applications

Optimizing the BSCF series was conducted using the hybrid desirability approach [20]. The joint optimal solution for the BSCF series was identified with a high composite desirability of 0.9942, as depicted in **Figure S53**. The optimal composition was determined to be $Ba_{0.8}Sr_{0.2}Co_{0.5}Fe_{0.5}O_{3-\delta}$ by setting the respective concentrations of Ba, Sr, Co, and Fe to 80, 20, 40, and 40, as reported in **Table S55**. **Figure 7** compares the structure and performance of the optimized BSCF ($Ba_{0.8}Sr_{0.2}Co_{0.5}Fe_{0.5}O_{3-\delta}$) with the pristine BSCF ($Ba_{0.5}Sr_{0.5}Co_{0.8}Fe_{0.2}O_{3-\delta}$).

Figure 7a presents the refined X-ray diffraction (XRD) profiles of the pristine and optimized BSCF powders after calcination at 1000 ^{o}C for 10 h. The patterns confirm that both materials are homogenous and well-crystallized, with the optimized BSCF (O-BSCF) lattice having a larger volume[12]. **Figure 7**b compares the ASR of both materials and presents the ASR stability of the optimized BSCF at 550 ^{o}C. The results showed that the O-BSCF was stable and exhibited

superior performance at all temperatures, with an increase of up to 55% over the pristine BSCF (P-BSCF) at 550 °C **(Figure 7c, S53a)**.

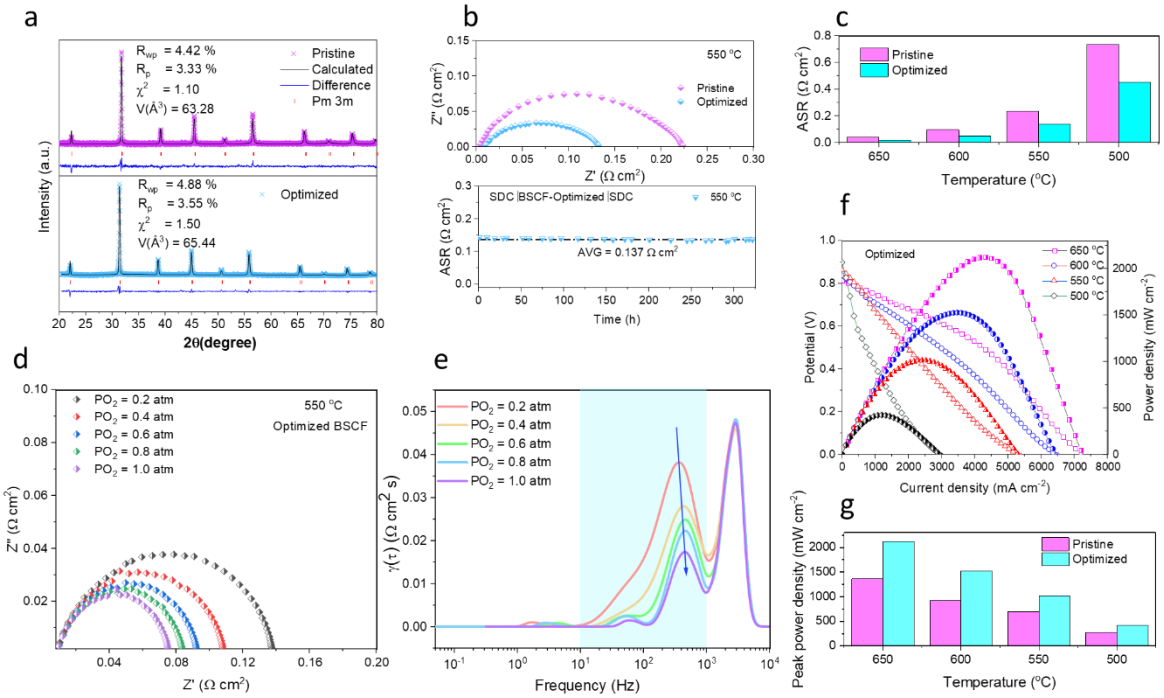

Figure 7: Performance characteristics of BSCF. (a) X-ray diffraction patterns of the pristine and optimized BSCF, (b) Comparison of the electrochemical impedance spectroscopy (EIS) of the pristine and optimized BSCF at 550 °C and the ASR stability of the optimized BSCF for over 300 h in air at 500 °C. (c) Comparison of the ASR values of the pristine and optimized BSCF from 500 – 650 °C. (d) Impedance spectra showing the response of the optimized BSCF with variation in PO_2 (atm) at 550 °C. (e) Distribution of relaxation time analysis of the spectra in (d). (f) I-V-P curves of an anode-supported single cell with the configuration Ni + SDC|SDC|optimized BSCF from 500 – 650 °C. (g) Comparison of the power densities of the pristine and optimized BSCF from 500 – 650 °C.

To gain some insights into the observed improved ORR kinetics of the optimized BSCF, symmetrical cells based on the material were subject to variation in PO_2 from (0.2 – 1 atm) at 550 °C (**Figure 7**d). Using the data from these Nyquist plots, the distribution of relaxation time (DRT) analysis was conducted (**Figure 7**e). At lower PO_2 (0.2 atm), it can be inferred that the O-BSCF experiences a significant ORR rate limiting process due to surface exchange and bulk diffusion at the electrode-electrolyte interface, observed in the frequency range of 10^1 – 10^3 Hz[12]. This phenomenon could be attributed to the limited oxygen availability, leading to slower

reaction rates. However, oxygen availability is increased at higher PO_2 (1.0 atm), resulting in a decreased rate-limiting process due to surface exchange and bulk diffusion[12].

On the other hand, the rate-limiting process due to charge transfer processes is constant (>10^3 Hz), independent of the PO_2. This behavior suggests that the rate of charge transfer is not significantly influenced by oxygen availability and remains a constant rate-limiting step. The phenomenon suggests that O-BSCF has a high oxygen vacancy concentration due to increased lattice volume, as larger lattice volumes have been associated with higher oxygen vacancy concentrations[44–46].

Finally, anode-supported single cells based on the pristine and optimized BSCF were tested under H_2 fuel. At 650 ^oC, the peak power density (PPD) of the O-BSCF-based cell exceeds 2000 mA cm^{-2}, superseding the P-BSCF by over 55 % (**Figure 7f-g, S53b)**. These results further reinforce the EDP's potential as a reliable approach for effectively optimizing pre-existing functional materials under different electrochemical applications.

4.0 Conclusion

In this work, we have introduced a novel and efficient methodology based on the experimental design paradigm (EDP) for accelerated development of optimized cathode materials for ceramic fuel cells. Compared to traditional trial-and-error approaches, EDP offers a more effective solution for rapid screening and discovery by revealing quantitative relationships between composition, elemental interactions, and material properties. Unlike machine learning methods, EDP eliminates the dependence on vast datasets.

As a proof-of-concept, EDP was demonstrated through the optimization of $BaCo_\alpha Ce_\beta Fe_\gamma Y_\zeta O_{3-\delta}$ (BCCFY) for protonic ceramic fuel cells. The optimal BCCFY composition exhibited outstanding performance, with low area-specific resistance and high peak power density. EDP

analysis identified that Co-Ce interactions significantly enhanced oxygen reduction activity, while Co-Y interactions improved surface exchange kinetics. The versatility of EDP was further validated through optimization of the $Ba_{\alpha}Sr_{\beta}Co_{\gamma}Fe_{\zeta}O_{3-\delta}$ (BSCF) system, achieving 55% better electrocatalysis over the original material.

While showing great promise, there remain exciting opportunities to build on this pioneering work and address current limitations. Incorporating quantitative elemental analysis would strengthen the composition-property relationships predicted by EDP. Applying EDP to more cathode chemistries, cell types and exploring nonlinear effects would further establish its generalizability. Microscale characterization and modelling studies could provide deeper insights into the structure-property relationships. Evaluating stability criteria and extending EDP to interfaces, electrolytes and other components are important areas of future work. Integration with high-throughput experiments or computations can enable rapid screening over more expansive compositional spaces.

This study lays the groundwork for EDP as a mainstream strategy complementary to existing materials discovery approaches. With future enhancements, we envision EDP to accelerate the development of optimized, high-performance materials for real-world clean energy systems. The novel yet simple paradigm demonstrated here marks only the beginning of harnessing the power of designed experiments for transformative materials innovation.

References

1. Stocker, T.F., Qin, D., Plattner, G.-K., Tignor, M., Allen, S.K., Boschung, J., Nauels, A., Xia, Y., Bex, V., and Midgley, P.M. (2013). IPCC, 2013: Climate Change 2013: The Physical Science Basis. Contribution of Working Group I to the Fifth Assessment Report of the Intergovernmental Panel on Climate Change.

2. Perera, A.T.D., Nik, V.M., Chen, D., Scartezzini, J.L., and Hong, T. (2020). Quantifying the impacts of climate change and extreme climate events on energy systems. Nat Energy *5*, 150–159. 10.1038/s41560-020-0558-0.

3. Duan, C., Huang, J., Sullivan, N., and O'Hayre, R. (2020). Proton-conducting oxides for energy conversion and storage. Appl Phys Rev *7*, 011314. 10.1063/1.5135319.

4. Duan, C., Kee, R., Zhu, H., Sullivan, N., Zhu, L., Bian, L., Jennings, D., and O'Hayre, R. (2019). Highly efficient reversible protonic ceramic electrochemical cells for power generation and fuel production. Nat Energy *4*, 230–240. 10.1038/s41560-019-0333-2.

5. Choi, S., Kucharczyk, C.J., Liang, Y., Zhang, X., Takeuchi, I., Ji, H.-I., and Haile, S.M. (2018). Exceptional power density and stability at intermediate temperatures in protonic ceramic fuel cells. Nat Energy *3*, 202–210. 10.1038/s41560-017-0085-9.

6. Duan, C., Kee, R.J., Zhu, H., Karakaya, C., Chen, Y., Ricote, S., Jarry, A., Crumlin, E.J., Hook, D., Braun, R., et al. (2018). Highly durable, coking and sulfur tolerant, fuel-flexible protonic ceramic fuel cells. Nature *557*, 217–222. 10.1038/s41586-018-0082-6.

7. Shim, J.H. (2018). Ceramics breakthrough. Nat Energy *3*, 168–169. 10.1038/s41560-018-0110-7.

8. An, H., Lee, H.W., Kim, B.K., Son, J.W., Yoon, K.J., Kim, H., Shin, D., Ji, H. il, and Lee, J.H. (2018). A 5 × 5 cm2 protonic ceramic fuel cell with a power density of 1.3 W cm–2 at 600 °C. Nat Energy *3*, 870–875. 10.1038/s41560-018-0230-0.

9. Zhang, Y., Chen, B., Guan, D., Xu, M., Ran, R., Ni, M., Zhou, W., O'Hayre, R., and Shao, Z. (2021). Thermal-expansion offset for high-performance fuel cell cathodes. Nature *591*, 246–251. 10.1038/s41586-021-03264-1.

10. Shao, Z., and Haile, S.M. (2004). A high-performance cathode for the next generation of solid-oxide fuel cells. Nature *431*, 170–173. 10.1038/nature02863.

11. Wang, Z., Wang, Y., Wang, J., Song, Y., Robson, M.J., Seong, A., Yang, M., Zhang, Z., Belotti, A., Liu, J., et al. (2022). Rational design of perovskite ferrites as high-performance proton-conducting fuel cell cathodes. Nat Catal *5*, 777–787. 10.1038/s41929-022-00829-9.

12. Zhai, S., Xie, H., Cui, P., Guan, D., Wang, J., Zhao, S., Chen, B., Song, Y., Shao, Z., and Ni, M. (2022). A combined ionic Lewis-acid descriptor and machine-learning approach to prediction of efficient oxygen reduction electrodes for ceramic fuel cells. Nat Energy, 1–10. 10.1038/s41560-022-01098-3.

13. Duan, C., Tong, J., Shang, M., Nikodemski, S., Sanders, M., Ricote, S., Almansoori, A., and O'Hayre, R. (2015). Readily processed protonic ceramic fuel cells with high performance at low temperatures. Science (1979) *349*, 1321–1326. 10.1126/science.aab3987.

14. Song, Y., Chen, Y., Wang, W., Zhou, C., Zhong, Y., Yang, G., Zhou, W., Liu, M., and Shao, Z. (2019). Self-Assembled Triple-Conducting Nanocomposite as a Superior Protonic Ceramic Fuel Cell Cathode. Joule *3*, 2842–2853. 10.1016/j.joule.2019.07.004.

15. Bello, I.T., Yu, N., Song, Y., Wang, J., Chan, T., Zhao, S., Li, Z., Dai, Y., Yu, J., and Ni, M. (2022). Electrokinetic Insights into the Triple Ionic and Electronic Conductivity of a Novel Nanocomposite Functional Material for Protonic Ceramic Fuel Cells. Small *18*, 2203207. 10.1002/smll.202203207.

16. Montgomery, D.C. Design and analysis of experiments (Second edition. New York : Wiley, [1984] ©1984).

17. Lundstedt, T., Seifert, Elisabeth., Abramo, Lisbeth., Thelin, B., Nyström, Å., Pettersen, J., and Bergman, R. (1998). Experimental design and optimization. Chemometrics and Intelligent Laboratory Systems *42*, 3–40. 10.1016/S0169-7439(98)00065-3.

18. Calì, M., Santarelli, M.G.L., and Leone, P. (2007). Design of experiments for fitting regression models on the tubular SOFC CHP 100 kWe: Screening test, response surface analysis and optimization. Int J Hydrogen Energy *32*, 343–358. 10.1016/J.IJHYDENE.2006.05.021.

19. Barari, F., Morgan, R., and Barnard, P. (2014). A Design of Experiments (DOE) approach to optimise temperature measurement accuracy in Solid Oxide Fuel Cell (SOFC). J Phys Conf Ser *547*, 012004. 10.1088/1742-6596/547/1/012004.

20. Minitab, Inc. (2020). MINITAB.

21. Danilov, N., Lyagaeva, J., Vdovin, G., Medvedev, D., Demin, A., and Tsiakaras, P. (2017). Electrochemical Approach for Analyzing Electrolyte Transport Properties and Their Effect on Protonic Ceramic Fuel Cell Performance. ACS Appl Mater Interfaces *9*, 26874–26884. 10.1021/acsami.7b07472.

22. Rodriguez-Carvajal, J. (1990). FULLPROF: a program for Rietveld refinement and pattern matching analysis. In satellite meeting on powder diffraction of the XV congress of the IUCr.

23. Chen, D., and Shao, Z. (2011). Surface exchange and bulk diffusion properties of Ba0.5Sr 0.5Co0.8Fe0.2O3-δ mixed conductor. Int J Hydrogen Energy *36*, 6948–6956. 10.1016/j.ijhydene.2011.02.087.

24. Zhu, Y., Liu, D., Jing, H., Zhang, F., Zhang, X., Hu, S., Zhang, L., Wang, J., Zhang, L., Zhang, W., et al. (2022). Oxygen activation on Ba-containing perovskite materials. Sci Adv *8*, 4072. 10.1126/sciadv.abn4072.

25. Zohourian, R., Merkle, R., Raimondi, G., and Maier, J. (2018). Mixed-Conducting Perovskites as Cathode Materials for Protonic Ceramic Fuel Cells: Understanding the Trends in Proton Uptake. Adv Funct Mater *28*, 1–10. 10.1002/adfm.201801241.

26. Shannon, R.D. (1976). Revised effective ionic radii and systematic studies of interatomic distances in halides and chalcogenides. Acta Crystallographica Section A *32*, 751–767. 10.1107/S0567739476001551.

27. Papac, M., Stevanović, V., Zakutayev, A., and O'Hayre, R. (2021). Triple ionic–electronic conducting oxides for next-generation electrochemical devices. Nat Mater *20*, 301–313. 10.1038/s41563-020-00854-8.

28. Merkle, R., Hoedl, M.F., Raimondi, G., Zohourian, R., and Maier, J. (2021). Oxides with Mixed Protonic and Electronic Conductivity. Annu Rev Mater Res *51*, 461–493. 10.1146/annurev-matsci-091819-010219.

29. Han, D., Liu, X., Bjørheim, T.S., and Uda, T. (2021). Yttrium-Doped Barium Zirconate-Cerate Solid Solution as Proton Conducting Electrolyte: Why Higher Cerium Concentration Leads to Better Performance for Fuel Cells and Electrolysis Cells. Adv Energy Mater *11*, 1–11. 10.1002/aenm.202003149.

30. Yang, G., Su, C., Shi, H., Zhu, Y., Song, Y., Zhou, W., and Shao, Z. (2020). Toward reducing the operation temperature of solid oxide fuel cells: Our past 15 years of efforts in cathode development. Energy and Fuels *34*, 15169–15194. 10.1021/acs.energyfuels.0c01887.

31. Babilo, P., Uda, T., and Haile, S.M. (2007). Processing of yttrium-doped barium zirconate for high proton conductivity. J Mater Res *22*, 1322–1330. 10.1557/jmr.2007.0163.

32. Unger, L.S., Ruhl, R., Meffert, M., Niedrig, C., Menesklou, W., Wagner, S.F., Gerthsen, D., Bouwmeester, H.J.M., and Ivers-Tiffée, E. (2018). Yttrium doping of Ba0.5Sr0.5Co0.8Fe0.2O3-δ part II: Influence on oxygen transport and phase stability. J Eur Ceram Soc *38*, 2388–2395. 10.1016/j.jeurceramsoc.2017.12.042.

33. Pergolesi, D., Fabbri, E., D'Epifanio, A., di Bartolomeo, E., Tebano, A., Sanna, S., Licoccia, S., Balestrino, G., and Traversa, E. (2010). High proton conduction in grain-boundary-free yttrium-doped barium zirconate films grown by pulsed laser deposition. Nat Mater *9*, 846–852. 10.1038/nmat2837.

34. Chen, D., and Shao, Z. (2011). Surface exchange and bulk diffusion properties of. Int J Hydrogen Energy *36*, 6948–6956. 10.1016/j.ijhydene.2011.02.087.

35. Seong, A., Kim, J., Jeong, D., Sengodan, S., Liu, M., Choi, S., and Kim, G. (2021). Electrokinetic Proton Transport in Triple (H+/O2−/e−) Conducting Oxides as a Key Descriptor for Highly Efficient Protonic Ceramic Fuel Cells. Advanced Science *8*, 1–6. 10.1002/advs.202004099.

36. Guan, D., Zhang, K., Hu, Z., Wu, X., Chen, J.-L., Pao, C.-W., Guo, Y., Zhou, W., Shao, Z., Guan, D., et al. (2021). Exceptionally Robust Face-Sharing Motifs Enable Efficient and Durable Water Oxidation. Advanced Materials *33*, 2103392. 10.1002/ADMA.202103392.

37. Chen, H., Lim, C., Zhou, M., He, Z., Sun, X., Li, X., Ye, Y., Tan, T., Zhang, H., Yang, C., et al. (2021). Activating Lattice Oxygen in Perovskite Oxide by B-Site Cation Doping for Modulated Stability and Activity at Elevated Temperatures. Advanced Science *8*, 2102713. 10.1002/ADVS.202102713.

38. Bello, I.T., Song, Y., Yu, N., Li, Z., Zhao, S., Maradesa, A., Liu, T., Shao, Z., and Ni, M. (2023). Evaluation of the electrocatalytic performance of a novel nanocomposite cathode material for ceramic fuel cells. J Power Sources *560*, 232722. 10.1016/J.JPOWSOUR.2023.232722.

39. Zou, D., Yi, Y., Song, Y., Guan, D., Xu, M., Ran, R., Wang, W., Zhou, W., and Shao, Z. (2022). The BaCe 0.16 Y 0.04 Fe 0.8 O 3− δ nanocomposite: a new high-performance cobalt-free triple-conducting cathode for protonic ceramic fuel cells operating at reduced temperatures. J Mater Chem A Mater *10*, 5381–5390. 10.1039/D1TA10652J.

40. Tong, H., Fu, M., Yang, Y., Chen, F., and Tao, Z. (2022). A Novel Self-Assembled Cobalt-Free Perovskite Composite Cathode with Triple-Conduction for Intermediate Proton-Conducting Solid Oxide Fuel Cells. Adv Funct Mater *32*, 2209695. 10.1002/adfm.202209695.

41. Guan, D., Zhang, K., Zhou, W., and Shao, Z. (2021). Utilizing the charge-transfer model to design promising electrocatalysts. Curr Opin Electrochem *30*, 100805. 10.1016/j.coelec.2021.100805.

42. Ciucci, F., and Chen, C. (2015). Analysis of electrochemical impedance spectroscopy data using the distribution of relaxation times: A Bayesian and hierarchical Bayesian approach. Electrochim Acta *167*, 439–454. 10.1016/j.electacta.2015.03.123.

43. Wang, Q., Luo, T., Tong, Y., Dai, M., Miao, X.Y., Ricote, S., Zhan, Z., and Chen, M. (2022). Large-area protonic ceramic cells for hydrogen purification. Sep Purif Technol *295*, 121301. 10.1016/j.seppur.2022.121301.

44. Gunkel, F., Christensen, D. V., Chen, Y.Z., and Pryds, N. (2020). Oxygen vacancies: The (in)visible friend of oxide electronics. Appl Phys Lett *116*, 120505. 10.1063/1.5143309/570959.

45. Zhang, C., and Bristowe, P.D. (2013). First principles calculations of oxygen vacancy formation in barium-strontium-cobalt-ferrite. RSC Adv *3*, 12267–12274. 10.1039/C3RA41585F.

46. Bello, I.T., Yu, N., Zhai, S., Song, Y., Zhao, S., Cheng, C., Zhang, Z., and Ni, M. (2022). Effect of engineered lattice contraction and expansion on the performance and CO2 tolerance of Ba0.5Sr0.5Co0.7Fe0.3O3-δ functional material for intermediate temperature solid oxide fuel cells. Ceram Int *48*, 21457–21468. 10.1016/j.ceramint.2022.04.110.

Revolutionizing Material Design for Protonic Ceramic Fuel Cells: Bridging the Limitations of Conventional Experimental Screening and Machine Learning Methods

Idris Temitope Bello[a], Daqin Guan[a], Na Yu[a], Zheng Li[a], Yufei Song[b], Xi Chen[a], Siyuan Zhao[a], Qijiao He[a], Zongping Shao [c,]*, Meng Ni[a,]*

[a]Department of Building and Real Estate, Research Institute for Sustainable Urban Development (RISUD) & Research Institute for Smart Energy (RISE), The Hong Kong Polytechnic University, Hung Hom, Kowloon, Hong Kong, China

[b]Department of Mechanical and Aerospace Engineering, The Hong Kong University of Science and Technology, Clear Water Bay, Hong Kong, China

[c]WA School of Mines: Minerals, Energy and Chemical Engineering, Curtin University, Perth, Western Australia, 6845, Australia.

*Corresponding authors: meng.ni@polyu.edu.hk; shaozp@njtech.edu.cn

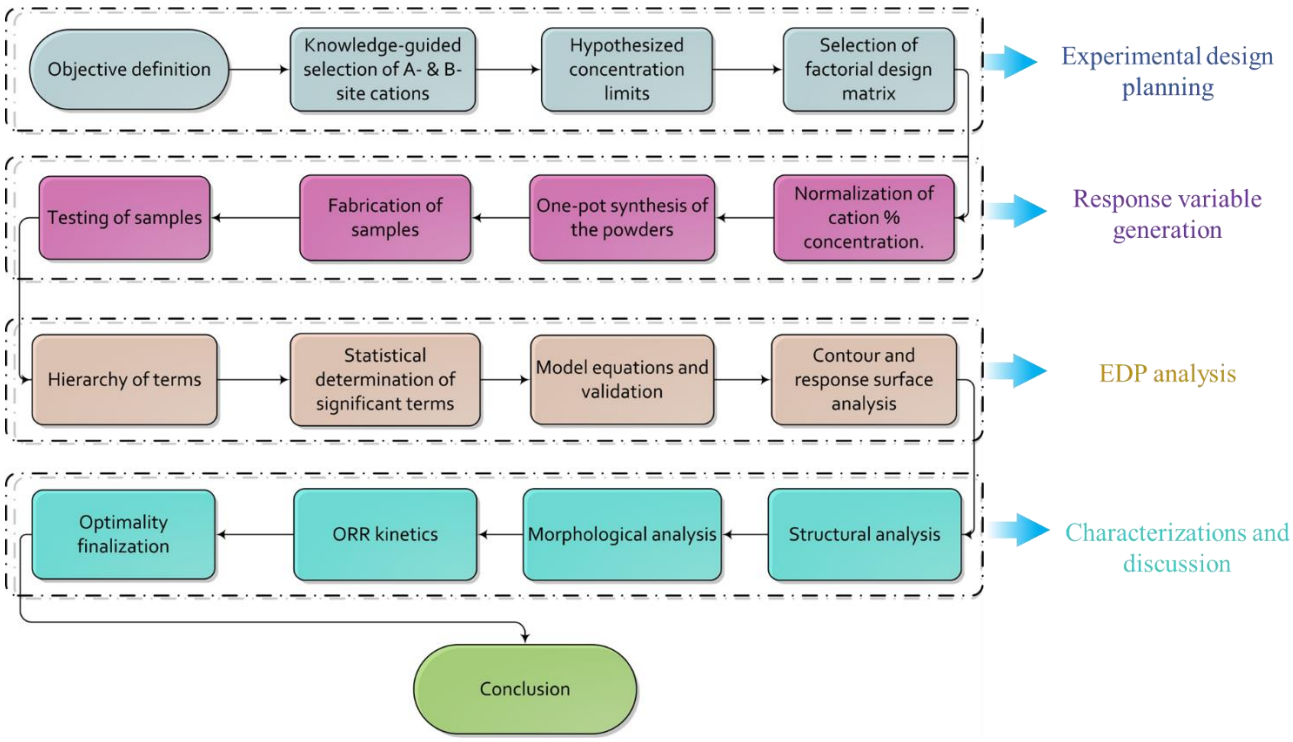

Figure S1: Comprehensive research framework for screening and optimizing the ORR of cathode materials for PCFCs using the EDP.

Table S1: Alias structure for the factors.

Factor	Name
A	Co
B	Ce
C	Fe
D	Y

Aliases
I + ABCD
A + BCD
B + ACD
C + ABD
D + ABC
AB + CD
AC + BD
AD + BC

Table S2: Hypothesized concentration of factor limits.

Cathode material series	Factors	Level (Concentration)	
		Lower limit (-1)	Upper limit (+1)
$BaCo_{\alpha}Ce_{\beta}Fe_{\gamma}Y_{\zeta}O_{3-\delta}$	Co	40	70
	Ce	10	40
	Fe	5	10
	Y	5	10
$Ba_{\alpha}Sr_{\beta}Co_{\gamma}Fe_{\zeta}O_{3-\delta}$	Ba	50	80
	Sr	20	50
	Co	40	90
	Fe	10	40

Table S3: Experimental design matrix with ASR and EC as the response variables with two replicates for $BaCo_{\alpha}Ce_{\beta}Fe_{\gamma}Y_{\zeta}O_{3-\delta}$ series.

	Factor levels (conc.)			
Run Order	Co	Ce	Fe	Y
1	40 (-1)	10 (-1)	10 (+1)	5 (-1)
2	40 (-1)	40 (+1)	10 (+1)	5 (-1)
3	40 (-1)	40 (+1)	10 (+1)	10 (+1)
4	70 (+1)	40 (+1)	10 (+1)	5 (-1)
5	40 (-1)	40 (+1)	5 (-1)	10 (+1)
6	40 (-1)	10 (-1)	5 (-1)	10 (+1)
7	70 (+1)	10 (-1)	5 (-1)	5 (-1)
8	40 (-1)	10 (-1)	5 (-1)	5 (-1)
9	70 (+1)	40 (+1)	5 (-1)	10 (+1)
10	70 (+1)	10 (-1)	5 (-1)	10 (+1)
11	40 (-1)	10 (-1)	10 (+1)	10 (+1)
12	70 (+1)	10 (-1)	10 (+1)	5 (-1)
13	70 (+1)	10 (-1)	5 (-1)	5 (-1)
14	70 (+1)	40 (+1)	5 (-1)	10 (+1)
15	70 (+1)	10 (-1)	10 (+1)	5 (-1)
16	70 (+1)	40 (+1)	5 (-1)	5 (-1)
17	40 (-1)	40 (+1)	5 (-1)	5 (-1)
18	70 (+1)	40 (+1)	10 (+1)	10 (+1)
19	70 (+1)	40 (+1)	5 (-1)	5 (-1)
20	40 (-1)	40 (+1)	5 (-1)	5 (-1)
21	70 (+1)	10 (-1)	10 (+1)	10 (+1)
22	70 (+1)	40 (+1)	10 (+1)	5 (-1)
23	40 (-1)	40 (+1)	5 (-1)	5 (-1)
24	40 (-1)	10 (-1)	5 (-1)	5 (-1)
25	70 (+1)	40 (+1)	10 (+1)	10 (+1)
26	70 (+1)	10 (-1)	10 (+1)	10 (+1)
27	40 (-1)	40 (+1)	10 (+1)	10 (+1)
28	40 (-1)	10 (-1)	5 (-1)	10 (+1)
29	70 (+1)	10 (-1)	5 (-1)	10 (+1)
30	40 (-1)	10 (-1)	10 (+1)	10 (+1)
31	40 (-1)	10 (-1)	10 (+1)	5 (-1)
32	40 (-1)	40 (+1)	10 (+1)	5 (-1)

Table S4: Experimental design matrix with ASR as the response variables with two replicates for $Ba_{\alpha}Sr_{\beta}Co_{\gamma}Fe_{\varsigma}O_{3-\delta}$ series.

	Factor levels (conc.)			
Run Order	Ba	Sr	Co	Fe
1	80(+1)	20(-1)	40(-1)	10(-1)
2	80(+1)	20(-1)	40(-1)	10(-1)
3	50(-1)	50(+1)	40(-1)	40(+1)
4	80(+1)	50(+1)	40(-1)	10(-1)
5	80(+1)	20(-1)	90(+1)	40(+1)
6	80(+1)	50(+1)	40(-1)	40(+1)
7	80(+1)	50(+1)	40(-1)	10(-1)
8	50(-1)	20(-1)	90(+1)	10(-1)
9	80(+1)	50(+1)	90(+1)	40(+1)
10	80(+1)	50(+1)	40(-1)	40(+1)
11	50(-1)	20(-1)	40(-1)	10(-1)
12	80(+1)	50(+1)	90(+1)	10(-1)
13	80(+1)	20(-1)	90(+1)	10(-1)
14	50(-1)	20(-1)	90(+1)	40(+1)
15	80(+1)	20(-1)	40(-1)	40(+1)
16	50(-1)	50(+1)	90(+1)	40(+1)
17	50(-1)	50(+1)	40(-1)	10(-1)
18	50(-1)	50(+1)	90(+1)	10(-1)
19	50(-1)	20(-1)	90(+1)	10(-1)
20	50(-1)	50(+1)	90(+1)	10(-1)
21	50(-1)	20(-1)	90(+1)	40(+1)
22	50(-1)	20(-1)	40(-1)	10(-1)
23	80(+1)	20(-1)	90(+1)	10(-1)
24	50(-1)	20(-1)	40(-1)	40(+1)
25	80(+1)	50(+1)	90(+1)	40(+1)
26	80(+1)	50(+1)	90(+1)	10(-1)
27	50(-1)	50(+1)	40(-1)	10(-1)
28	80(+1)	20(-1)	90(+1)	40(+1)
29	50(-1)	50(+1)	90(+1)	40(+1)
30	50(-1)	50(+1)	40(-1)	40(+1)
31	80(+1)	20(-1)	40(-1)	40(+1)
32	50(-1)	20(-1)	40(-1)	40(+1)

Table S5: Experimental design matrix with one replicate for the BCCFY series.

RunOrder	Co	Ce	Fe	Y
1	70 (+1)	40 (+1)	10 (+1)	10 (+1)
2	40 (-1)	10 (-1)	10 (+1)	10 (+1)
3	40 (-1)	10 (-1)	5 (-1)	5 (-1)
4	70 (+1)	10 (-1)	10 (+1)	5 (-1)
5	40 (-1)	40 (+1)	10 (+1)	5 (-1)
6	70 (+1)	40 (+1)	5 (-1)	5 (-1)
7	70 (+1)	10 (-1)	5 (-1)	10 (+1)
8	40 (-1)	40 (+1)	5 (-1)	10 (+1)

Table S6: Matrix of experiments for $BaCo_{\alpha}Ce_{\beta}Fe_{\gamma}Y_{\zeta}O_{3-\delta}$.

Sample No.	Co	Ce	Fe	Y	$BaCo_{\alpha}Ce_{\beta}Fe_{\gamma}Y_{\zeta}O_{3-\delta}$			
					α	β	γ	ζ
					(% mol. Concentration)			
1	-1	-1	-1	-1	66.67	16.67	8.33	8.33
2	-1	-1	+1	+1	57.14	14.29	14.29	14.29
3	-1	+1	-1	+1	42.11	42.11	5.26	10.53
4	-1	+1	+1	-1	42.11	42.11	10.53	5.26
5	+1	-1	-1	+1	73.68	10.53	5.26	10.53
6	+1	-1	+1	-1	73.68	10.53	10.53	5.26
7	+1	+1	-1	-1	58.33	33.33	4.17	4.17
8	+1	+1	+1	+1	53.85	30.77	7.69	7.69
9	-1	-1	+1	-1	61.54	15.38	15.38	7.69
10	+1	+1	+1	-1	56.00	32.00	8.00	4.00
11	-1	-1	-1	+1	61.54	15.38	7.69	15.38
12	-1	+1	-1	-1	44.44	44.44	5.56	5.56
13	-1	+1	+1	+1	40.00	40.00	10.00	10.00
14	+1	-1	-1	-1	77.78	11.11	5.56	5.56
15	+1	-1	+1	+1	70.00	10.00	10.00	10.00
16	+1	+1	-1	+1	56.00	32.00	4.00	8.00

Table S7: Matrix of experiments $Ba_{\alpha}Sr_{\beta}Co_{\gamma}Fe_{\zeta}O_{3-\delta}$ series.

Sample No.	Ba	Sr	Co	Fe	$Ba_{\alpha}Sr_{\beta}Co_{\gamma}Fe_{\zeta}O_{3-\delta}$			
					α	β	γ	ζ
					(% mol. Concentration)			
1	+1	-1	-1	-1	80.00	20.00	80.00	20.00
2	+1	-1	-1	+1	80.00	20.00	50.00	50.00
3	+1	-1	+1	-1	80.00	20.00	90.00	10.00
4	+1	-1	+1	+1	80.00	20.00	69.23	30.77
5	+1	+1	-1	-1	61.54	38.46	80.00	20.00
6	+1	+1	-1	+1	61.54	38.46	50.00	50.00
7	+1	+1	+1	-1	61.54	38.46	90.00	10.00
8	+1	+1	+1	+1	61.54	38.46	69.23	30.77
9	-1	-1	-1	-1	71.43	28.57	80.00	20.00
10	-1	-1	-1	+1	71.43	28.57	50.00	50.00
11	-1	-1	+1	-1	71.43	28.57	90.00	10.00
12	-1	-1	+1	+1	71.43	28.57	69.23	30.77
13	-1	+1	-1	-1	50.00	50.00	80.00	20.00
14	-1	+1	-1	+1	50.00	50.00	50.00	50.00
15	-1	+1	+1	-1	50.00	50.00	90.00	10.00
16	-1	+1	+1	+1	50.00	50.00	69.23	30.77

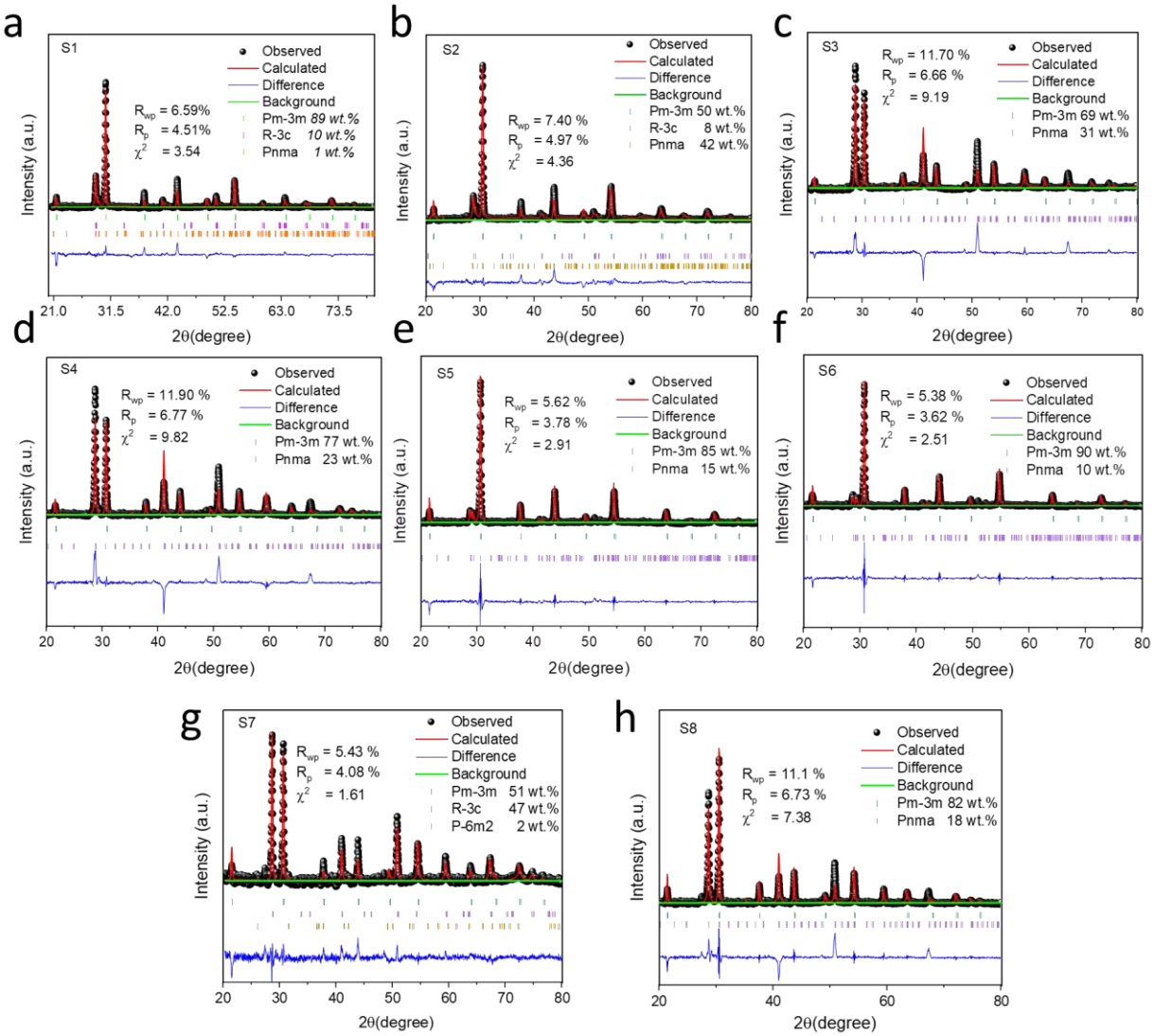

Figure S2: Refinement of the half fraction of the samples from Table S6 (a) S1 (b) S2 (c) S3 (d) S4 (e) S5 (f) S6 (g) S7 (h) S8

Table S8: Estimated lattice parameters of all the samples

Sample	Space groups	Lattice Parameters					
		a	b	c	α	β	γ
S1	Pm-3m	4.12147	4.12147	4.12147	90.0000	90.0000	90.0000
	R-3c	6.22155	6.22155	14.79442	90.0000	90.0000	120.0000
	Pnma	6.15758	8.79433	6.21294	90.0000	90.0000	90.0000
S2	Pm-3m	4.14510	4.14510	4.14510	90.0000	90.0000	90.0000
	R-3c	6.20351	6.20351	14.92609	90.0000	90.0000	120.0000
	Pnma	6.24232	8.60778	5.86177	90.0000	90.0000	90.0000
S3	Pm-3m	4.15555	4.15555	4.15555	90.0000	90.0000	90.0000
	Pnma	6.21055	6.18729	8.78271	90.0000	90.0000	90.0000
S4	Pm-3m	4.11156	4.11156	4.11156	90.0000	90.0000	90.0000
	Pnma	6.21541	6.19532	8.79176	90.0000	90.0000	90.0000
S5	Pm-3m	4.12354	4.12354	4.12354	90.0000	90.0000	90.0000
	Pnma	6.19715	6.08515	8.80205	90.0000	90.0000	90.0000
S6	Pm-3m	4.10415	4.10415	4.10415	90.0000	90.0000	90.0000
	Pnma	6.20731	6.06088	8.66242	90.0000	90.0000	90.0000
S7	Pm-3m	4.11954	4.11954	4.11954	90.0000	90.0000	90.0000
	R-3c	6.21758	6.21758	6.21758	90.0000	90.0000	120.0000
	P-6m2	5.66698	5.66698	4.76921	90.0000	90.0000	120.0000
S8	Pm-3m	4.13915	4.13915	4.13915	90.0000	90.0000	90.0000
	Pnma	6.21760	6.22098	8.79184	90.0000	90.0000	90.0000

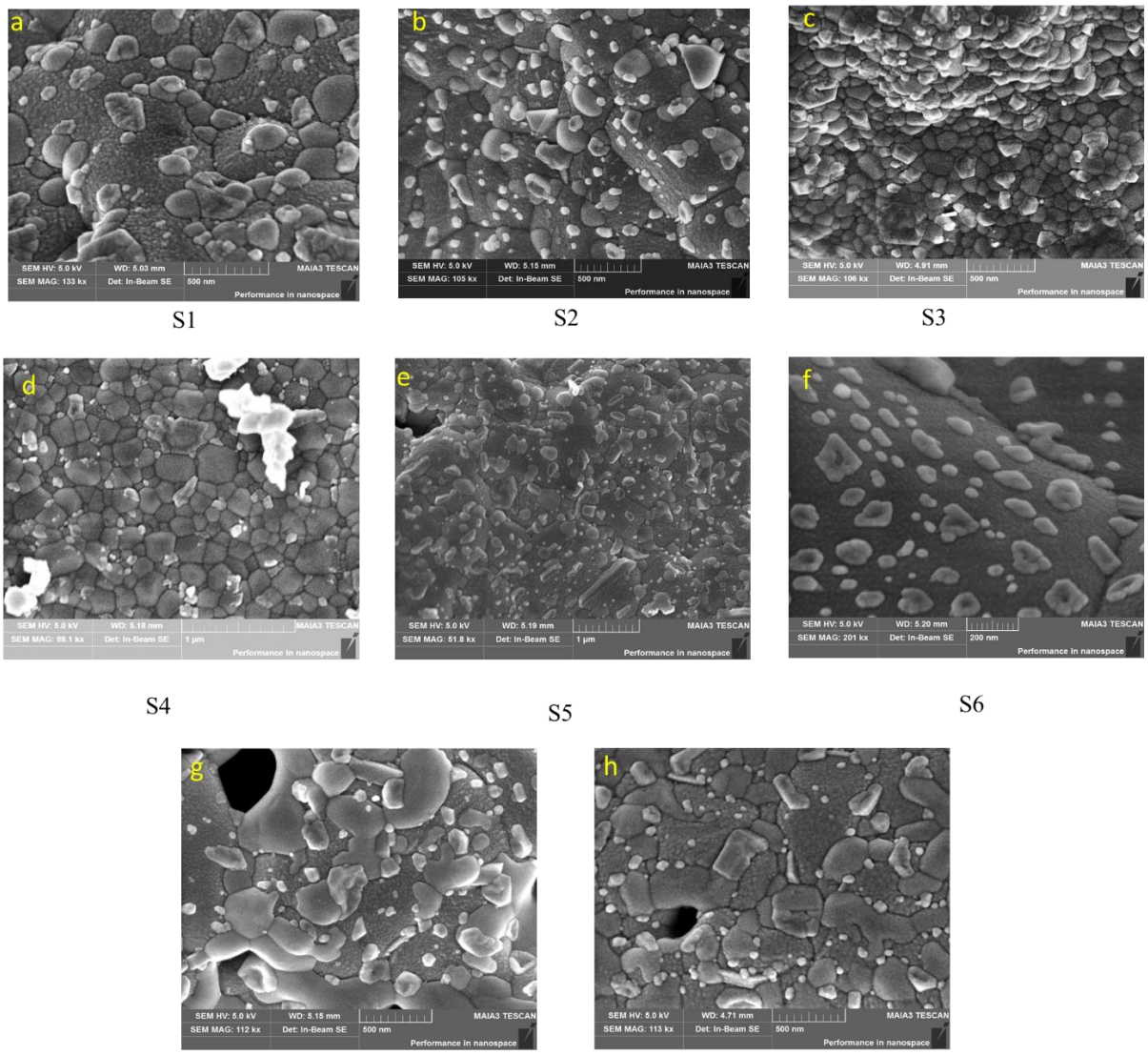

Figure S3: SEM images of (a) $BaCo_{0.667}Ce_{0.167}Fe_{0.083}Y_{0.083}O_{3-\delta}$ (b) $BaCo_{0.571}Ce_{0.143}Fe_{0.143}Y_{0.143}O_{3-\delta}$(c) $BaCo_{0.421}Ce_{0.421}Fe_{0.053}Y_{0.105}O_{3-\delta}$ (d) $BaCo_{0.421}Ce_{0.421}Fe_{0.105}Y_{0.053}O_{3-\delta}$ (e) $BaCo_{0.737}Ce_{0.105}Fe_{0.053}Y_{0.105}O_{3-\delta}$ (f) $BaCo_{0.737}Ce_{0.105}Fe_{0.105}Y_{0.053}O_{3-\delta}$ (g) $BaCo_{0.583}Ce_{0.333}Fe_{0.042}Y_{0.042}O_{3-\delta}$ (h) $BaCo_{0.538}Ce_{0.308}Fe_{0.077}Y_{0.077}O_{3-\delta}$

Table S9: Matrix of results with D_{chem} and k_{chem} as responses for BCCFY family.

					D_{chem} (cm^2 s^{-1})				k_{chem} (cm s^{-1})			
RunOrder	Co	Ce	Fe	Y	650 °C	600 °C	550 °C	500 °C	650 °C	600 °C	550 °C	500 °C
1	70	40	10	10	5.72E-05	3.07E-05	1.46E-05	6.94E-06	0.000565	0.000307	0.000144	6.84E-05
2	40	10	10	10	5.95E-05	3.62E-05	1.92E-05	9.27E-06	0.000615	0.000375	0.000195	9.38E-05
3	40	10	5	5	0.000121	6.3E-05	3.36E-05	1.43E-05	0.00118	0.000613	0.000326	0.000141
4	70	10	10	5	6.67E-05	3.39E-05	1.54E-05	6.55E-06	0.000636	0.000319	0.000147	6.45E-05
5	40	40	10	5	7.17E-05	3.43E-05	1.81E-05	8.93E-06	0.000774	0.000367	0.000183	8.9E-05
6	70	40	5	5	5.51E-05	3.68E-05	2.71E-05	2.13E-05	0.000588	0.000389	0.000285	0.000223
7	70	10	5	10	0.000108	5.16E-05	2.23E-05	8.65E-06	0.001078	0.000526	0.000232	8.59E-05
8	40	40	5	10	2.07E-05	1.33E-05	7.29E-06	5.62E-06	0.000197	0.000128	6.95E-05	5.26E-05

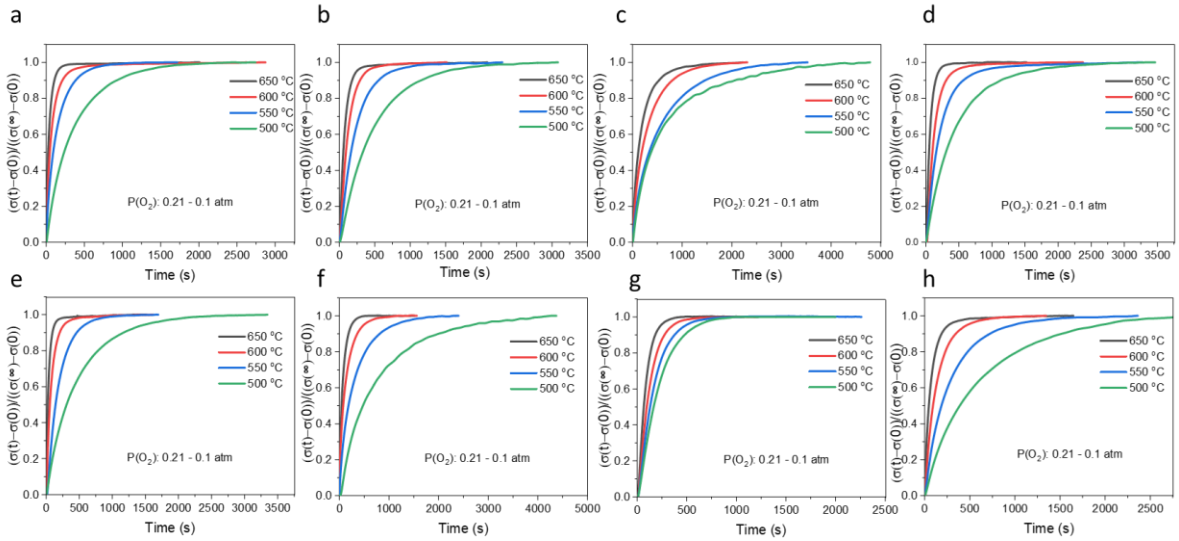

Figure S4: Electrical relaxation conductivity results for (a) S1 (b) S2 (c) S3 (d) S4 (e) S5 (f) S6 (g) S7 (h) S8.

Note: The ECR curves for samples S3 and S6 do not reach full equilibrium. While included here for completeness, the derived D_{chem} and K_{chem} values may be non-ideal and should be interpreted with caution. Ensuring fully equilibrated ECR measurements will be vital in future studies applying EDP for cathode development.

Table S10: Matrix of results with ASR and EC as responses for BCCFY series.

	Factor levels (conc.)				ASR responses (Ω cm^2)				Conductivity responses (S cm^{-1})			
Run Order	Co	Ce	Fe	Y	650 ºC	600 ºC	550 ºC	500 ºC	650 ºC	600 ºC	550 ºC	500 ºC
1	40	10	10	5	0.085	0.182	0.448	1.289	1.845	1.694	1.554	1.432
2	40	40	10	5	0.216	0.493	0.973	2.455	1.428	1.317	1.200	1.088
3	40	40	10	10	0.194	0.382	0.921	2.549	0.478	0.424	0.366	0.308
4	70	40	10	5	0.117	0.237	0.564	1.555	2.242	2.025	1.837	1.651
5	40	40	5	10	0.559	1.515	4.082	10.859	0.657	0.555	0.473	0.390
6	40	10	5	10	0.176	0.314	0.783	2.108	1.069	0.925	0.812	0.713
7	70	10	5	5	0.176	0.340	0.614	1.952	4.777	4.250	3.801	3.408
8	40	10	5	5	0.096	0.177	0.422	1.046	3.120	2.785	2.501	2.233
9	70	40	5	10	0.148	0.256	0.589	1.933	1.553	1.370	1.207	1.086
10	70	10	5	10	0.201	0.472	1.203	3.228	3.564	3.155	2.787	2.469
11	40	10	10	10	0.142	0.252	0.635	1.685	1.584	1.414	1.264	1.123
12	70	10	10	5	0.108	0.217	0.561	1.533	4.841	4.433	4.151	3.754
13	70	10	5	5	0.191	0.268	0.605	1.883	4.777	4.250	3.801	3.408
14	70	40	5	10	0.166	0.274	0.604	1.507	1.553	1.370	1.207	1.087
15	70	10	10	5	0.094	0.200	0.557	1.559	4.841	4.433	4.151	3.754
16	70	40	5	5	0.174	0.310	0.713	1.782	6.342	5.852	5.599	5.286
17	40	40	5	5	0.129	0.334	0.815	2.163	1.026	0.922	0.833	0.753
18	70	40	10	10	0.098	0.214	0.594	1.867	1.892	1.699	1.532	1.373
19	70	40	5	5	0.125	0.297	0.845	2.692	6.283	5.872	5.203	5.286
20	40	40	5	5	0.147	0.314	0.805	2.221	1.026	0.922	0.833	0.753
21	70	10	10	10	0.345	0.650	1.222	3.595	2.418	2.150	1.930	1.739
22	70	40	10	5	0.104	0.236	0.564	1.537	2.242	2.025	1.837	1.651
23	40	40	5	10	0.555	1.517	4.054	10.654	0.657	0.555	0.473	0.390
24	40	10	5	5	0.078	0.161	0.364	1.049	3.133	2.884	2.491	2.230
25	70	40	10	10	0.088	0.211	0.479	1.579	1.892	1.699	1.532	1.373
26	70	10	10	10	0.358	0.564	1.158	3.376	2.418	2.150	1.930	1.739
27	40	40	10	10	0.178	0.357	0.925	2.662	0.478	0.424	0.366	0.308
28	40	10	5	10	0.172	0.332	0.784	2.091	1.069	0.925	0.812	0.713
29	70	10	5	10	0.182	0.491	1.313	3.942	3.564	3.155	2.787	2.469
30	40	10	10	10	0.110	0.246	0.695	2.160	1.584	1.584	1.414	1.264
31	40	10	10	5	0.085	0.215	0.578	1.707	1.957	1.652	1.594	1.444
32	40	40	10	5	0.146	0.331	0.933	2.698	1.428	1.317	1.200	1.088

Table S11: Matrix of results with ASR as responses for BSCF series.

	Factor levels (conc.)				ASR responses (Ω cm^2)			
Run Order	Ba	Sr	Co	Fe	650 ºC	600 ºC	550 ºC	500 ºC
1	80	20	40	10	0.07077	0.15158	0.388316	1.25266
2	80	20	40	10	0.06833	0.15085	0.39277	1.266401
3	50	50	40	40	0.033091	0.115925	0.260738	0.812083
4	80	50	40	10	0.091099	0.188824	0.436382	1.17157
5	80	20	90	40	0.102227	0.286788	0.681537	1.836037
6	80	50	40	40	0.069355	0.157589	0.374563	1.060928
7	80	50	40	10	0.088678	0.188074	0.437324	1.181386
8	50	20	90	10	0.030762	0.117032	0.327573	1.158896
9	80	50	90	40	0.049322	0.107396	0.270323	0.731228
10	80	50	40	40	0.067746	0.152526	0.373346	1.055433
11	50	20	40	10	0.017799	0.045585	0.126683	0.472531
12	80	50	90	10	0.066187	0.120034	0.307461	1.04562
13	80	20	90	10	0.040302	0.11795	0.331117	1.152773
14	50	20	90	40	0.042555	0.120831	0.305946	0.973282
15	80	20	40	40	0.016642	0.049145	0.136037	0.46421
16	50	50	90	40	0.126715	0.316002	0.897726	3.080105
17	50	50	40	10	0.037648	0.093317	0.227815	0.742218
18	50	50	90	10	0.032187	0.08155	0.223588	0.737152
19	50	20	90	10	0.037263	0.117067	0.327949	1.161368
20	50	50	90	10	0.03345	0.080902	0.218599	0.735781
21	50	20	90	40	0.044529	0.121522	0.309557	0.965236
22	50	20	40	10	0.017977	0.044757	0.130934	0.47155
23	80	20	90	10	0.046429	0.117825	0.335281	1.163763
24	50	20	40	40	0.053313	0.13343	0.299831	0.962803
25	80	50	90	40	0.050903	0.107938	0.266233	0.731228
26	80	50	90	10	0.060563	0.119308	0.307716	0.988315
27	50	50	40	10	0.038607	0.093654	0.230849	0.732562
28	80	20	90	40	0.114214	0.290701	0.686875	1.852875
29	50	50	90	40	0.127445	0.318906	0.918803	3.072647
30	50	50	40	40	0.037564	0.114822	0.257441	0.768123
31	80	20	40	40	0.01639	0.04544	0.133544	0.451218
32	50	20	40	40	0.054346	0.137611	0.293747	0.97183

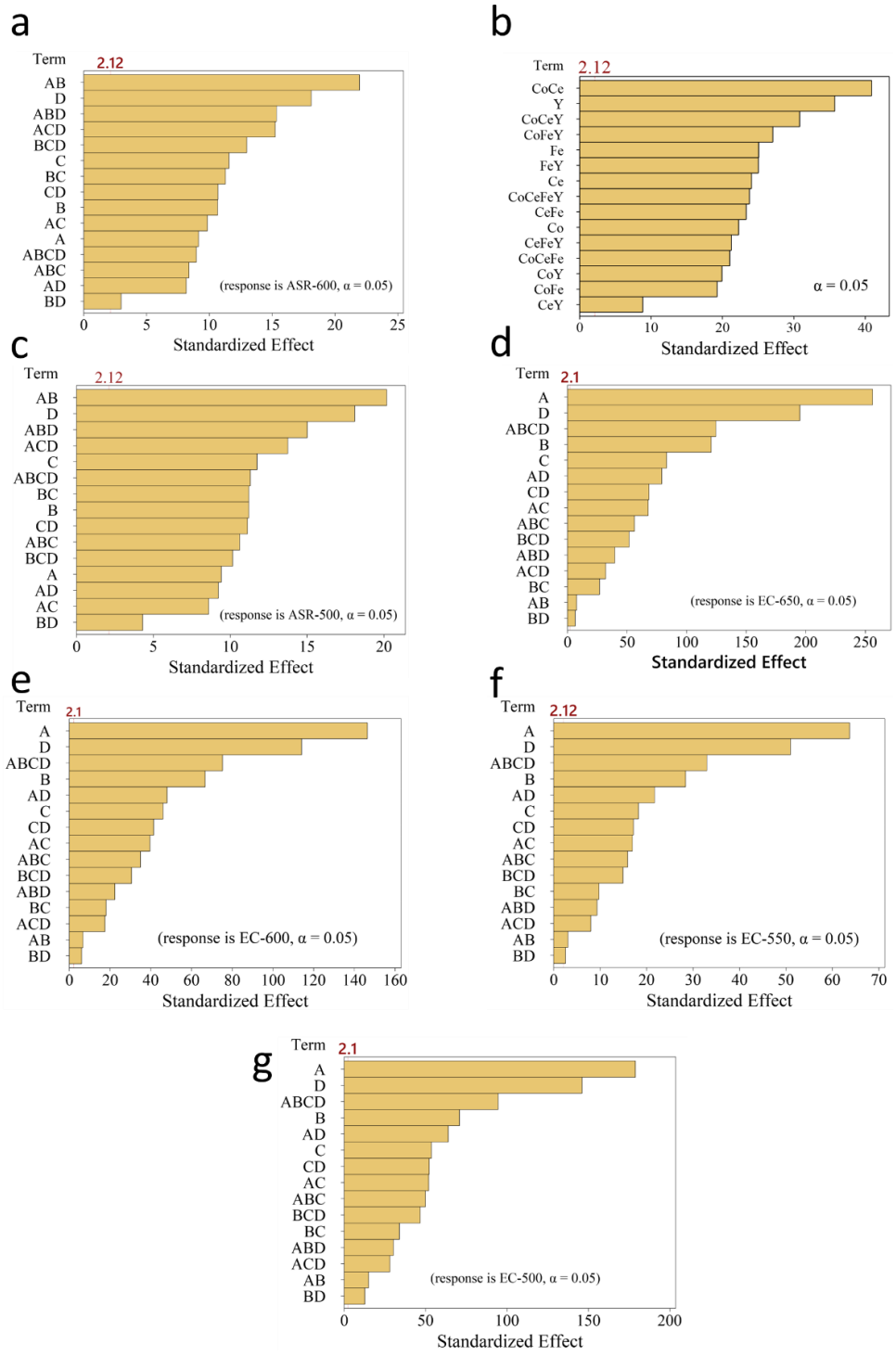

Figure S5: Pareto chart of the absolute values of standardized effects of each model term with a significance level of 0.05. ASR at (a) 600 ^{o}C (b) 550 ^{o}C (c) 500 ^{o}C. Electronic conductivity at (d) 650 ^{o}C (e) 600 ^{o}C (f) 550 ^{o}C and (g) 500 ^{o}C. A = Co, B = Ce, C = Fe, and D = Y

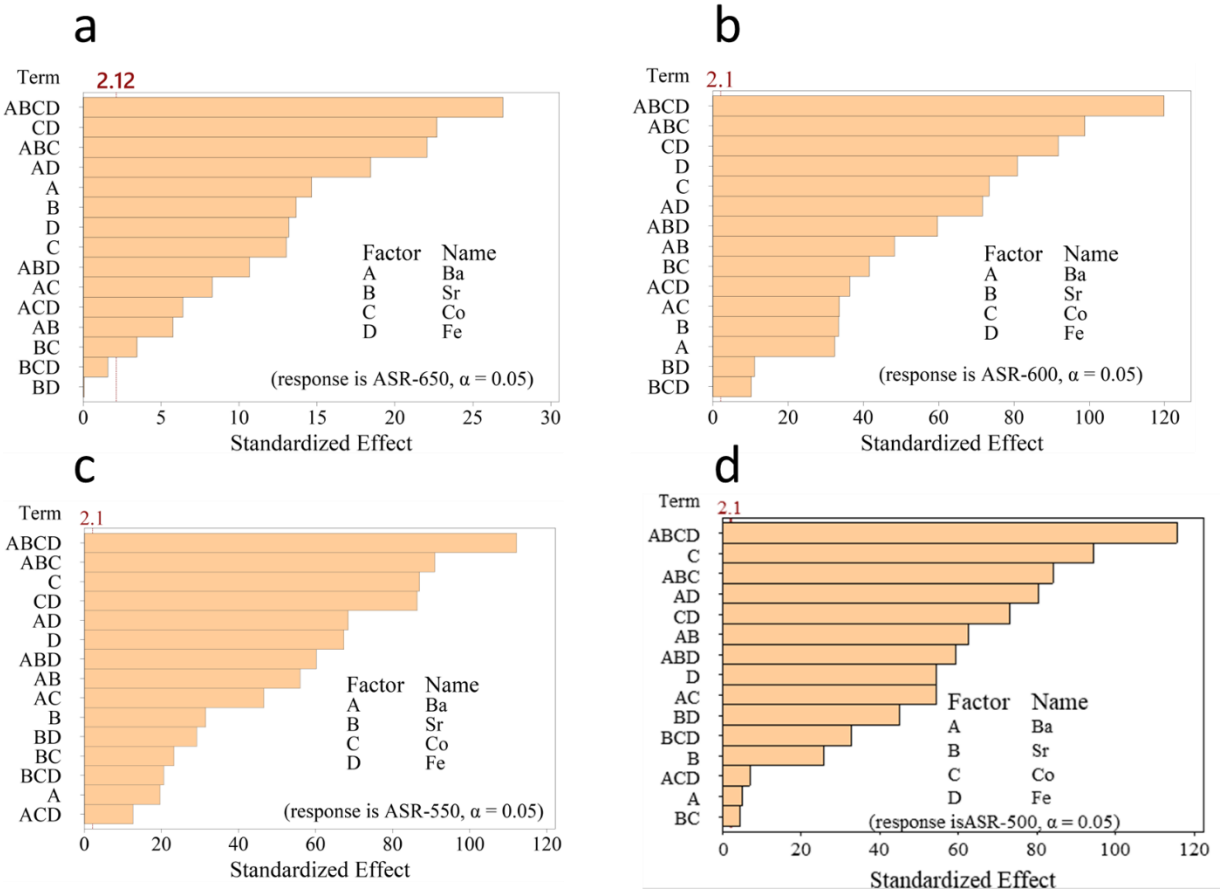

Figure S6: Pareto chart of the absolute values of standardized effects of each model term with a significance level of 0.05. ASR at (a) 600 ºC (b) 550 ºC (c) 500 ºC. Electronic conductivity at (d) 650 ºC (e) 600 ºC (f) 550 ºC and (g) 500 ºC. A = Ba, B = Sr, C = Co, and D = Fe

Supplementary note 1

Lenth's Pseudo-Standard Error (PSE) creates an estimate of the residual standard error by using effects that are not active. According to this approach, if there are n rows, n-1 contrasts denoted as $\hat{C}_i$ where i = 1,…, n-1

To estimate the PSE, the expression, $v = 1.5\left[median_{i=1,\ldots,n-1}\left|\hat{C}_i\right|\right]$ is first used to calculate v, the Lenth's PSE is calculated using the expression $PSE = 1.5\left[median_{|\hat{C}_i|<2.5v}\left|\hat{C}_i\right|\right]$ which is based on effects that are probably inactive[5].

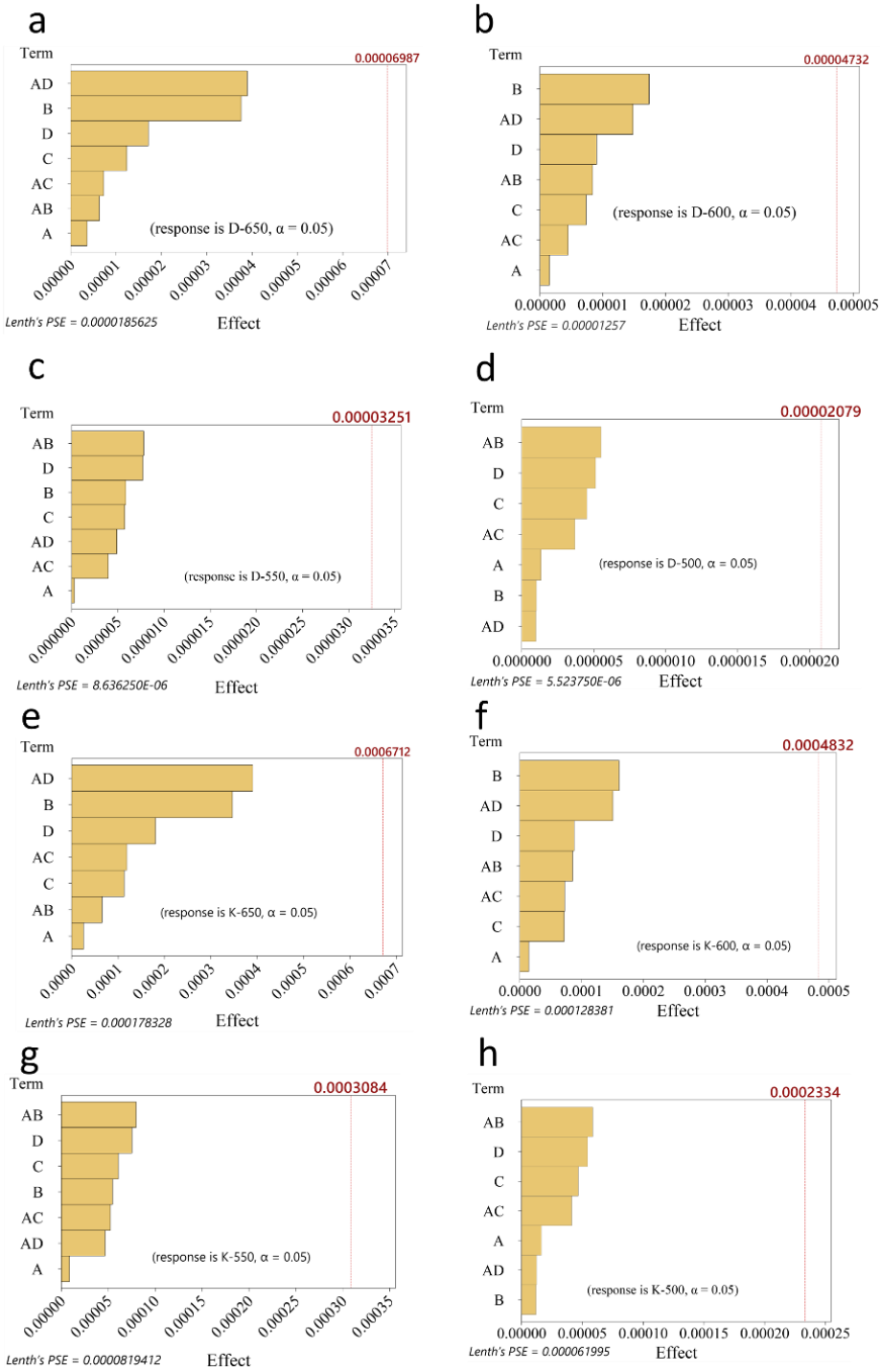

Figure S7: Pareto chart of the absolute values of the effects of each model term with a significance level of 0.05. D_{chem} at (a) 650 ºC (b) 600 ºC (c) 550 ºC (d) 500 ºC. k_{chem} at (e) 650 ºC (f) 600 ºC (g) 550 ºC and (h) 500 ºC. A = Co, B = Ce, C = Fe, and D = Y.

Table S12: Coefficients of effects causing variability in ASR of BCCFY series at 650 ^{o}C

Term	Effect	Coef	SE Coef	T-Value	P-Value	VIF
Constant		0.17946	0.00325	55.27	0.000	
Co	-0.02487	-0.01243	0.00325	-3.83	0.001	1.00
Ce	0.03412	0.01706	0.00325	5.25	0.000	1.00
Fe	-0.05052	-0.02526	0.00325	-7.78	0.000	1.00
Y	0.10005	0.05002	0.00325	15.41	0.000	1.00
Co*Ce	-0.11360	-0.05680	0.00325	-17.49	0.000	1.00
Co*Fe	0.04418	0.02209	0.00325	6.80	0.000	1.00
Co*Y	-0.03805	-0.01902	0.00325	-5.86	0.000	1.00
Ce*Fe	-0.05712	-0.02856	0.00325	-8.80	0.000	1.00
Ce*Y	0.00349	0.00175	0.00325	0.54	0.598	1.00
Fe*Y	-0.03039	-0.01520	0.00325	-4.68	0.000	1.00
Co*Ce*Fe	0.01213	0.00606	0.00325	1.87	0.080	1.00
Co*Ce*Y	-0.07065	-0.03532	0.00325	-10.88	0.000	1.00
Co*Fe*Y	0.08479	0.04239	0.00325	13.06	0.000	1.00
Ce*Fe*Y	-0.07942	-0.03971	0.00325	-12.23	0.000	1.00
Co*Ce*Fe*Y	0.01258	0.00629	0.00325	1.94	0.071	1.00

Table 13: Coefficients of effects causing variability in ASR of BCCFY series at 600 ºC.

Term	Effect	Coef	SE Coef	T-Value	P-Value	VIF
Constant		0.38627	0.00645	59.87	0.000	
Co	-0.11777	-0.05889	0.00645	-9.13	0.000	1.00
Ce	0.13740	0.06870	0.00645	10.65	0.000	1.00
Fe	-0.14911	-0.07456	0.00645	-11.56	0.000	1.00
Y	0.23354	0.11677	0.00645	18.10	0.000	1.00
Co*Ce	-0.28308	-0.14154	0.00645	-21.94	0.000	1.00
Co*Fe	0.12683	0.06342	0.00645	9.83	0.000	1.00
Co*Y	-0.10521	-0.05260	0.00645	-8.15	0.000	1.00
Ce*Fe	-0.14550	-0.07275	0.00645	-11.28	0.000	1.00
Ce*Y	0.03836	0.01918	0.00645	2.97	0.009	1.00
Fe*Y	-0.13786	-0.06893	0.00645	-10.68	0.000	1.00
Co*Ce*Fe	0.10814	0.05407	0.00645	8.38	0.000	1.00
Co*Ce*Y	-0.19792	-0.09896	0.00645	-15.34	0.000	1.00
Co*Fe*Y	0.19653	0.09827	0.00645	15.23	0.000	1.00
Ce*Fe*Y	-0.16733	-0.08367	0.00645	-12.97	0.000	1.00
Co*Ce*Fe*Y	0.11555	0.05777	0.00645	8.95	0.000	1.00

Table S14: Coefficients of effects causing variability in ASR of BCCFY series at 550 ^{o}C.

Term	Effect	Coef	SE Coef	T-Value	P-Value	VIF
Constant		0.95011	0.00846	112.26	0.000	
Co	-0.37704	-0.18852	0.00846	-22.28	0.000	1.00
Ce	0.40755	0.20377	0.00846	24.08	0.000	1.00
Fe	-0.42437	-0.21218	0.00846	-25.07	0.000	1.00
Y	0.60495	0.30247	0.00846	35.74	0.000	1.00
Co*Ce	-0.69243	-0.34621	0.00846	-40.91	0.000	1.00
Co*Fe	0.32589	0.16295	0.00846	19.25	0.000	1.00
Co*Y	-0.33753	-0.16877	0.00846	-19.94	0.000	1.00
Ce*Fe	-0.39504	-0.19752	0.00846	-23.34	0.000	1.00
Ce*Y	0.14948	0.07474	0.00846	8.83	0.000	1.00
Fe*Y	-0.42370	-0.21185	0.00846	-25.03	0.000	1.00
Co*Ce*Fe	0.35603	0.17801	0.00846	21.03	0.000	1.00
Co*Ce*Y	-0.52196	-0.26098	0.00846	-30.84	0.000	1.00
Co*Fe*Y	0.45798	0.22899	0.00846	27.06	0.000	1.00
Ce*Fe*Y	-0.35978	-0.17989	0.00846	-21.26	0.000	1.00
Co*Ce*Fe*Y	0.40255	0.20128	0.00846	23.78	0.000	1.00

Table S15: Coefficients of effects causing variability in ASR of BCCFY series at 500 ^{o}C.

Term	Effect	Coef	SE Coef	T-Value	P-Value	VIF
Constant		2.6535	0.0461	57.60	0.000	
Co	-0.8671	-0.4336	0.0461	-9.41	0.000	1.00
Ce	1.0319	0.5160	0.0461	11.20	0.000	1.00
Fe	-1.0814	-0.5407	0.0461	-11.74	0.000	1.00
Y	1.6671	0.8336	0.0461	18.09	0.000	1.00
Co*Ce	-1.8588	-0.9294	0.0461	-20.17	0.000	1.00
Co*Fe	0.7918	0.3959	0.0461	8.59	0.000	1.00
Co*Y	-0.8504	-0.4252	0.0461	-9.23	0.000	1.00
Ce*Fe	-1.0321	-0.5161	0.0461	-11.20	0.000	1.00
Ce*Y	0.3961	0.1981	0.0461	4.30	0.001	1.00
Fe*Y	-1.0246	-0.5123	0.0461	-11.12	0.000	1.00
Co*Ce*Fe	0.9779	0.4889	0.0461	10.61	0.000	1.00
Co*Ce*Y	-1.3829	-0.6914	0.0461	-15.01	0.000	1.00
Co*Fe*Y	1.2663	0.6331	0.0461	13.74	0.000	1.00
Ce*Fe*Y	-0.9358	-0.4679	0.0461	-10.16	0.000	1.00
Co*Ce*Fe*Y	1.0412	0.5206	0.0461	11.30	0.000	1.00

Table S16: Coefficients of effects causing variability in electronic conductivity of BCCFY series at 650 ^{o}C.

Term	Effect	Coef	SE Coef	T-Value	P-Value	VIF
Constant		2.42935	0.00399	609.34	0.000	
Co	2.04118	1.02059	0.00399	255.99	0.000	1.00
Ce	-0.96161	-0.48080	0.00399	-120.60	0.000	1.00
Fe	-0.66276	-0.33138	0.00399	-83.12	0.000	1.00
Y	-1.55491	-0.77746	0.00399	-195.00	0.000	1.00
Co*Ce	0.06111	0.03056	0.00399	7.66	0.000	1.00
Co*Fe	-0.54060	-0.27030	0.00399	-67.80	0.000	1.00
Co*Y	-0.63136	-0.31568	0.00399	-79.18	0.000	1.00
Ce*Fe	-0.21448	-0.10724	0.00399	-26.90	0.000	1.00
Ce*Y	-0.05237	-0.02618	0.00399	-6.57	0.000	1.00
Fe*Y	0.54485	0.27243	0.00399	68.33	0.000	1.00
Co*Ce*Fe	-0.44789	-0.22394	0.00399	-56.17	0.000	1.00
Co*Ce*Y	-0.31598	-0.15799	0.00399	-39.63	0.000	1.00
Co*Fe*Y	0.25505	0.12752	0.00399	31.99	0.000	1.00
Ce*Fe*Y	0.41245	0.20623	0.00399	51.73	0.000	1.00
Co*Ce*Fe*Y	0.99293	0.49646	0.00399	124.52	0.000	1.00

Table S17: Coefficients of effects causing variability in electronic conductivity of BCCFY series at 600 ^{o}C.

Term	Effect	Coef	SE Coef	T-Value	P-Value	VIF
Constant		2.19344	0.00632	347.04	0.000	
Co	1.84944	0.92472	0.00632	146.31	0.000	1.00
Ce	-0.84301	-0.42150	0.00632	-66.69	0.000	1.00
Fe	-0.58155	-0.29078	0.00632	-46.01	0.000	1.00
Y	-1.44226	-0.72113	0.00632	-114.10	0.000	1.00
Co*Ce	0.08512	0.04256	0.00632	6.73	0.000	1.00
Co*Fe	-0.50076	-0.25038	0.00632	-39.61	0.000	1.00
Co*Y	-0.60658	-0.30329	0.00632	-47.99	0.000	1.00
Ce*Fe	-0.22924	-0.11462	0.00632	-18.13	0.000	1.00
Ce*Y	-0.07667	-0.03833	0.00632	-6.07	0.000	1.00
Fe*Y	0.52340	0.26170	0.00632	41.41	0.000	1.00
Co*Ce*Fe	-0.44231	-0.22115	0.00632	-34.99	0.000	1.00
Co*Ce*Y	-0.28295	-0.14147	0.00632	-22.38	0.000	1.00
Co*Fe*Y	0.22111	0.11056	0.00632	17.49	0.000	1.00
Ce*Fe*Y	0.38643	0.19321	0.00632	30.57	0.000	1.00
Co*Ce*Fe*Y	0.95190	0.47595	0.00632	75.30	0.000	1.00

Table S18: Coefficients of effects causing variability in electronic conductivity of BCCFY series at 550 ^{o}C.

Term	Effect	Coef	SE Coef	T-Value	P-Value	VIF
Constant		1.9838	0.0133	149.16	0.000	
Co	1.6939	0.8469	0.0133	63.68	0.000	1.00
Ce	-0.7550	-0.3775	0.0133	-28.38	0.000	1.00
Fe	-0.4851	-0.2426	0.0133	-18.24	0.000	1.00
Y	-1.3557	-0.6779	0.0133	-50.97	0.000	1.00
Co*Ce	0.0822	0.0411	0.0133	3.09	0.007	1.00
Co*Fe	-0.4515	-0.2258	0.0133	-16.98	0.000	1.00
Co*Y	-0.5774	-0.2887	0.0133	-21.71	0.000	1.00
Ce*Fe	-0.2596	-0.1298	0.0133	-9.76	0.000	1.00
Ce*Y	-0.0672	-0.0336	0.0133	-2.53	0.022	1.00
Fe*Y	0.4569	0.2285	0.0133	17.18	0.000	1.00
Co*Ce*Fe	-0.4235	-0.2117	0.0133	-15.92	0.000	1.00
Co*Ce*Y	-0.2487	-0.1244	0.0133	-9.35	0.000	1.00
Co*Fe*Y	0.2133	0.1067	0.0133	8.02	0.000	1.00
Ce*Fe*Y	0.3967	0.1983	0.0133	14.91	0.000	1.00
Co*Ce*Fe*Y	0.8774	0.4387	0.0133	32.99	0.000	1.00

Table S19: Coefficients of effects causing variability in electronic conductivity of BCCFY series at 500 ^{o}C.

Term	Effect	Coef	SE Coef	T-Value	P-Value	VIF
Constant		1.80505	0.00442	408.19	0.000	
Co	1.58131	0.79065	0.00442	178.80	0.000	1.00
Ce	-0.62634	-0.31317	0.00442	-70.82	0.000	1.00
Fe	-0.47404	-0.23702	0.00442	-53.60	0.000	1.00
Y	-1.29224	-0.64612	0.00442	-146.11	0.000	1.00
Co*Ce	0.13283	0.06641	0.00442	15.02	0.000	1.00
Co*Fe	-0.45924	-0.22962	0.00442	-51.93	0.000	1.00
Co*Y	-0.56577	-0.28289	0.00442	-63.97	0.000	1.00
Ce*Fe	-0.29987	-0.14994	0.00442	-33.91	0.000	1.00
Ce*Y	-0.11291	-0.05645	0.00442	-12.77	0.000	1.00
Fe*Y	0.46274	0.23137	0.00442	52.32	0.000	1.00
Co*Ce*Fe	-0.44135	-0.22067	0.00442	-49.90	0.000	1.00
Co*Ce*Y	-0.26775	-0.13387	0.00442	-30.27	0.000	1.00
Co*Fe*Y	0.24853	0.12426	0.00442	28.10	0.000	1.00
Ce*Fe*Y	0.41326	0.20663	0.00442	46.73	0.000	1.00
Co*Ce*Fe*Y	0.83623	0.41812	0.00442	94.55	0.000	1.00

Table S20: Coefficients of effects causing variability in electronic conductivity of BSCF series at 650 ^{o}C.

Term	Effect	Coef	SE Coef	T-Value	P-Value	VIF
Constant		0.055763	0.000541	103.00	0.000	
Ba	0.015869	0.007935	0.000541	14.66	0.000	1.00
Sr	0.014794	0.007397	0.000541	13.66	0.000	1.00
Co	0.014106	0.007053	0.000541	13.03	0.000	1.00
Fe	0.014269	0.007135	0.000541	13.18	0.000	1.00
Ba*Sr	-0.006226	-0.003113	0.000541	-5.75	0.000	1.00
Ba*Co	-0.008964	-0.004482	0.000541	-8.28	0.000	1.00
Ba*Fe	-0.019964	-0.009982	0.000541	-18.44	0.000	1.00
Sr*Co	-0.003733	-0.001867	0.000541	-3.45	0.003	1.00
Sr*Fe	-0.000054	-0.000027	0.000541	-0.05	0.961	1.00
Co*Fe	0.024577	0.012288	0.000541	22.70	0.000	1.00
Ba*Sr*Co	-0.023885	-0.011942	0.000541	-22.06	0.000	1.00
Ba*Sr*Fe	-0.011551	-0.005776	0.000541	-10.67	0.000	1.00
Ba*Co*Fe	0.006914	0.003457	0.000541	6.39	0.000	1.00
Sr*Co*Fe	0.001708	0.000854	0.000541	1.58	0.134	1.00
Ba*Sr*Co*Fe	-0.029161	-0.014580	0.000541	-26.93	0.000	1.00

Table S21: Coefficients of effects causing variability in electronic conductivity of BSCF series at 600 ^{o}C.

Term	Effect	Coef	SE Coef	T-Value	P-Value	VIF
Constant		0.137652	0.000289	476.56	0.000	
Ba	0.018691	0.009345	0.000289	32.35	0.000	1.00
Sr	0.019291	0.009645	0.000289	33.39	0.000	1.00
Co	0.042414	0.021207	0.000289	73.42	0.000	1.00
Fe	0.046766	0.023383	0.000289	80.95	0.000	1.00
Ba*Sr	-0.027865	-0.013932	0.000289	-48.23	0.000	1.00
Ba*Co	-0.019425	-0.009712	0.000289	-33.63	0.000	1.00
Ba*Fe	-0.041382	-0.020691	0.000289	-71.63	0.000	1.00
Sr*Co	-0.024001	-0.012000	0.000289	-41.55	0.000	1.00
Sr*Fe	0.006413	0.003207	0.000289	11.10	0.000	1.00
Co*Fe	0.053036	0.026518	0.000289	91.81	0.000	1.00
Ba*Sr*Co	-0.057072	-0.028536	0.000289	-98.79	0.000	1.00
Ba*Sr*Fe	-0.034496	-0.017248	0.000289	-59.71	0.000	1.00
Ba*Co*Fe	0.021006	0.010503	0.000289	36.36	0.000	1.00
Sr*Co*Fe	0.005896	0.002948	0.000289	10.21	0.000	1.00
Ba*Sr*Co*Fe	-0.069244	-0.034622	0.000289	-119.86	0.000	1.00

Table S22: Coefficients of effects causing variability in electronic conductivity of BSCF series at 550 ^{o}C.

Term	Effect	Coef	SE Coef	T-Value	P-Value	VIF
Constant		0.350519	0.000796	440.45	0.000	
Ba	0.031315	0.015658	0.000796	19.68	0.000	1.00
Sr	0.050075	0.025038	0.000796	31.46	0.000	1.00
Co	0.138498	0.069249	0.000796	87.02	0.000	1.00
Fe	0.107243	0.053622	0.000796	67.38	0.000	1.00
Ba*Sr	-0.089092	-0.044546	0.000796	-55.98	0.000	1.00
Ba*Co	-0.074215	-0.037108	0.000796	-46.63	0.000	1.00
Ba*Fe	-0.108982	-0.054491	0.000796	-68.47	0.000	1.00
Sr*Co	-0.036999	-0.018499	0.000796	-23.25	0.000	1.00
Sr*Fe	0.046437	0.023218	0.000796	29.18	0.000	1.00
Co*Fe	0.137471	0.068736	0.000796	86.37	0.000	1.00
Ba*Sr*Co	-0.144754	-0.072377	0.000796	-90.95	0.000	1.00
Ba*Sr*Fe	-0.095803	-0.047901	0.000796	-60.19	0.000	1.00
Ba*Co*Fe	0.020115	0.010058	0.000796	12.64	0.000	1.00
Sr*Co*Fe	0.032779	0.016389	0.000796	20.59	0.000	1.00
Ba*Sr*Co*Fe	-0.178572	-0.089286	0.000796	-112.19	0.000	1.00

Table S23: Coefficients of effects causing variability in electronic conductivity of BSCF series at 500 ^{o}C.

Term	Effect	Coef	SE Coef	T-Value	P-Value	VIF
Constant		1.10074	0.00250	439.99	0.000	
Ba	-0.02578	-0.01289	0.00250	-5.15	0.000	1.00
Sr	0.12931	0.06465	0.00250	25.84	0.000	1.00
Co	0.47180	0.23590	0.00250	94.29	0.000	1.00
Fe	0.27217	0.13608	0.00250	54.40	0.000	1.00
Ba*Sr	-0.31359	-0.15679	0.00250	-62.67	0.000	1.00
Ba*Co	-0.27205	-0.13602	0.00250	-54.37	0.000	1.00
Ba*Fe	-0.40209	-0.20104	0.00250	-80.36	0.000	1.00
Sr*Co	-0.02208	-0.01104	0.00250	-4.41	0.000	1.00
Sr*Fe	0.22498	0.11249	0.00250	44.96	0.000	1.00
Co*Fe	0.36520	0.18260	0.00250	72.99	0.000	1.00
Ba*Sr*Co	-0.42091	-0.21045	0.00250	-84.12	0.000	1.00
Ba*Sr*Fe	-0.29708	-0.14854	0.00250	-59.37	0.000	1.00
Ba*Co*Fe	-0.03506	-0.01753	0.00250	-7.01	0.000	1.00
Sr*Co*Fe	0.16474	0.08237	0.00250	32.92	0.000	1.00
Ba*Sr*Co*Fe	-0.57860	-0.28930	0.00250	-115.64	0.000	1.00

Table S24: Coefficients of effects causing variability in D_{chem} at 650 ^{o}C.

Term	Effect	Coef	SE Coef	T-Value	P-Value	VIF
Constant		0.000070	*	*	*	
Co	0.000004	0.000002	*	*	*	1.00
Ce	-0.000038	-0.000019	*	*	*	1.00
Fe	-0.000012	-0.000006	*	*	*	1.00
Y	-0.000017	-0.000009	*	*	*	1.00
Co*Ce	0.000006	0.000003	*	*	*	1.00
Co*Fe	-0.000007	-0.000004	*	*	*	1.00
Co*Y	0.000039	0.000019	*	*	*	1.00

Table S25: Coefficients of effects causing variability in D_{chem} at 600 ^{o}C.

Term	**Effect**	**Coef**	**SE Coef**	**T-Value**	**P-Value**	**VIF**
Constant		0.000037	*	*	*	
Co	0.000002	0.000001	*	*	*	1.00
Ce	-0.000017	-0.000009	*	*	*	1.00
Fe	-0.000007	-0.000004	*	*	*	1.00
Y	-0.000009	-0.000005	*	*	*	1.00
Co*Ce	0.000008	0.000004	*	*	*	1.00
Co*Fe	-0.000004	-0.000002	*	*	*	1.00
Co*Y	0.000015	0.000007	*	*	*	1.00

Table S26: Coefficients of effects causing variability in D_{chem} at 550 °C.

Term	Effect	Coef	SE Coef	T-Value	P-Value	VIF
Constant		0.000020	*	*	*	
Co	0.000000	0.000000	*	*	*	1.00
Ce	-0.000006	-0.000003	*	*	*	1.00
Fe	-0.000006	-0.000003	*	*	*	1.00
Y	-0.000008	-0.000004	*	*	*	1.00
Co*Ce	0.000008	0.000004	*	*	*	1.00
Co*Fe	-0.000004	-0.000002	*	*	*	1.00
Co*Y	0.000005	0.000002	*	*	*	1.00

Table S27: Coefficients of effects causing variability in D_{chem} at 500 °C.

Term	Effect	Coef	SE Coef	T-Value	P-Value	VIF
Constant		0.000010	*	*	*	
Co	0.000001	0.000001	*	*	*	1.00
Ce	0.000001	0.000001	*	*	*	1.00
Fe	-0.000005	-0.000002	*	*	*	1.00
Y	-0.000005	-0.000003	*	*	*	1.00
Co*Ce	0.000005	0.000003	*	*	*	1.00
Co*Fe	-0.000004	-0.000002	*	*	*	1.00
Co*Y	-0.000001	-0.000000	*	*	*	1.00

Table S28: Coefficients of effects causing variability in k_{chem} at 650 °C.

Term	Effect	Coef	SE Coef	T-Value	P-Value	VIF
Constant		0.000704	*	*	*	
Co	0.000025	0.000013	*	*	*	1.00
Ce	-0.000346	-0.000173	*	*	*	1.00
Fe	-0.000113	-0.000057	*	*	*	1.00
Y	-0.000181	-0.000090	*	*	*	1.00
Co*Ce	0.000066	0.000033	*	*	*	1.00
Co*Fe	-0.000119	-0.000059	*	*	*	1.00
Co*Y	0.000390	0.000195	*	*	*	1.00

Table S29: Coefficients of effects causing variability in k_{chem} at 600 °C.

Term	**Effect**	**Coef**	**SE Coef**	**T-Value**	**P-Value**	**VIF**
Constant		0.000378	*	*	*	
Co	0.000015	0.000007	*	*	*	1.00
Ce	-0.000161	-0.000080	*	*	*	1.00
Fe	-0.000072	-0.000036	*	*	*	1.00
Y	-0.000088	-0.000044	*	*	*	1.00
Co*Ce	0.000086	0.000043	*	*	*	1.00
Co*Fe	-0.000073	-0.000036	*	*	*	1.00
Co*Y	0.000151	0.000075	*	*	*	1.00

Table S30: Coefficients of effects causing variability in k_{chem} at 550 ^{o}C.

Term	Effect	Coef	SE Coef	T-Value	P-Value	VIF
Constant		0.000198	*	*	*	
Co	0.000009	0.000004	*	*	*	1.00
Ce	-0.000055	-0.000027	*	*	*	1.00
Fe	-0.000061	-0.000030	*	*	*	1.00
Y	-0.000075	-0.000038	*	*	*	1.00
Co*Ce	0.000080	0.000040	*	*	*	1.00
Co*Fe	-0.000052	-0.000026	*	*	*	1.00
Co*Y	0.000047	0.000023	*	*	*	1.00

Table S31: Coefficients of effects causing variability in k_{chem} at 500 ^{o}C.

Term	Effect	Coef	SE Coef	T-Value	P-Value	VIF
Constant		0.000102	*	*	*	
Co	0.000016	0.000008	*	*	*	1.00
Ce	0.000012	0.000006	*	*	*	1.00
Fe	-0.000047	-0.000023	*	*	*	1.00
Y	-0.000054	-0.000027	*	*	*	1.00
Co*Ce	0.000059	0.000029	*	*	*	1.00
Co*Fe	-0.000041	-0.000021	*	*	*	1.00
Co*Y	-0.000012	-0.000006	*	*	*	1.00

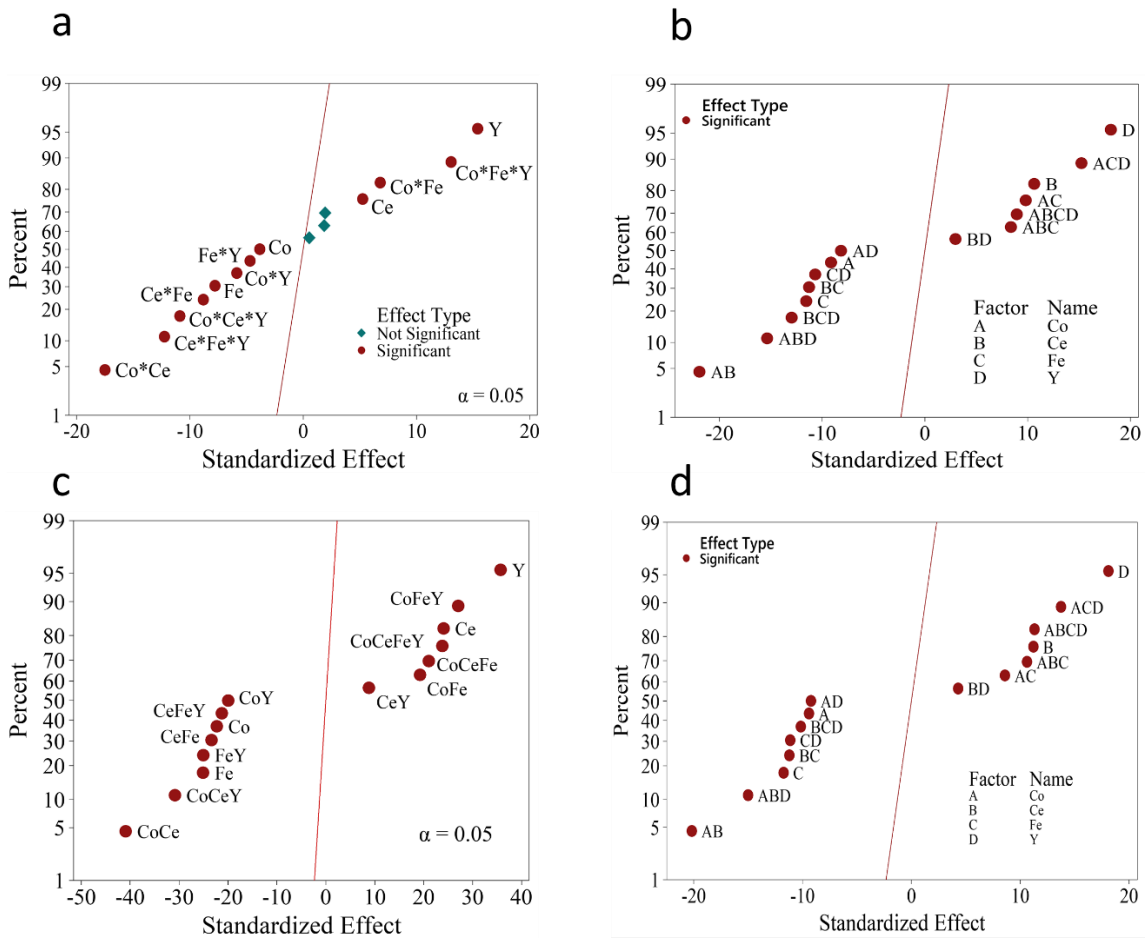

Figure S8: Normal plot of standardized effects of ASR with a significant effect of 0.05 at (a) 650 ºC (b) 600 ºC (c) 550 ºC and (d) 500 ºC. A= Co, B = Ce, C = Fe, D = Y.

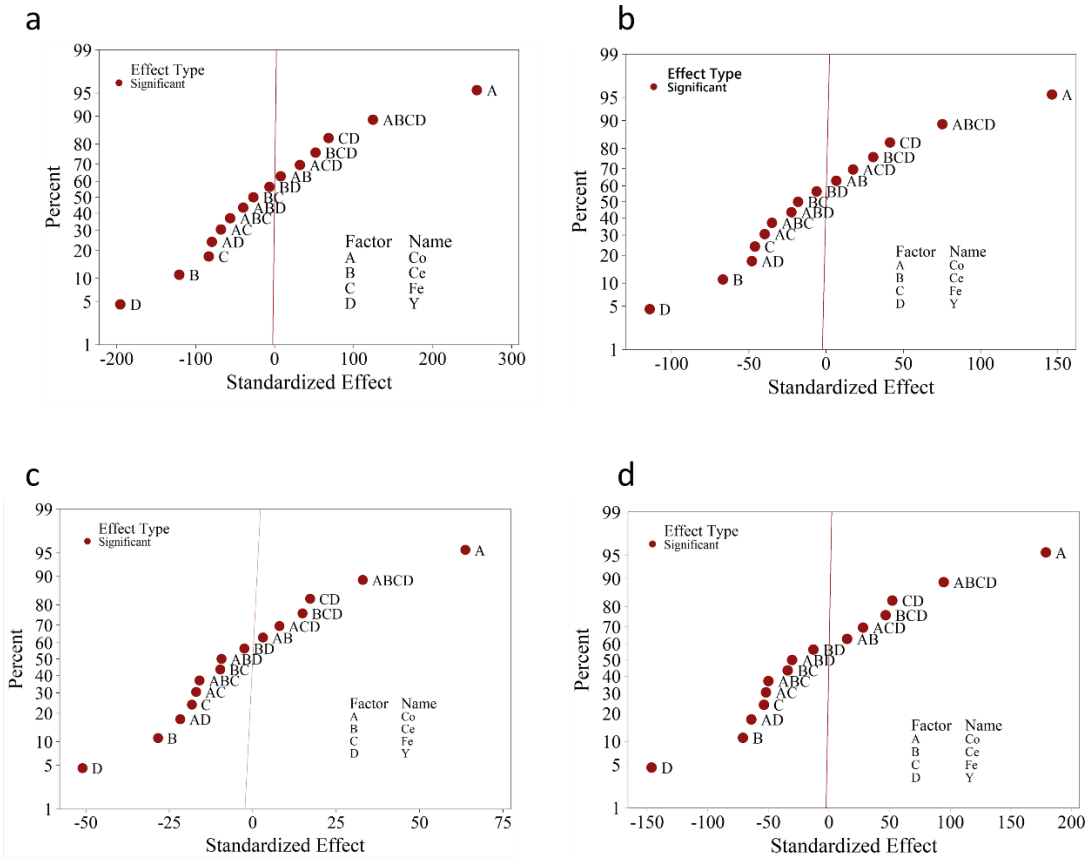

Figure S9: Normal plot of standardized effects of EC with a significance level of 0.05 at (a) 650 ºC (a) 600 ºC (b) 550 ºC and (c) 500 ºC. A= Co, B = Ce, C = Fe, D = Y.

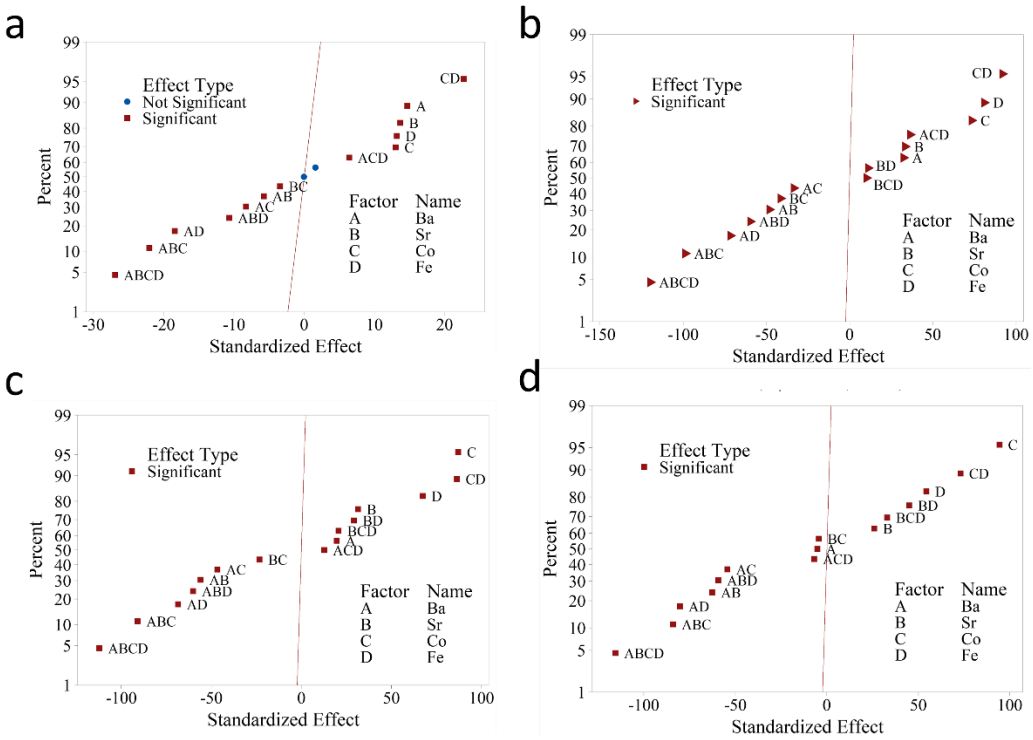

Figure S10: Normal plot of standardized effects of ASR with a significance level of 0.05 for BSCF at (a) 650 ºC (a) 600 ºC (b) 550 ºC and (c) 500 ºC. A= Ba, B = Sr, C = Co, D = Fe.

Table S32: Analysis of variance (ANOVA) of BCCFY series for ASR at 650 ºC.

Source	DF	Adj SS	Adj MS	F-Value	P-Value
Model	15	0.429123	0.028608	84.81	0.000
Linear	4	0.114754	0.028688	85.05	0.000
Co	1	0.004948	0.004948	14.67	0.001
Ce	1	0.009311	0.009311	27.60	0.000
Fe	1	0.020422	0.020422	60.54	0.000
Y	1	0.080073	0.080073	237.37	0.000
2-Way Interactions	6	0.164028	0.027338	81.04	0.000
Co*Ce	1	0.103239	0.103239	306.05	0.000
Co*Fe	1	0.015617	0.015617	46.30	0.000
Co*Y	1	0.011581	0.011581	34.33	0.000
Ce*Fe	1	0.026105	0.026105	77.39	0.000
Ce*Y	1	0.000097	0.000097	0.29	0.598
Fe*Y	1	0.007389	0.007389	21.90	0.000
3-Way Interactions	4	0.149074	0.037269	110.48	0.000
Co*Ce*Fe	1	0.001176	0.001176	3.49	0.080
Co*Ce*Y	1	0.039931	0.039931	118.37	0.000
Co*Fe*Y	1	0.057511	0.057511	170.49	0.000
Ce*Fe*Y	1	0.050457	0.050457	149.58	0.000
4-Way Interactions	1	0.001267	0.001267	3.76	0.071
Co*Ce*Fe*Y	1	0.001267	0.001267	3.76	0.071
Error	16	0.005397	0.000337		
Total	31	0.434520			

Table S33: Analysis of variance (ANOVA) of BCCFY series for ASR at 600 ºC.

Source	DF	Adj SS	Adj MS	F-Value	P-Value
Model	15	3.11443	0.207629	155.87	0.000
Linear	4	0.87619	0.219048	164.44	0.000
Co	1	0.11097	0.110967	83.30	0.000
Ce	1	0.15103	0.151027	113.38	0.000
Fe	1	0.17788	0.177878	133.54	0.000
Y	1	0.43632	0.436319	327.55	0.000
2-Way Interactions	6	1.19150	0.198584	149.08	0.000
Co*Ce	1	0.64107	0.641075	481.27	0.000
Co*Fe	1	0.12870	0.128697	96.62	0.000
Co*Y	1	0.08855	0.088549	66.48	0.000
Ce*Fe	1	0.16937	0.169368	127.15	0.000
Ce*Y	1	0.01177	0.011772	8.84	0.009
Fe*Y	1	0.15204	0.152043	114.14	0.000
3-Way Interactions	4	0.93992	0.234980	176.40	0.000
Co*Ce*Fe	1	0.09355	0.093552	70.23	0.000
Co*Ce*Y	1	0.31336	0.313364	235.25	0.000
Co*Fe*Y	1	0.30900	0.309004	231.97	0.000
Ce*Fe*Y	1	0.22400	0.224002	168.16	0.000
4-Way Interactions	1	0.10681	0.106813	80.19	0.000
Co*Ce*Fe*Y	1	0.10681	0.106813	80.19	0.000
Error	16	0.02131	0.001332		
Total	31	3.13574			

Table S34: Analysis of variance (ANOVA) of BCCFY series for ASR at 550 ºC.

Source	DF	Adj SS	Adj MS	F-Value	P-Value
Model	15	22.4980	1.49987	654.39	0.000
Linear	4	6.8344	1.70860	745.46	0.000
Co	1	1.1373	1.13727	496.19	0.000
Ce	1	1.3288	1.32876	579.73	0.000
Fe	1	1.4407	1.44070	628.57	0.000
Y	1	2.9277	2.92769	1277.34	0.000
2-Way Interactions	6	8.4601	1.41002	615.19	0.000
Co*Ce	1	3.8356	3.83565	1673.48	0.000
Co*Fe	1	0.8497	0.84966	370.70	0.000
Co*Y	1	0.9114	0.91144	397.66	0.000
Ce*Fe	1	1.2485	1.24846	544.70	0.000
Ce*Y	1	0.1788	0.17876	77.99	0.000
Fe*Y	1	1.4362	1.43616	626.59	0.000
3-Way Interactions	4	5.9071	1.47677	644.31	0.000
Co*Ce*Fe	1	1.0140	1.01405	442.43	0.000
Co*Ce*Y	1	2.1795	2.17952	950.92	0.000
Co*Fe*Y	1	1.6780	1.67795	732.09	0.000
Ce*Fe*Y	1	1.0356	1.03556	451.81	0.000
4-Way Interactions	1	1.2964	1.29640	565.61	0.000
Co*Ce*Fe*Y	1	1.2964	1.29640	565.61	0.000
Error	16	0.0367	0.00229		
Total	31	22.5347			

Table S35: Analysis of variance (ANOVA) of BCCFY series for ASR at 500 ºC.

Source	DF	Adj SS	Adj MS	F-Value	P-Value
Model	15	154.198	10.2799	151.35	0.000
Linear	4	46.125	11.5313	169.78	0.000
Co	1	6.015	6.0155	88.57	0.000
Ce	1	8.519	8.5190	125.43	0.000
Fe	1	9.356	9.3563	137.75	0.000
Y	1	22.234	22.2343	327.36	0.000
2-Way Interactions	6	56.619	9.4365	138.94	0.000
Co*Ce	1	27.642	27.6421	406.98	0.000
Co*Fe	1	5.015	5.0154	73.84	0.000
Co*Y	1	5.786	5.7856	85.18	0.000
Ce*Fe	1	8.522	8.5223	125.48	0.000
Ce*Y	1	1.255	1.2553	18.48	0.001
Fe*Y	1	8.398	8.3984	123.65	0.000
3-Way Interactions	4	42.782	10.6954	157.47	0.000
Co*Ce*Fe	1	7.650	7.6498	112.63	0.000
Co*Ce*Y	1	15.299	15.2985	225.24	0.000
Co*Fe*Y	1	12.827	12.8274	188.86	0.000
Ce*Fe*Y	1	7.006	7.0060	103.15	0.000
4-Way Interactions	1	8.672	8.6724	127.69	0.000
Co*Ce*Fe*Y	1	8.672	8.6724	127.69	0.000
Error	16	1.087	0.0679		
Total	31	155.285			

Table S36: Analysis of variance (ANOVA) of BCCFY series for EC at 650 ºC.

Source	DF	Adj SS	Adj MS	F-Value	P-Value
Model	15	84.0787	5.6052	11019.93	0.000
Linear	4	63.5849	15.8962	31252.06	0.000
Co	1	33.3314	33.3314	65529.67	0.000
Ce	1	7.3975	7.3975	14543.53	0.000
Fe	1	3.5140	3.5140	6908.46	0.000
Y	1	19.3421	19.3421	38026.58	0.000
2-Way Interactions	6	8.3216	1.3869	2726.71	0.000
Co*Ce	1	0.0299	0.0299	58.74	0.000
Co*Fe	1	2.3380	2.3380	4596.43	0.000
Co*Y	1	3.1889	3.1889	6269.34	0.000
Ce*Fe	1	0.3680	0.3680	723.51	0.000
Ce*Y	1	0.0219	0.0219	43.13	0.000
Fe*Y	1	2.3749	2.3749	4669.11	0.000
3-Way Interactions	4	4.2849	1.0712	2106.05	0.000
Co*Ce*Fe	1	1.6048	1.6048	3155.08	0.000
Co*Ce*Y	1	0.7988	0.7988	1570.37	0.000
Co*Fe*Y	1	0.5204	0.5204	1023.10	0.000
Ce*Fe*Y	1	1.3610	1.3610	2675.64	0.000
4-Way Interactions	1	7.8872	7.8872	15506.33	0.000
Co*Ce*Fe*Y	1	7.8872	7.8872	15506.33	0.000
Error	16	0.0081	0.0005		
Total	31	84.0868			

Table S37: Analysis of variance (ANOVA) of BCCFY series for EC at 600 ºC.

Source	DF	Adj SS	Adj MS	F-Value	P-Value
Model	15	71.1020	4.7401	3708.10	0.000
Linear	4	52.3953	13.0988	10246.92	0.000
Co	1	27.3635	27.3635	21405.90	0.000
Ce	1	5.6853	5.6853	4447.47	0.000
Fe	1	2.7056	2.7056	2116.55	0.000
Y	1	16.6408	16.6408	13017.77	0.000
2-Way Interactions	6	7.6665	1.2777	999.55	0.000
Co*Ce	1	0.0580	0.0580	45.34	0.000
Co*Fe	1	2.0060	2.0060	1569.29	0.000
Co*Y	1	2.9435	2.9435	2302.61	0.000
Ce*Fe	1	0.4204	0.4204	328.86	0.000
Ce*Y	1	0.0470	0.0470	36.79	0.000
Fe*Y	1	2.1916	2.1916	1714.42	0.000
3-Way Interactions	4	3.7913	0.9478	741.46	0.000
Co*Ce*Fe	1	1.5651	1.5651	1224.32	0.000
Co*Ce*Y	1	0.6405	0.6405	501.02	0.000
Co*Fe*Y	1	0.3911	0.3911	305.97	0.000
Ce*Fe*Y	1	1.1946	1.1946	934.51	0.000
4-Way Interactions	1	7.2490	7.2490	5670.72	0.000
Co*Ce*Fe*Y	1	7.2490	7.2490	5670.72	0.000
Error	16	0.0205	0.0013		
Total	31	71.1224			

Table S38: Analysis of variance (ANOVA) of BCCFY series for EC at 550 °C.

Source	DF	Adj SS	Adj MS	F-Value	P-Value
Model	15	60.4095	4.0273	711.50	0.000
Linear	4	44.1002	11.0251	1947.79	0.000
Co	1	22.9533	22.9533	4055.14	0.000
Ce	1	4.5605	4.5605	805.71	0.000
Fe	1	1.8829	1.8829	332.65	0.000
Y	1	14.7035	14.7035	2597.65	0.000
2-Way Interactions	6	6.5980	1.0997	194.28	0.000
Co*Ce	1	0.0540	0.0540	9.55	0.007
Co*Fe	1	1.6311	1.6311	288.16	0.000
Co*Y	1	2.6674	2.6674	471.26	0.000
Ce*Fe	1	0.5390	0.5390	95.23	0.000
Ce*Y	1	0.0361	0.0361	6.38	0.022
Fe*Y	1	1.6703	1.6703	295.09	0.000
3-Way Interactions	4	3.5526	0.8881	156.91	0.000
Co*Ce*Fe	1	1.4346	1.4346	253.45	0.000
Co*Ce*Y	1	0.4950	0.4950	87.44	0.000
Co*Fe*Y	1	0.3641	0.3641	64.32	0.000
Ce*Fe*Y	1	1.2589	1.2589	222.41	0.000
4-Way Interactions	1	6.1587	6.1587	1088.06	0.000
Co*Ce*Fe*Y	1	6.1587	6.1587	1088.06	0.000
Error	16	0.0906	0.0057		
Total	31	60.5001			

Table S39: Analysis of variance (ANOVA) of BCCFY series for EC at 500 ºC.

Source	DF	Adj SS	Adj MS	F-Value	P-Value
Model	15	54.8094	3.6540	5839.37	0.000
Linear	4	38.2994	9.5748	15301.52	0.000
Co	1	20.0043	20.0043	31968.72	0.000
Ce	1	3.1384	3.1384	5015.49	0.000
Fe	1	1.7977	1.7977	2872.88	0.000
Y	1	13.3590	13.3590	21348.98	0.000
2-Way Interactions	6	6.9235	1.1539	1844.08	0.000
Co*Ce	1	0.1411	0.1411	225.57	0.000
Co*Fe	1	1.6872	1.6872	2696.31	0.000
Co*Y	1	2.5608	2.5608	4092.40	0.000
Ce*Fe	1	0.7194	0.7194	1149.64	0.000
Ce*Y	1	0.1020	0.1020	162.97	0.000
Fe*Y	1	1.7130	1.7130	2737.57	0.000
3-Way Interactions	4	3.9922	0.9980	1594.98	0.000
Co*Ce*Fe	1	1.5583	1.5583	2490.31	0.000
Co*Ce*Y	1	0.5735	0.5735	916.52	0.000
Co*Fe*Y	1	0.4941	0.4941	789.68	0.000
Ce*Fe*Y	1	1.3663	1.3663	2183.40	0.000
4-Way Interactions	1	5.5943	5.5943	8940.17	0.000
Co*Ce*Fe*Y	1	5.5943	5.5943	8940.17	0.000
Error	16	0.0100	0.0006		
Total	31	54.8194			

Table S40: Analysis of variance (ANOVA) of BSCF series for ASR at 650 ^{o}C.

Source	DF	Adj SS	Adj MS	F-Value	P-Value
Model	15	0.028911	0.001927	205.49	0.000
Linear	4	0.006986	0.001747	186.21	0.000
Ba	1	0.002015	0.002015	214.79	0.000
Sr	1	0.001751	0.001751	186.68	0.000
Co	1	0.001592	0.001592	169.71	0.000
Fe	1	0.001629	0.001629	173.66	0.000
2-Way Interactions	6	0.009085	0.001514	161.43	0.000
Ba*Sr	1	0.000310	0.000310	33.06	0.000
Ba*Co	1	0.000643	0.000643	68.53	0.000
Ba*Fe	1	0.003189	0.003189	339.94	0.000
Sr*Co	1	0.000111	0.000111	11.89	0.003
Sr*Fe	1	0.000000	0.000000	0.00	0.961
Co*Fe	1	0.004832	0.004832	515.17	0.000
3-Way Interactions	4	0.006037	0.001509	160.91	0.000
Ba*Sr*Co	1	0.004564	0.004564	486.56	0.000
Ba*Sr*Fe	1	0.001067	0.001067	113.81	0.000
Ba*Co*Fe	1	0.000382	0.000382	40.78	0.000
Sr*Co*Fe	1	0.000023	0.000023	2.49	0.134
4-Way Interactions	1	0.006803	0.006803	725.27	0.000
Ba*Sr*Co*Fe	1	0.006803	0.006803	725.27	0.000
Error	16	0.000150	0.000009		
Total	31	0.029061			

Table S41: Analysis of variance (ANOVA) of BSCF series for ASR at 600 ^{o}C.

Source	DF	Adj SS	Adj MS	F-Value	P-Value
Model	15	0.165774	0.011052	4139.49	0.000
Linear	4	0.037660	0.009415	3526.50	0.000
Ba	1	0.002795	0.002795	1046.81	0.000
Sr	1	0.002977	0.002977	1115.10	0.000
Co	1	0.014392	0.014392	5390.51	0.000
Fe	1	0.017497	0.017497	6553.58	0.000
2-Way Interactions	6	0.050369	0.008395	3144.39	0.000
Ba*Sr	1	0.006212	0.006212	2326.58	0.000
Ba*Co	1	0.003019	0.003019	1130.65	0.000
Ba*Fe	1	0.013700	0.013700	5131.33	0.000
Sr*Co	1	0.004608	0.004608	1726.10	0.000
Sr*Fe	1	0.000329	0.000329	123.25	0.000
Co*Fe	1	0.022502	0.022502	8428.43	0.000
3-Way Interactions	4	0.039386	0.009847	3688.13	0.000
Ba*Sr*Co	1	0.026058	0.026058	9760.33	0.000
Ba*Sr*Fe	1	0.009520	0.009520	3565.80	0.000
Ba*Co*Fe	1	0.003530	0.003530	1322.22	0.000
Sr*Co*Fe	1	0.000278	0.000278	104.18	0.000
4-Way Interactions	1	0.038358	0.038358	14367.50	0.000
Ba*Sr*Co*Fe	1	0.038358	0.038358	14367.50	0.000
Error	16	0.000043	0.000003		
Total	31	0.165817			

Table S42: Analysis of variance (ANOVA) of BSCF series for ASR at 550 ºC.

Source	DF	Adj SS	Adj MS	F-Value	P-Value
Model	15	1.16333	0.077555	3826.81	0.000
Linear	4	0.27337	0.068342	3372.20	0.000
Ba	1	0.00785	0.007845	387.11	0.000
Sr	1	0.02006	0.020060	989.84	0.000
Co	1	0.15345	0.153453	7571.86	0.000
Fe	1	0.09201	0.092009	4540.00	0.000
2-Way Interactions	6	0.38197	0.063661	3141.24	0.000
Ba*Sr	1	0.06350	0.063499	3133.23	0.000
Ba*Co	1	0.04406	0.044063	2174.21	0.000
Ba*Fe	1	0.09502	0.095016	4688.39	0.000
Sr*Co	1	0.01095	0.010951	540.37	0.000
Sr*Fe	1	0.01725	0.017251	851.22	0.000
Co*Fe	1	0.15119	0.151187	7460.04	0.000
3-Way Interactions	4	0.25289	0.063222	3119.58	0.000
Ba*Sr*Co	1	0.16763	0.167630	8271.41	0.000
Ba*Sr*Fe	1	0.07343	0.073425	3623.03	0.000
Ba*Co*Fe	1	0.00324	0.003237	159.72	0.000
Sr*Co*Fe	1	0.00860	0.008596	424.14	0.000
4-Way Interactions	1	0.25510	0.255104	12587.62	0.000
Ba*Sr*Co*Fe	1	0.25510	0.255104	12587.62	0.000
Error	16	0.00032	0.000020		
Total	31	1.16365			

Table S43: Analysis of variance (ANOVA) of BSCF series for ASR at 500 ºC.

Source	DF	Adj SS	Adj MS	F-Value	P-Value
Model	15	11.6889	0.77926	3890.93	0.000
Linear	4	2.5125	0.62811	3136.24	0.000
Ba	1	0.0053	0.00532	26.55	0.000
Sr	1	0.1338	0.13377	667.91	0.000
Co	1	1.7808	1.78076	8891.53	0.000
Fe	1	0.5926	0.59261	2958.97	0.000
2-Way Interactions	6	4.1479	0.69132	3451.86	0.000
Ba*Sr	1	0.7867	0.78670	3928.07	0.000
Ba*Co	1	0.5921	0.59207	2956.28	0.000
Ba*Fe	1	1.2934	1.29339	6458.02	0.000
Sr*Co	1	0.0039	0.00390	19.47	0.000
Sr*Fe	1	0.4049	0.40491	2021.78	0.000
Co*Fe	1	1.0670	1.06698	5327.52	0.000
3-Way Interactions	4	2.3503	0.58757	2933.81	0.000
Ba*Sr*Co	1	1.4173	1.41730	7076.74	0.000
Ba*Sr*Fe	1	0.7060	0.70605	3525.36	0.000
Ba*Co*Fe	1	0.0098	0.00983	49.10	0.000
Sr*Co*Fe	1	0.2171	0.21711	1084.04	0.000
4-Way Interactions	1	2.6782	2.67821	13372.61	0.000
Ba*Sr*Co*Fe	1	2.6782	2.67821	13372.61	0.000
Error	16	0.0032	0.00020		
Total	31	11.6921			

Table S44: Model equations for BCCFY that describe the regression relationships between these elemental molar ratio inputs and the response variables.

Model No.	Response		Model Equations
1.	ASR-650	=	-0.383 + 0.01426 Co - 0.03874 Ce + 0.0706 Fe + 0.0396 Y + 0.000389 Co*Ce - 0.002233 Co*Fe - 0.001490 Co*Y + 0.00367 Ce*Fe + 0.00852 Ce*Y - 0.01056 Fe*Y - 0.000023 Co*Ce*Fe - 0.000096 Co*Ce*Y + 0.000340 Co*Fe*Y - 0.000670 Ce*Fe*Y + 0.000004 Co*Ce*Fe*Y
2.	ASR-600	=	0.740 - 0.00414 Co - 0.1603 Ce - 0.0181 Fe - 0.2067 Y + 0.002280 Co*Ce - 0.00087 Co*Fe + 0.00284 Co*Y + 0.01641 Ce*Fe + 0.03383 Ce*Y + 0.01012 Fe*Y - 0.000212 Co*Ce*Fe - 0.000484 Co*Ce*Y + 0.000021 Co*Fe*Y - 0.003152 Ce*Fe*Y + 0.000041 Co*Ce*Fe*Y
3.	ASR-550	=	4.064 - 0.0645 Co - 0.4888 Ce - 0.3311 Fe - 0.8933 Y + 0.007619 Co*Ce + 0.00495 Co*Fe + 0.01562 Co*Y + 0.05076 Ce*Fe + 0.10094 Ce*Y + 0.0765 Fe*Y - 0.000757 Co*Ce*Fe - 0.001537 Co*Ce*Y - 0.001136 Co*Fe*Y - 0.009791 Ce*Fe*Y + 0.000143 Co*Ce*Fe*Y
4.	ASR-500	=	8.77 - 0.1280 Co - 1.249 Ce - 0.611 Fe - 2.218 Y + 0.01939 Co*Ce + 0.00759 Co*Fe + 0.03815 Co*Y + 0.1286 Ce*Fe + 0.2630 Ce*Y + 0.1804 Fe*Y - 0.001907 Co*Ce*Fe - 0.004006 Co*Ce*Y - 0.002502 Co*Fe*Y - 0.02535 Ce*Fe*Y + 0.000370 Co*Ce*Fe*Y
5.	EC-650	=	25.347 - 0.36542 Co - 1.2614 Ce - 3.2061 Fe - 3.2108 Y + 0.025087 Co*Ce + 0.058738 Co*Fe + 0.054597 Co*Y + 0.14817 Ce*Fe + 0.14388 Ce*Y + 0.39921 Fe*Y - 0.003046 Co*Ce*Fe - 0.002929 Co*Ce*Y - 0.007466 Co*Fe*Y - 0.017217 Ce*Fe*Y + 0.000353 Co*Ce*Fe*Y
6.	EC-600	=	24.580 - 0.36284 Co - 1.2050 Ce - 3.1448 Fe - 3.0954 Y + 0.024062 Co*Ce + 0.05777 Co*Fe + 0.05282 Co*Y + 0.14272 Ce*Fe + 0.13697 Ce*Y + 0.39086 Fe*Y - 0.002932 Co*Ce*Fe - 0.002790 Co*Ce*Y - 0.007282 Co*Fe*Y - 0.016554 Ce*Fe*Y + 0.000338 Co*Ce*Fe*Y

7.	EC-550	=	21.895 - 0.3319 Co - 1.0951 Ce - 2.822 Fe - 2.755 Y + 0.022212 Co*Ce + 0.05335 Co*Fe + 0.04779 Co*Y + 0.13006 Ce*Fe + 0.12408 Ce*Y + 0.3500 Fe*Y - 0.002716 Co*Ce*Fe - 0.002561 Co*Ce*Y - 0.006661 Co*Fe*Y - 0.015042 Ce*Fe*Y + 0.000312 Co*Ce*Fe*Y
8.	EC-500	=	20.192 - 0.31391 Co - 1.0517 Ce - 2.5813 Fe - 2.5170 Y + 0.021747 Co*Ce + 0.049492 Co*Fe + 0.044214 Co*Y + 0.12370 Ce*Fe + 0.11770 Ce*Y + 0.31784 Fe*Y - 0.002622 Co*Ce*Fe - 0.002468 Co*Ce*Y - 0.006108 Co*Fe*Y - 0.014149 Ce*Fe*Y + 0.000297 Co*Ce*Fe*Y
9.	D-650	=	0.000332 - 0.000003 Co - 0.000002 Ce + 0.000003 Fe - 0.000032 Y + 0.000000 Co*Ce - 0.000000 Co*Fe + 0.000001 Co*Y
10.	D-600	=	0.000156 - 0.000001 Co - 0.000002 Ce + 0.000002 Fe - 0.000013 Y + 0.000000 Co*Ce - 0.000000 Co*Fe + 0.000000 Co*Y
11.	D-550	=	0.000073 - 0.000001 Co - 0.000001 Ce + 0.000002 Fe - 0.000005 Y + 0.000000 Co*Ce - 0.000000 Co*Fe + 0.000000 Co*Y
12.	D-500	=	0.000013 + 0.000000 Co - 0.000001 Ce + 0.000002 Fe - 0.000000 Y + 0.000000 Co*Ce - 0.000000 Co*Fe - 0.000000 Co*Y
13.	K-650	=	0.003080 - 0.000030 Co - 0.000020 Ce + 0.000065 Fe - 0.000322 Y + 0.000000 Co*Ce - 0.000002 Co*Fe + 0.000005 Co*Y
14.	K-600	=	0.001415 - 0.000012 Co - 0.000016 Ce + 0.000039 Fe - 0.000128 Y + 0.000000 Co*Ce - 0.000001 Co*Fe + 0.000002 Co*Y
15.	K-550	=	0.000644 - 0.000004 Co - 0.000012 Ce + 0.000026 Fe - 0.000049 Y + 0.000000 Co*Ce - 0.000001 Co*Fe + 0.000001 Co*Y
16.	K-500	=	0.000098 + 0.000003 Co - 0.000007 Ce + 0.000021 Fe - 0.000002 Y + 0.000000 Co*Ce - 0.000001 Co*Fe - 0.000000 Co*Y

Table S45: Goodness-of-fit statistics of model equations in **Table S44**.

Model	S	R-sq	R-sq (adj)	R-sq (pred)
1	0.0183665	98.76%	97.59%	95.03%
2	0.0364974	99.32%	98.68%	97.28%
3	0.0478750	99.84%	99.68%	99.35%
4	0.260615	99.30%	98.64%	97.20%
5	0.0225532	99.99%	99.98%	99.96%
6	0.0357536	99.97%	99.94%	99.88%
7	0.0752350	99.85%	99.71%	99.40%
8	0.0250149	99.98%	99.96%	99.93%
9	*	100%	*	*
10	*	100%	*	*
11	*	100%	*	*
12	*	100%	*	*
13	*	100%	*	*
14	*	100%	*	*
15	*	100%	*	*
16	*	100%	*	*

Table S46: Model equations for BSCF that describe the regression relationships between these elemental molar ratio inputs and the response variables.

Model No.	Response		Model Equations
1.	ASR-650	=	-0.4395 + 0.007399 Ba + 0.008467 Sr + 0.006544 Co + 0.02584 Fe - 0.000114 Ba*Sr - 0.000104 Ba*Co - 0.000418 Ba*Fe - 0.000152 Sr*Co - 0.000629 Sr*Fe -0.000406 Co*Fe + 0.000002 Ba*Sr*Co + 0.000010 Ba*Sr*Fe + 0.000007 Ba*Co*Fe + 0.000011 Sr*Co*Fe - 0.000000 Ba*Sr*Co*Fe
2.	ASR-600	=	-1.0678 + 0.017132 Ba + 0.020847 Sr + 0.017173 Co + 0.060574 Fe - 0.000271 Ba*Sr - 0.000254 Ba*Co - 0.000968 Ba*Fe - 0.000382 Sr*Co - 0.001421 Sr*Fe -0.001003 Co*Fe + 0.000005 Ba*Sr*Co + 0.000022 Ba*Sr*Fe + 0.000016 Ba*Co*Fe + 0.000027 Sr*Co*Fe - 0.000000 Ba*Sr*Co*Fe
3.	ASR-550	=	-2.5880 + 0.041859 Ba + 0.05425 Sr + 0.042714 Co + 0.14217 Fe - 0.000726 Ba*Sr - 0.000619 Ba*Co - 0.002269 Ba*Fe - 0.001005 Sr*Co - 0.003635 Sr*Fe - 0.002442 Co*Fe + 0.000014 Ba*Sr*Co + 0.000055 Ba*Sr*Fe + 0.000039 Ba*Co*Fe + 0.000072 Sr*Co*Fe - 0.000001 Ba*Sr*Co*Fe
4.	ASR-500	=	-8.386 + 0.13576 Ba + 0.19538 Sr + 0.13951 Co + 0.44505 Fe - 0.002736 Ba*Sr - 0.001975 Ba*Co - 0.006951 Ba*Fe - 0.003535 Sr*Co - 0.012078 Sr*Fe - 0.007623 Co*Fe + 0.000048 Ba*Sr*Co + 0.000179 Ba*Sr*Fe + 0.000117 Ba*Co*Fe + 0.000238 Sr*Co*Fe - 0.000003 Ba*Sr*Co*Fe

Table S47: Goodness-of-fit statistics of model equations in **Table S46**.

Model	S	R-sq	R-sq (adj)	R-sq (pred)
1	0.0030626	99.48%	99.00%	97.93%
2	0.0016340	99.97%	99.95%	99.90%
3	0.0045018	99.97%	99.95%	99.89%

4	0.0141519	99.97%	99.95%	99.89%

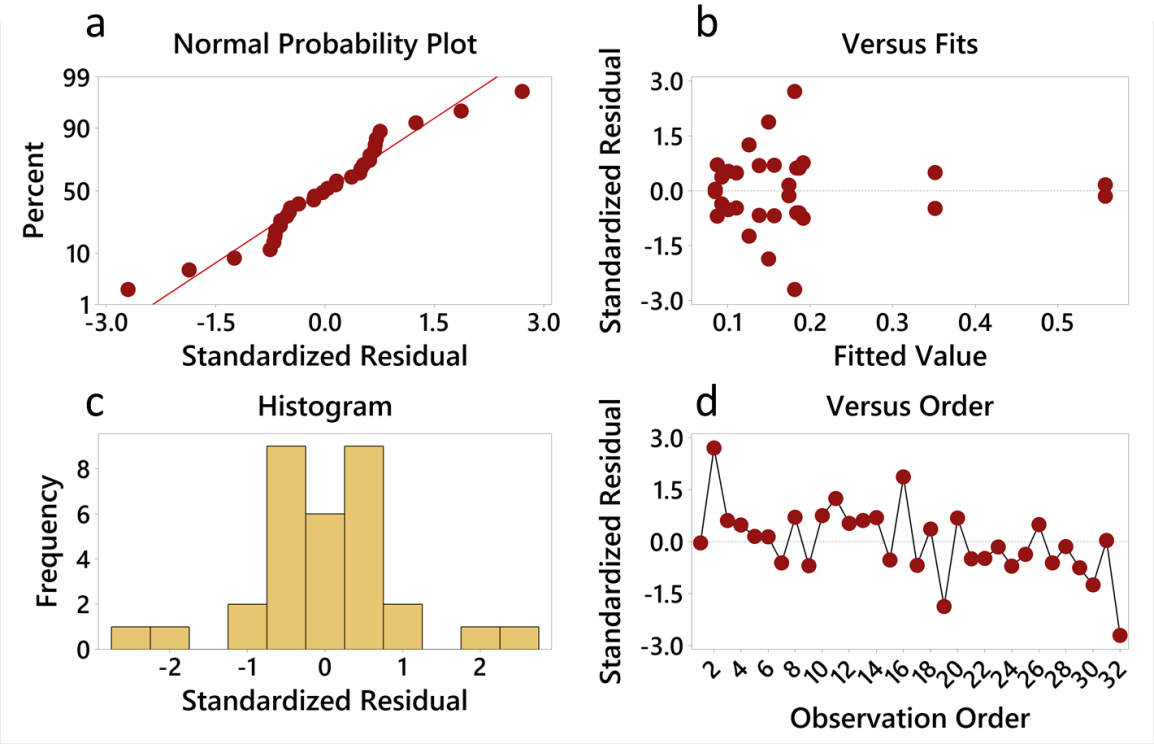

Figure S11: Residual plots of BCCFY series for ASR values at 650 ºC. (a) Normal probability plot (b) Plot of residuals against fitted values (c) Histogram of frequency against residuals, (d) Plot of residuals against observation order.

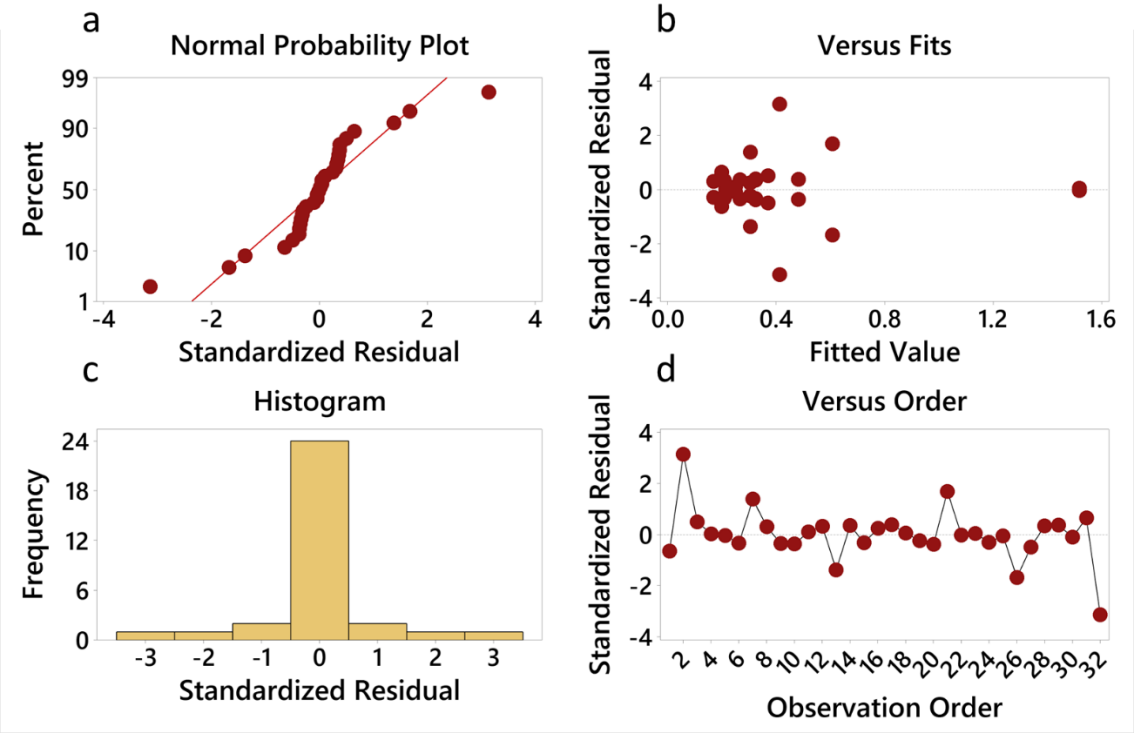

Figure S12: Residual plots of BCCFY series for ASR values at 600 ºC. (a) Normal probability plot (b) Plot of residuals against fitted values (c) Histogram of frequency against residuals, (d) Plot of residuals against observation order.

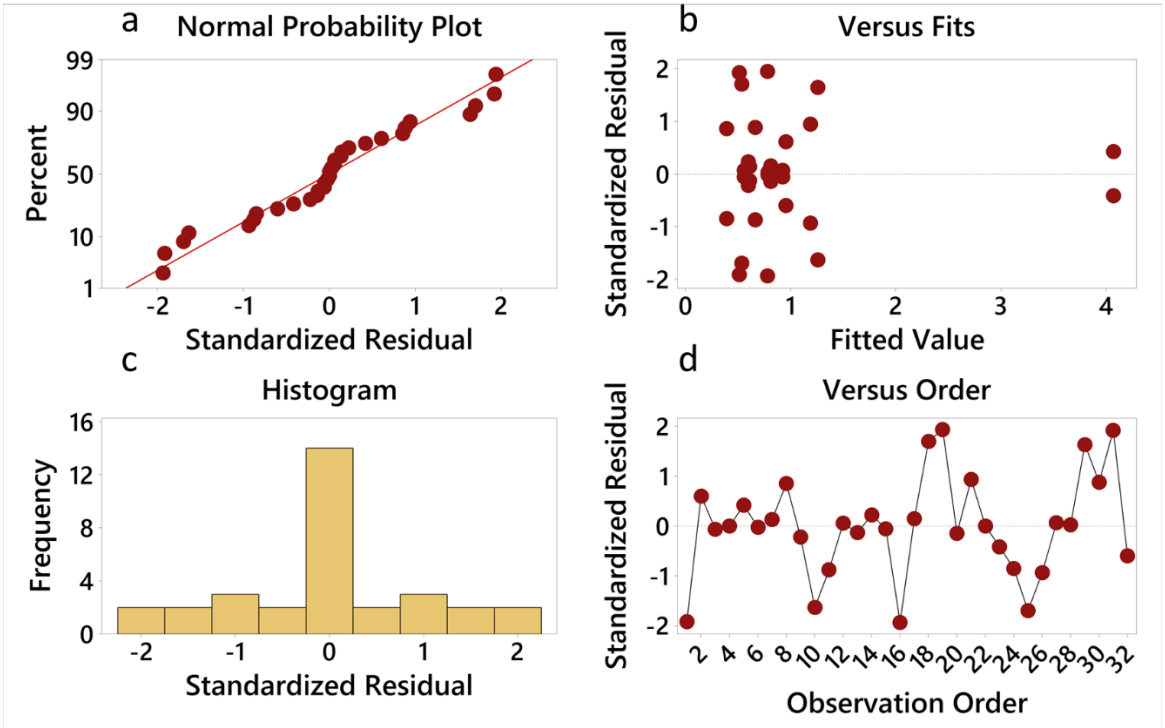

Figure S13: Residual plots of BCCFY series for ASR values at 550 ºC. (a) Normal probability plot (b) Plot of residuals against fitted values (c) Histogram of frequency against residuals, (d) Plot of residuals against observation order.

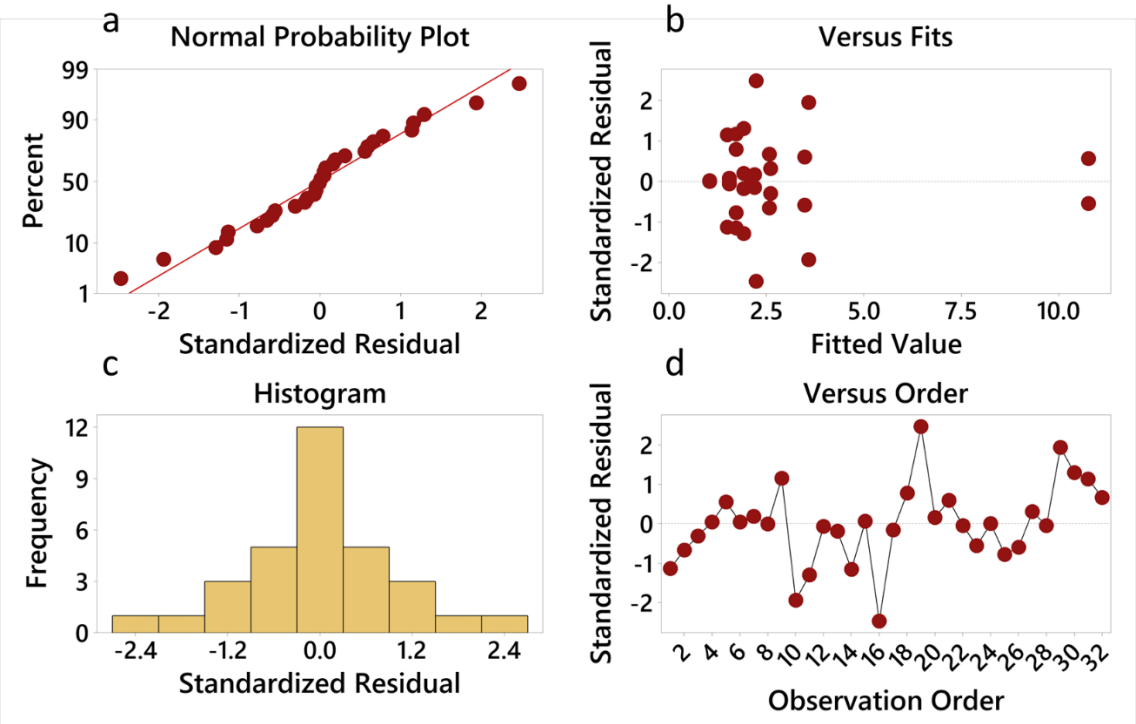

Figure S14: Residual plots of BCCFY series for ASR values at 500 ºC. (a) Normal probability plot (b) Plot of residuals against fitted values (c) Histogram of frequency against residuals, (d) Plot of residuals against observation order.

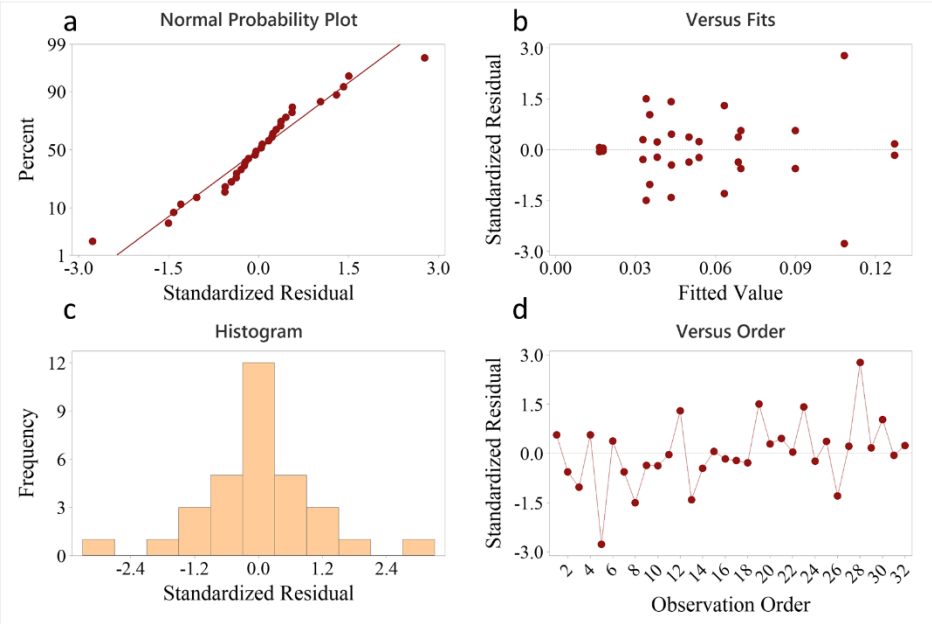

Figure S15: Residual plots of BSCF series for ASR values at 650 ºC. (a) Normal probability plot (b) Plot of residuals against fitted values (c) Histogram of frequency against residuals, (d) Plot of residuals against observation order.

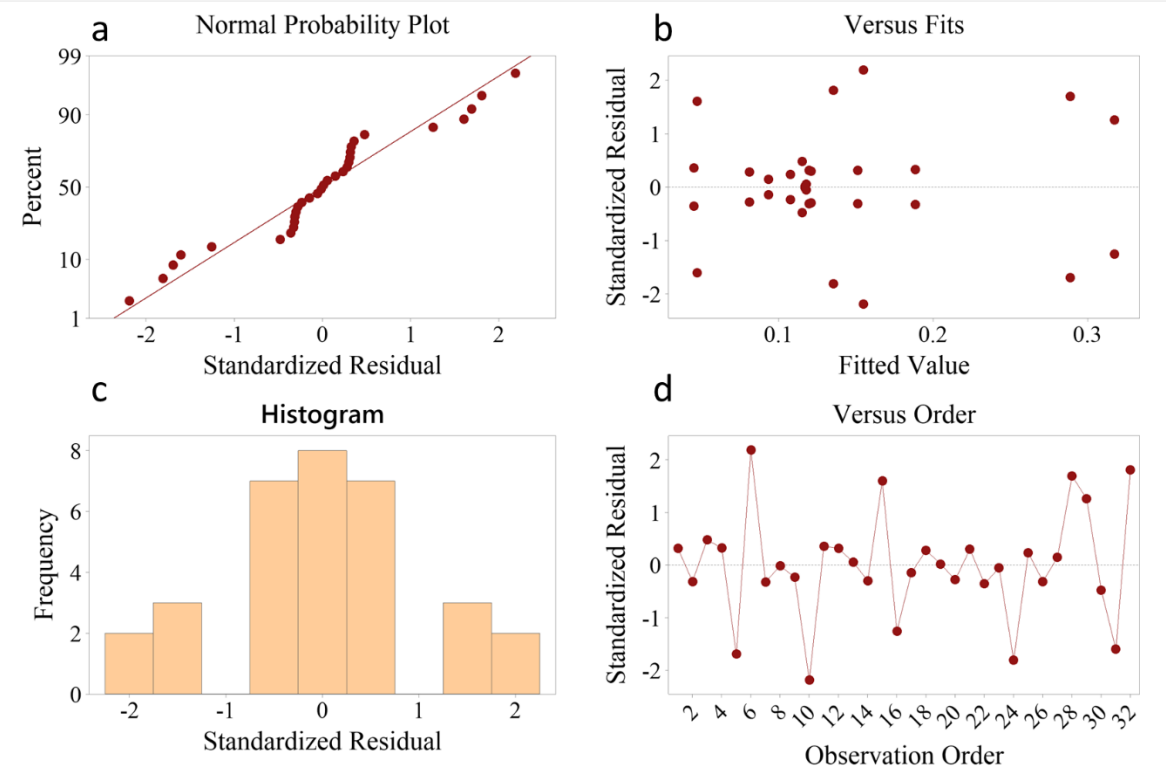

Figure S16: Residual plots of BSCF series for ASR values at 600 ºC. (a) Normal probability plot (b) Plot of residuals against fitted values (c) Histogram of frequency against residuals, (d) Plot of residuals against observation order.

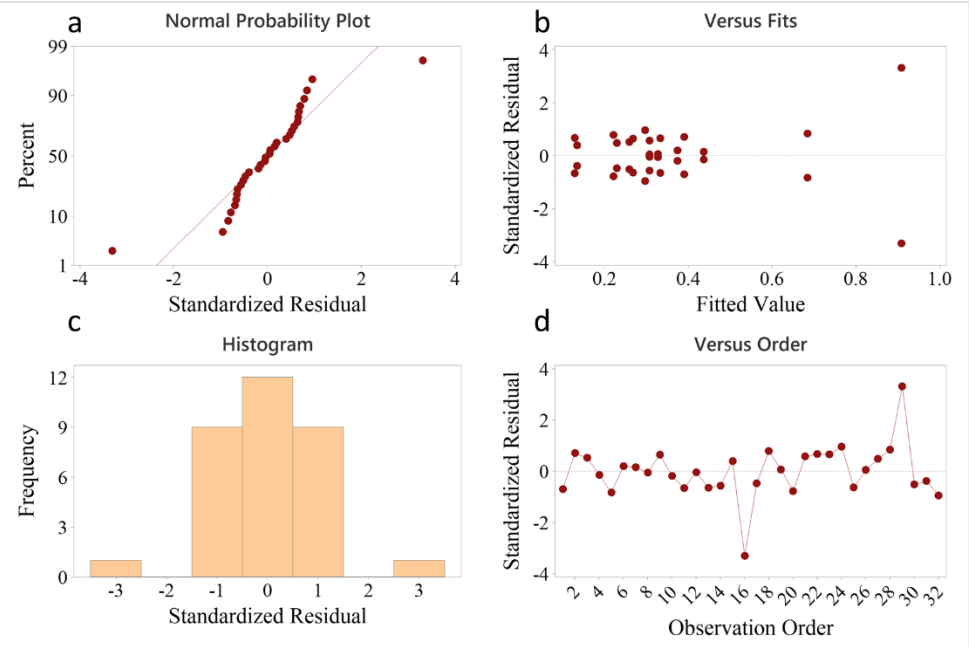

Figure S17: Residual plots of BSCF series for ASR values at 550 ^{o}C. (a) Normal probability plot (b) Plot of residuals against fitted values (c) Histogram of frequency against residuals, (d) Plot of residuals against observation order.

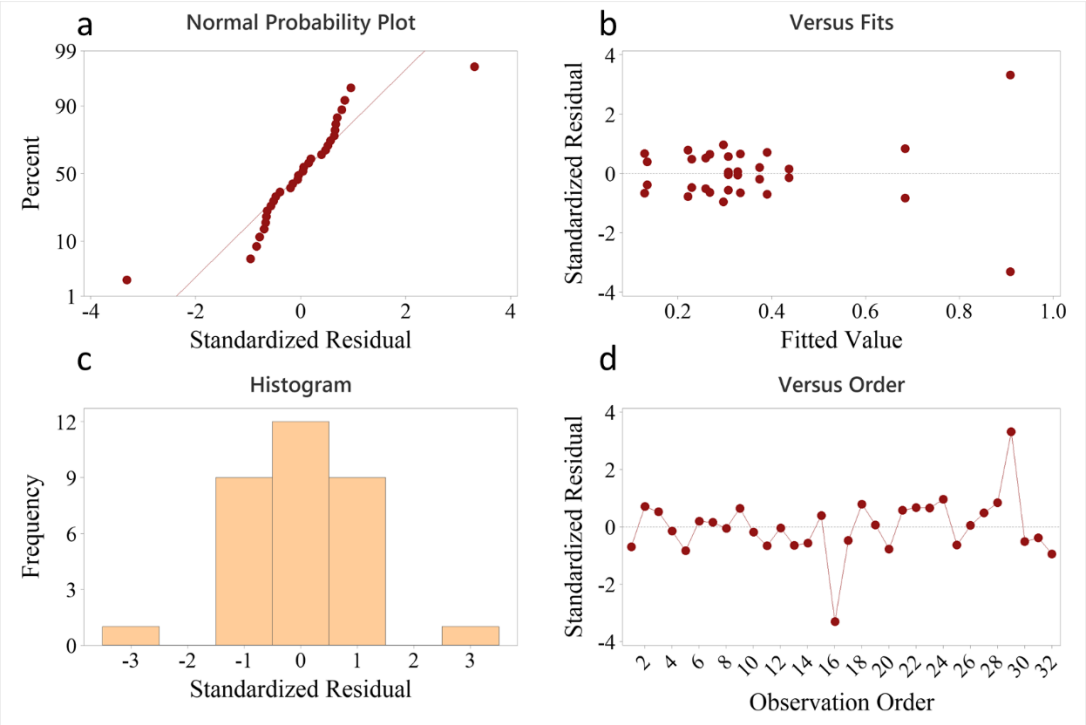

Figure S18: Residual plots of BSCF series for ASR values at 500 ºC. (a) Normal probability plot (b) Plot of residuals against fitted values (c) Histogram of frequency against residuals, (d) Plot of residuals against observation order.

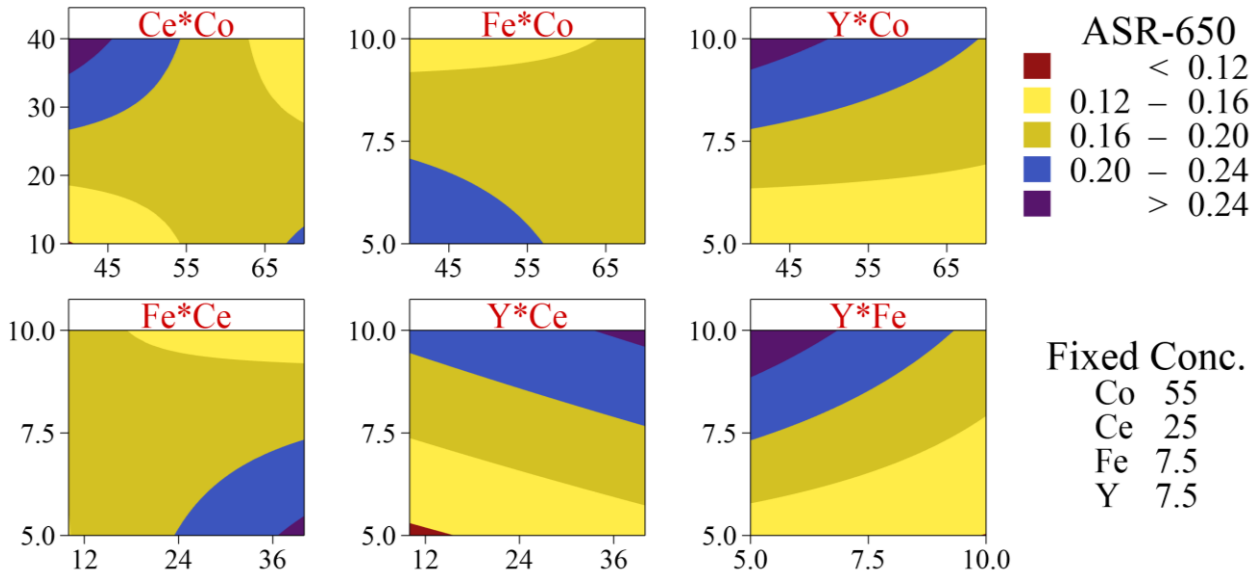

Figure S19: Contour plots of two-factor interactions for ASR at 650 °C.

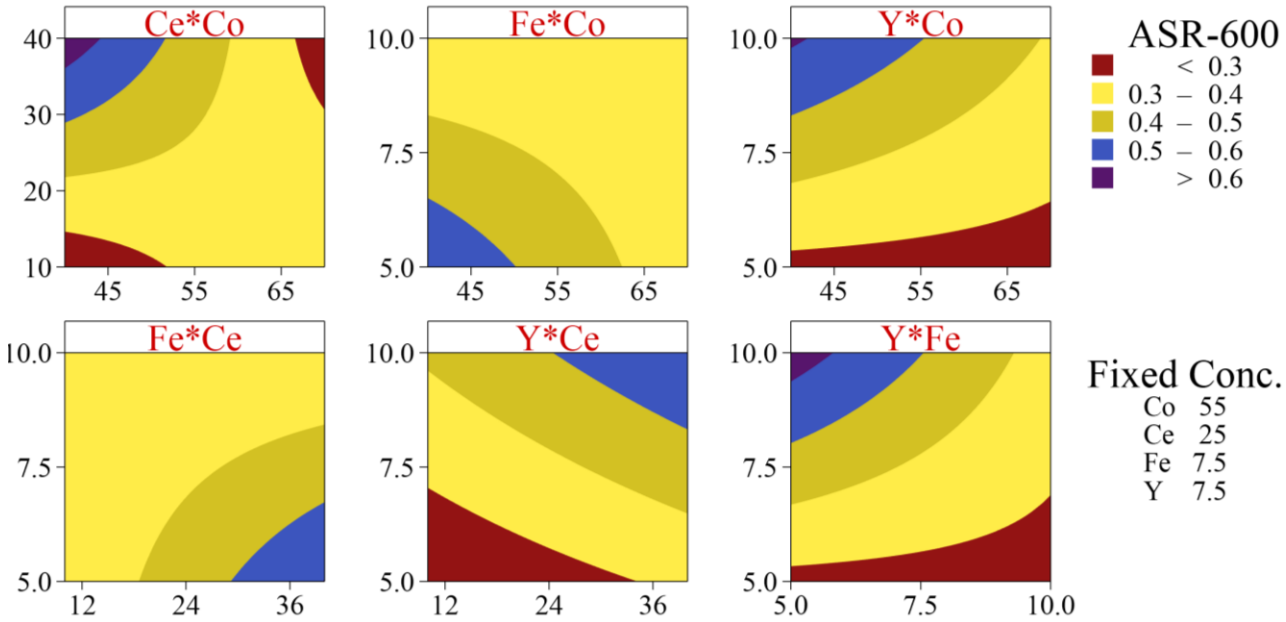

Figure S20: Contour plots of the significant two-factor interactions for ASR at 600 °C.

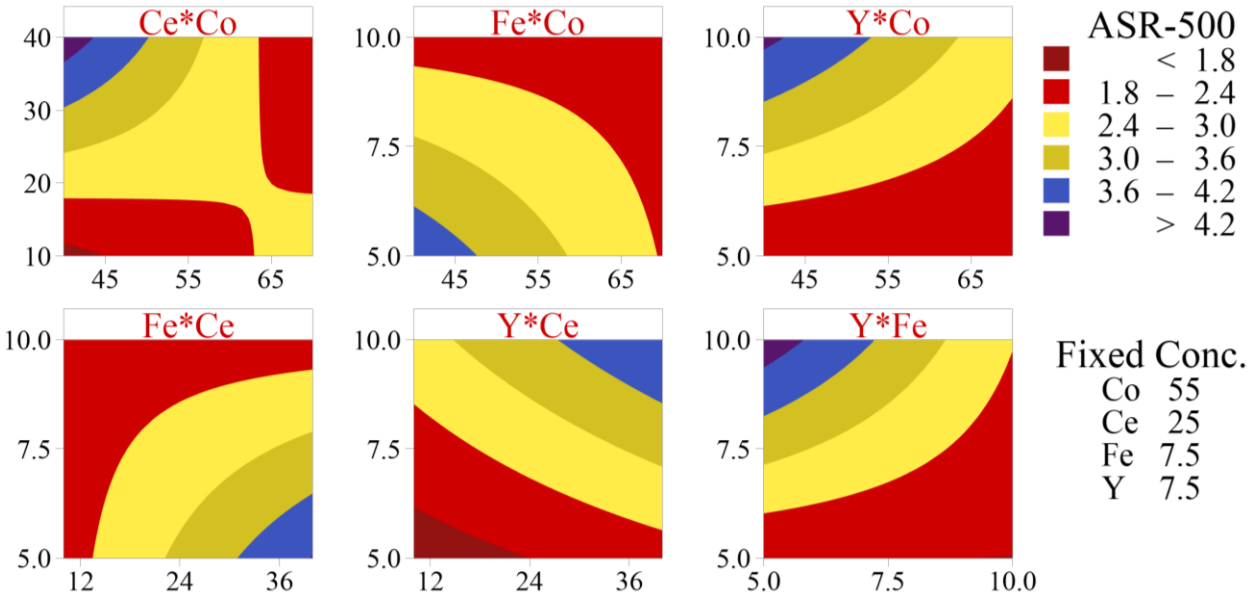

Figure S21: Contour plots of the significant two-factor interactions for ASR at 500 ºC.

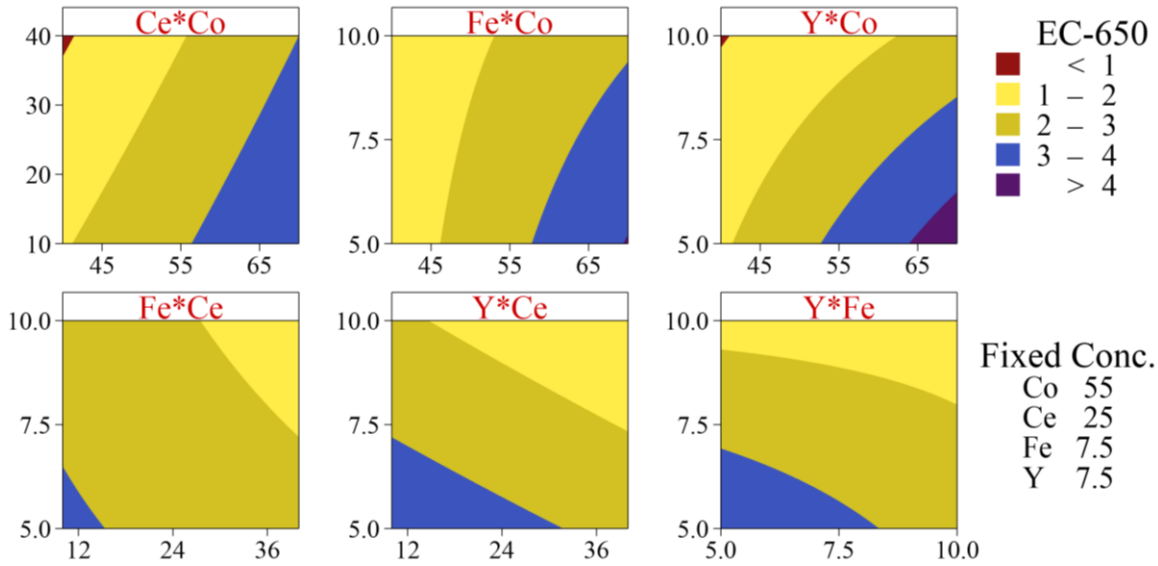

Figure S22: Contour plots of the significant two-factor interactions for electronic conductivity at 650 ºC.

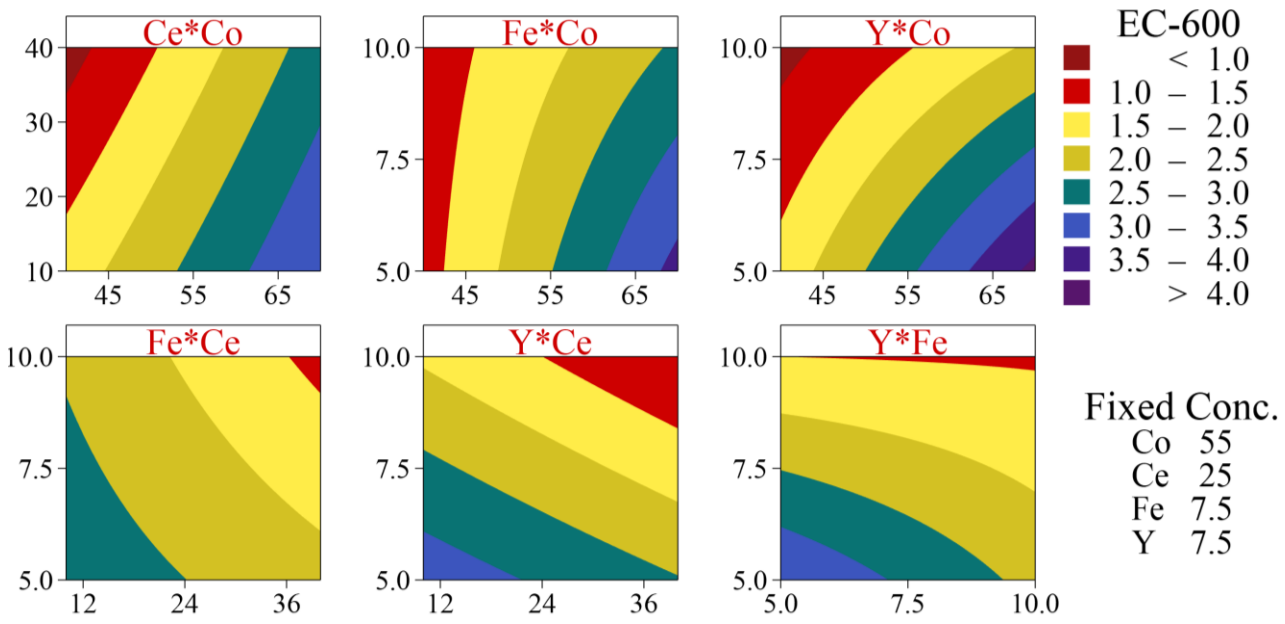

Figure S23: Contour plots of the significant two-factor interactions for electronic conductivity at 600 ºC.

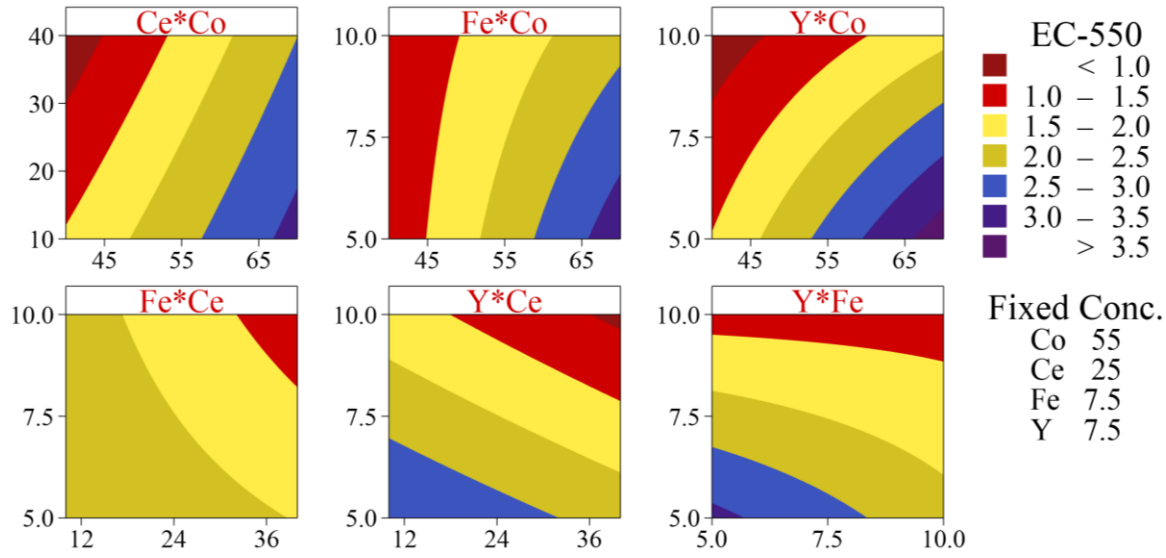

Figure S24: Contour plots of the significant two-factor interactions for electronic conductivity at 550 ºC.

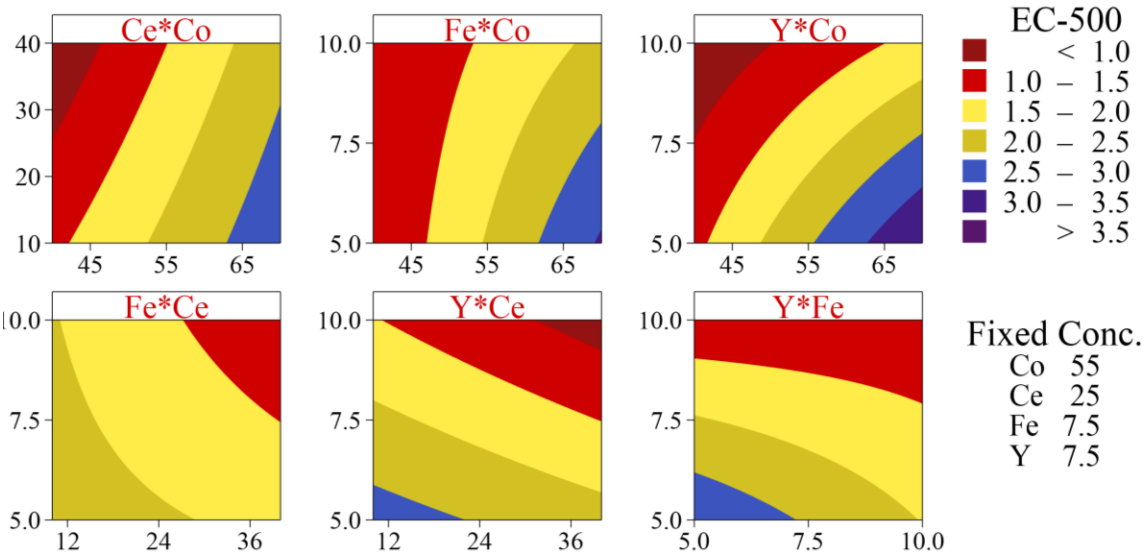

Figure S25: Contour plots of the significant two-factor interactions for electronic conductivity at 500 ºC.

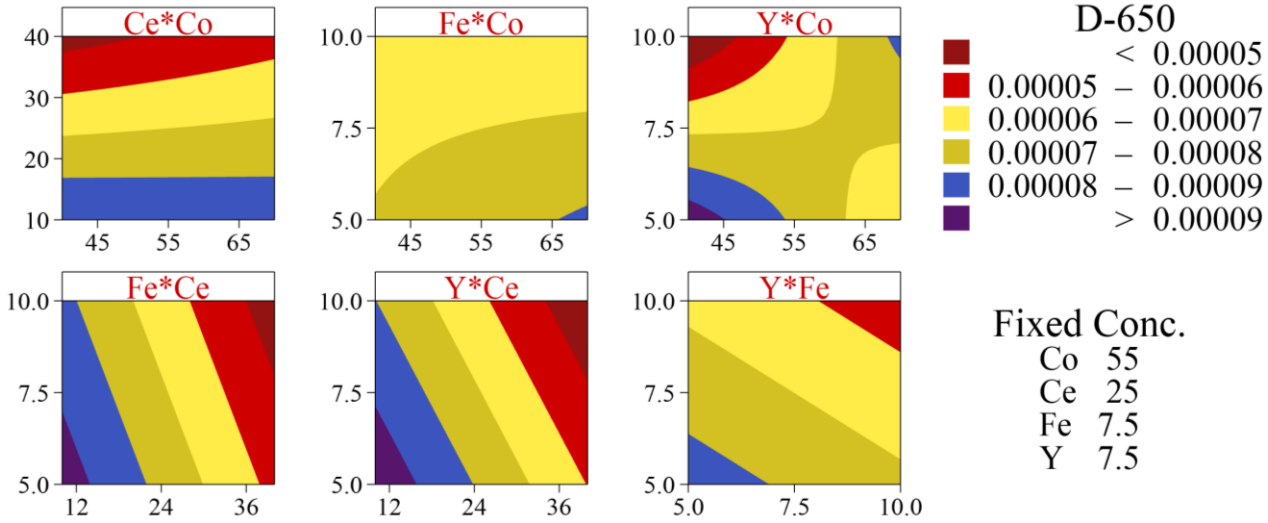

Figure S26: Contour plots of two-factor interactions for D_{chem} at 650 ºC.

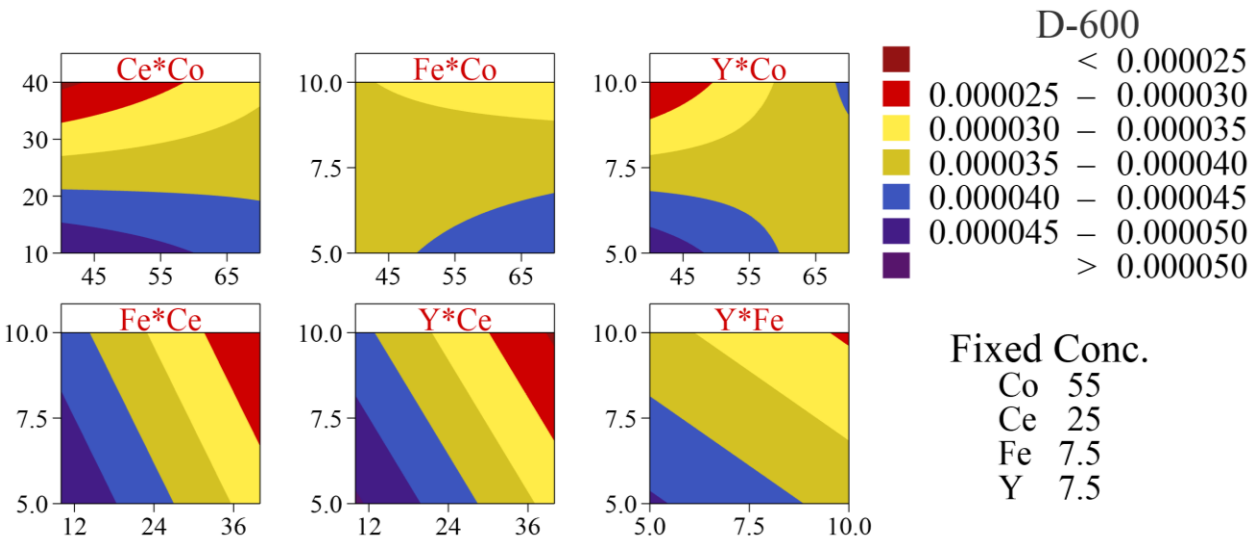

Figure S27: Contour plots of two-factor interactions for D_{chem} at 600 ºC.

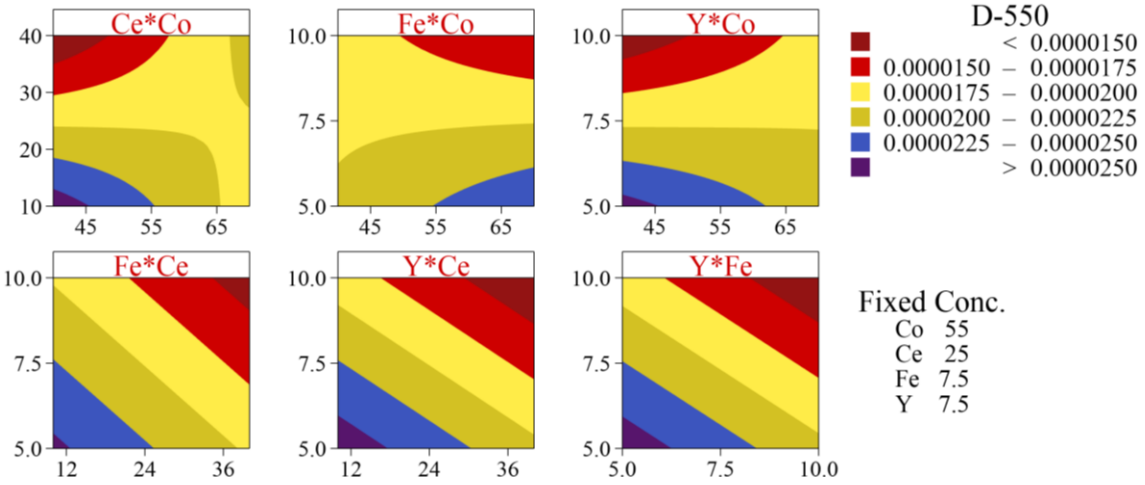

Figure S28: Contour plots of two-factor interactions for D_{chem} at 550 ºC.

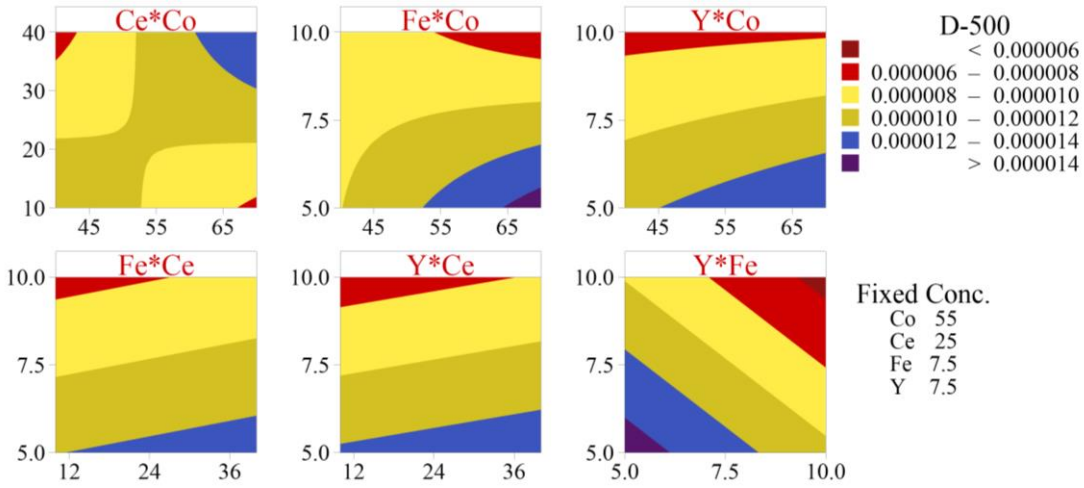

Figure S29: Contour plots of two-factor interactions for D_{chem} at 500 ^{o}C.

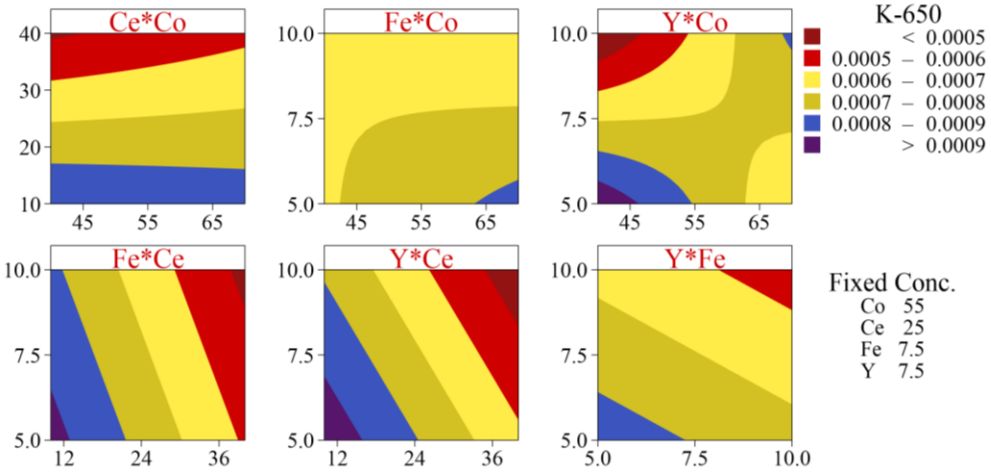

Figure S30: Contour plots of two-factor interactions for k_{chem} at 650 ^{o}C.

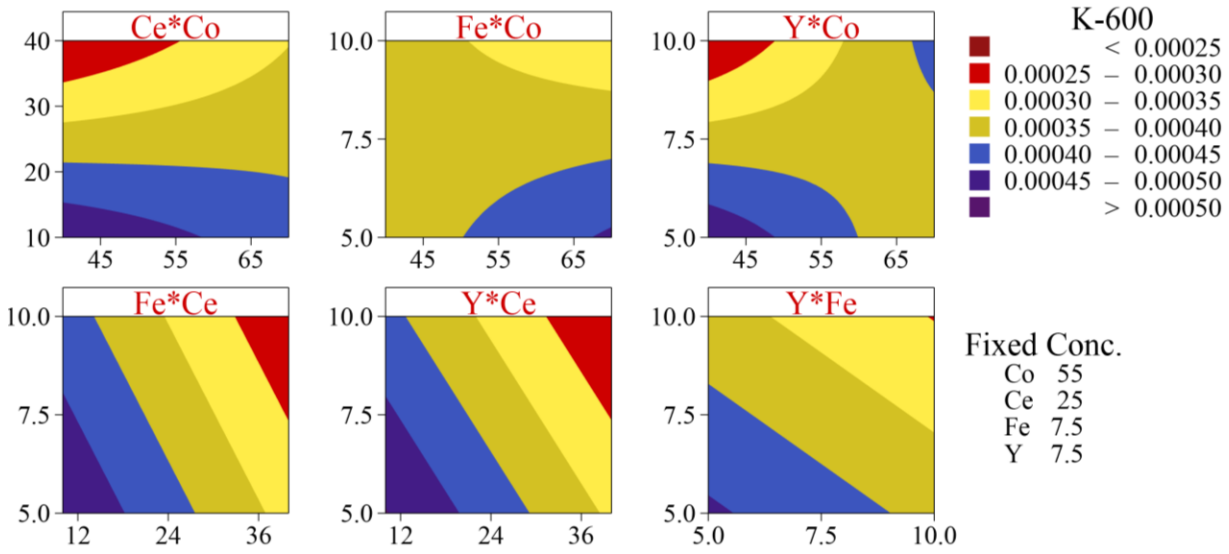

Figure S31: Contour plots of two-factor interactions for k_{chem} at 600 ºC.

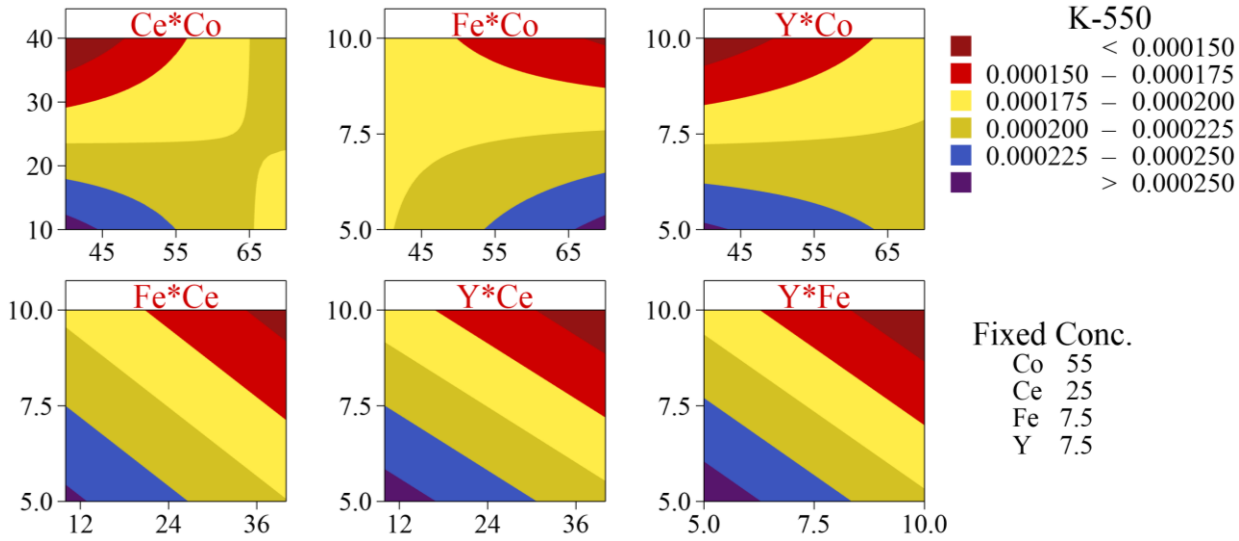

Figure S32: Contour plots of two-factor interactions for k_{chem} at 550 ºC.

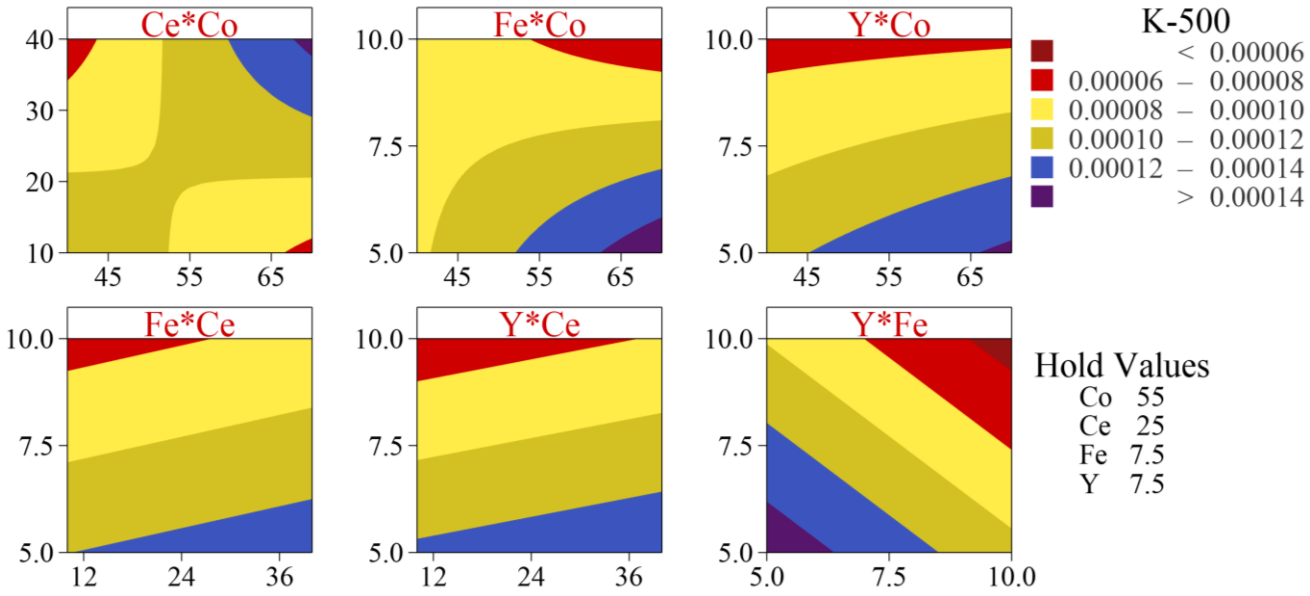

Figure S33: Contour plots of two-factor interactions for k_{chem} at 500 °C.

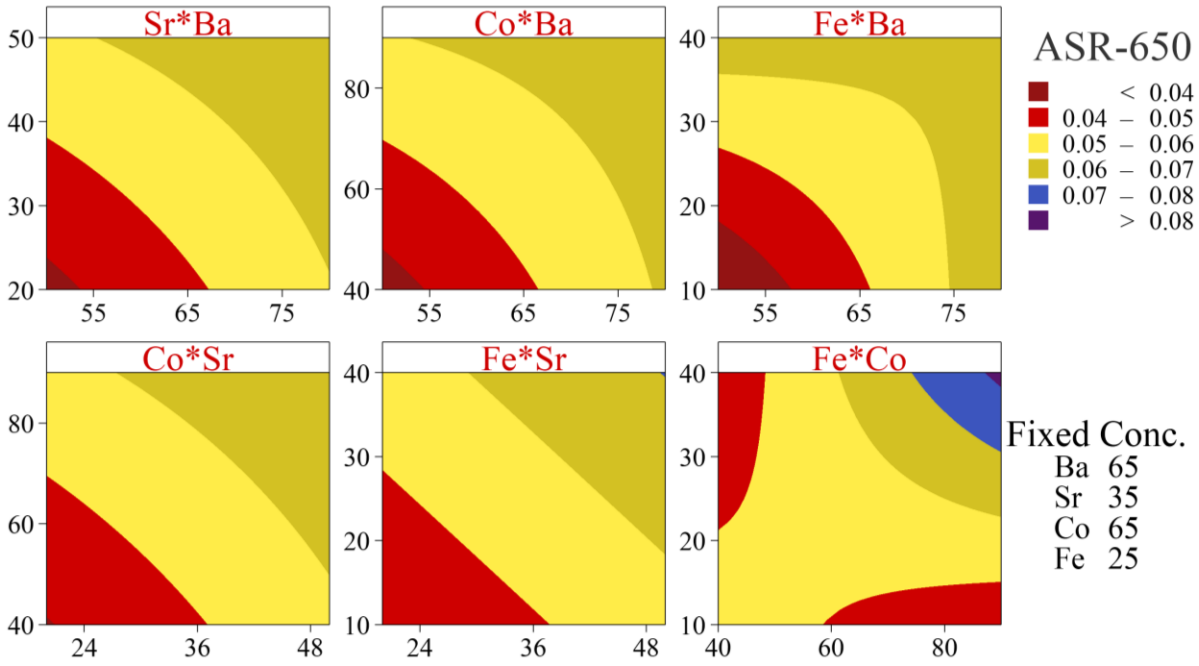

Figure S34: Contour plots of two-factor interactions for ASR of BSCF at 650 °C.

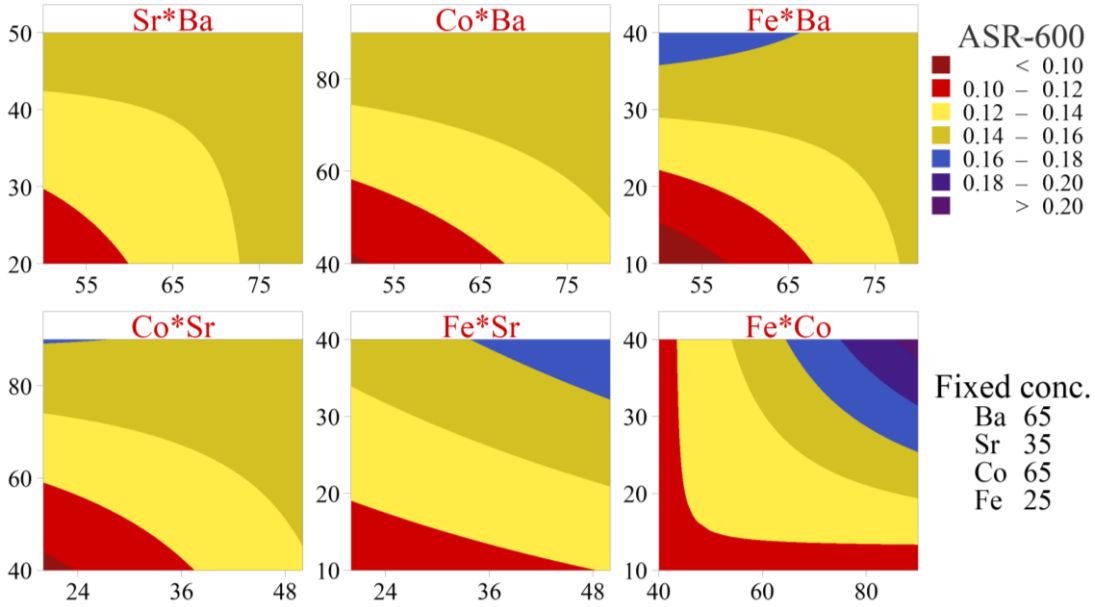

Figure S35: Contour plots of two-factor interactions for ASR of BSCF at 600 ºC.

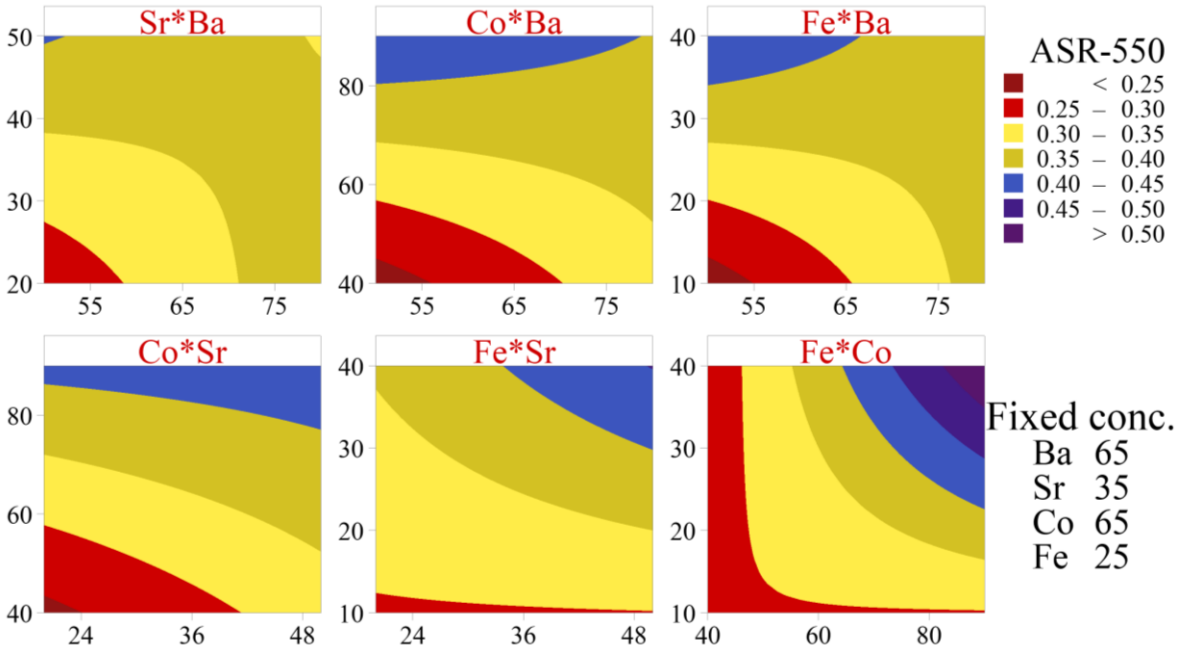

Figure S36: Contour plots of two-factor interactions for ASR of BSCF at 550 ºC.

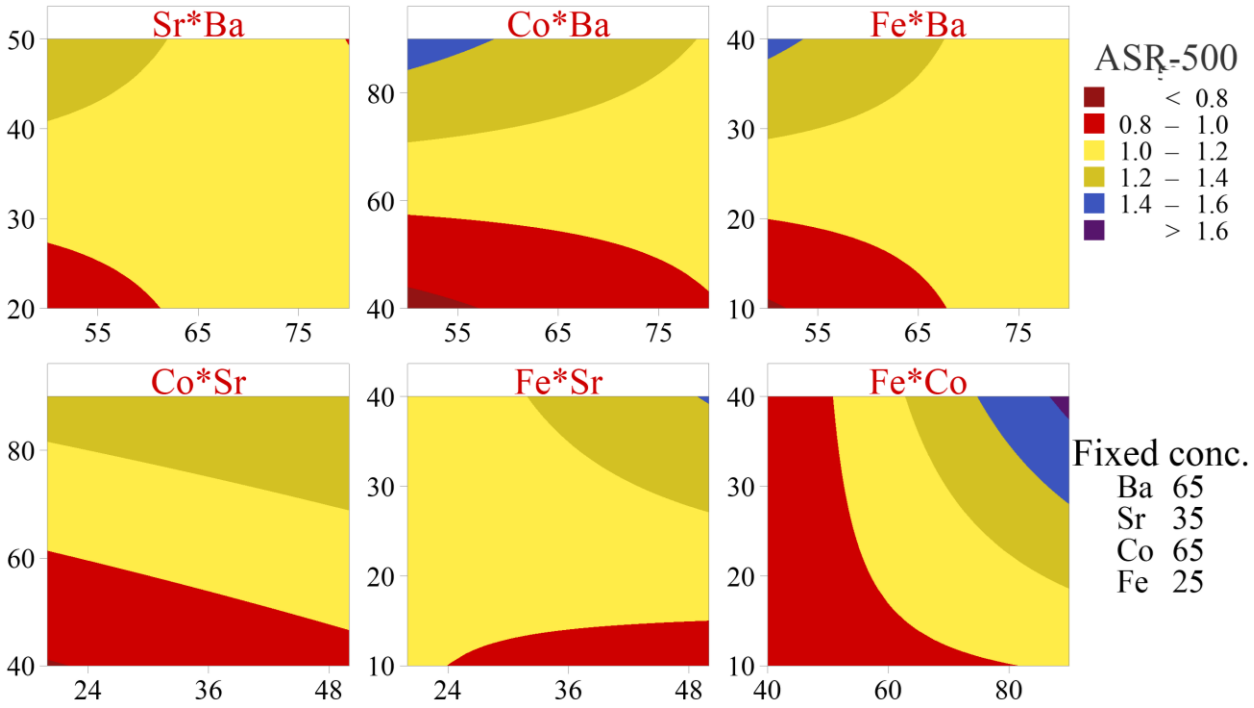

Figure S37: Contour plots of two-factor interactions for ASR of BSCF at 500 ºC.

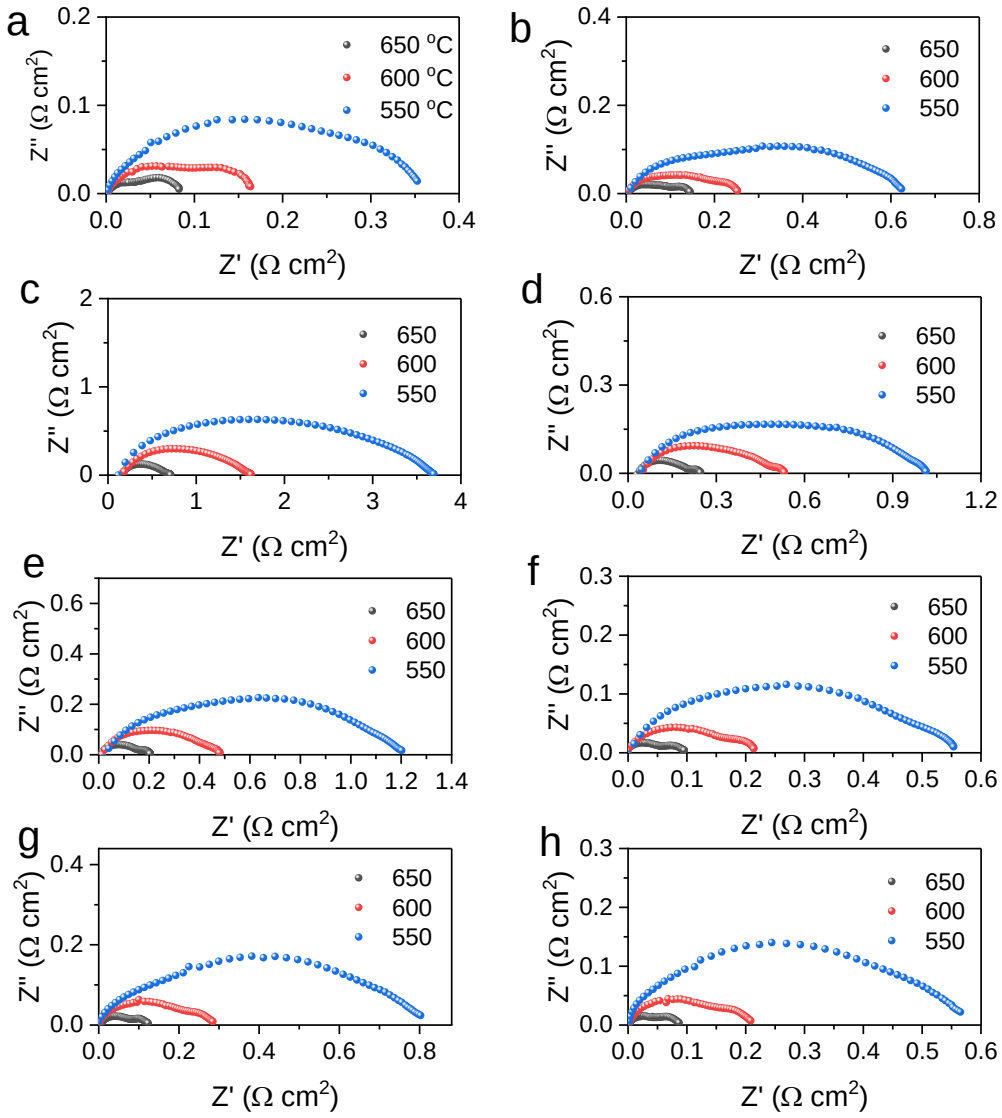

Figure S38: Electrochemical impedance spectra of the first replicate of symmetrical cells (based on the half fraction of the total independent conditions) with BCZYYb electrolyte and $BaCo_{\alpha}Ce_{\beta}Fe_{\gamma}Y_{\zeta}O_{3-\delta}$ nanocomposite cathodes (a) S1 (b) S2 (c) S3 (d) S 4 (e) S5 (f) S6 (g) S7 (h) S8.

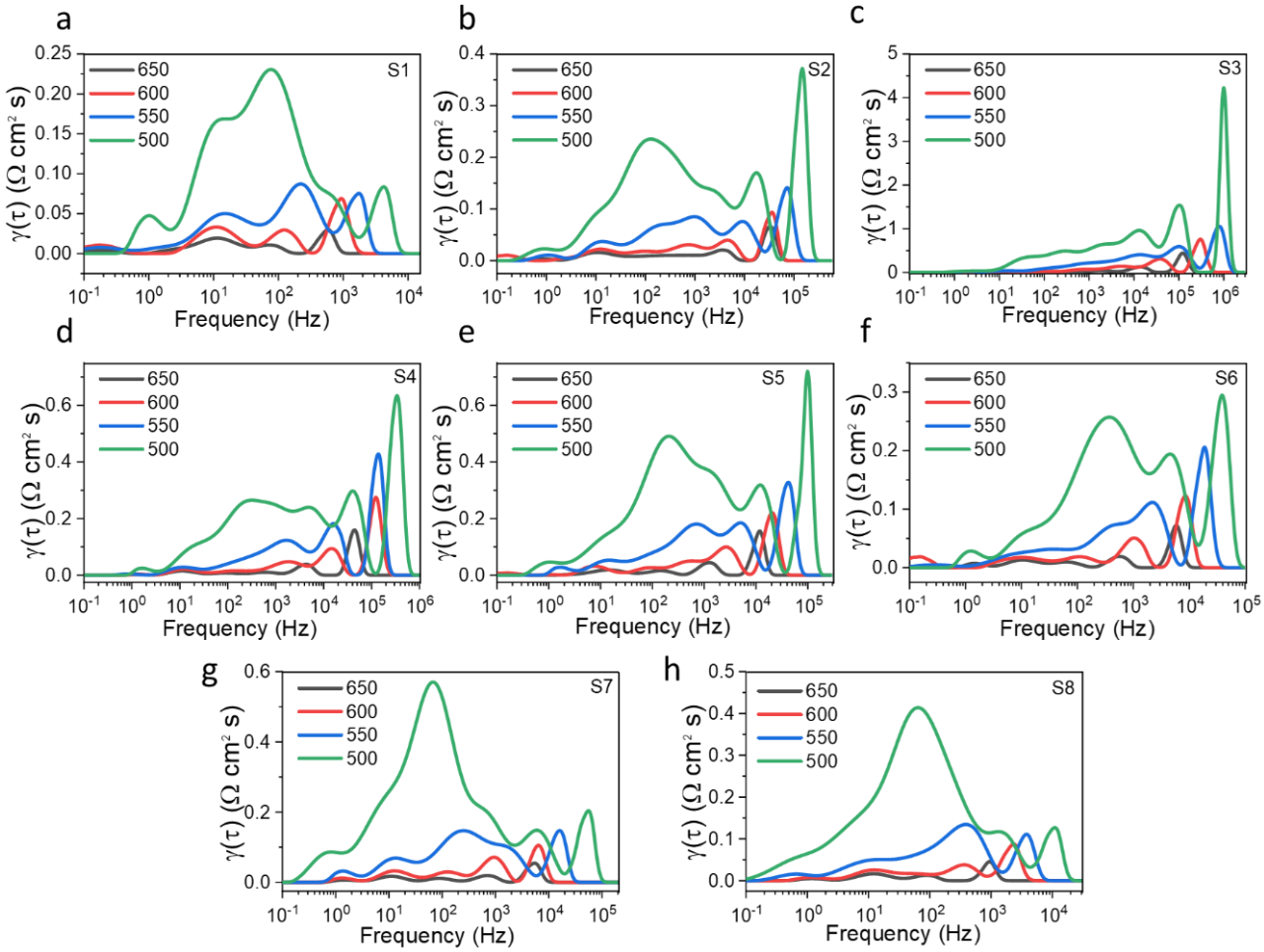

Figure S39: Distribution of relaxation time (DRT) analysis of (a) S1 (b) S2 (c) S3 (d) S4 (e) S5 (f) S6 (g) S7 (h) S8.

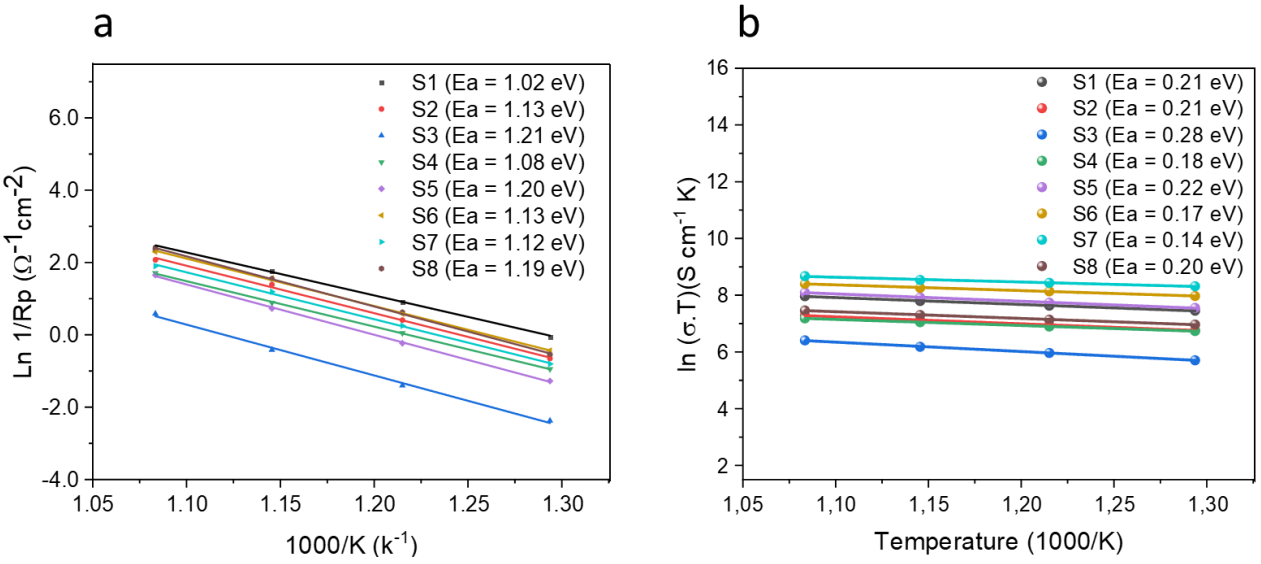

Figure S40: Activation energies of samples S1-S8 for BCCFY series (a) ASR (b) Electrical conductivity.

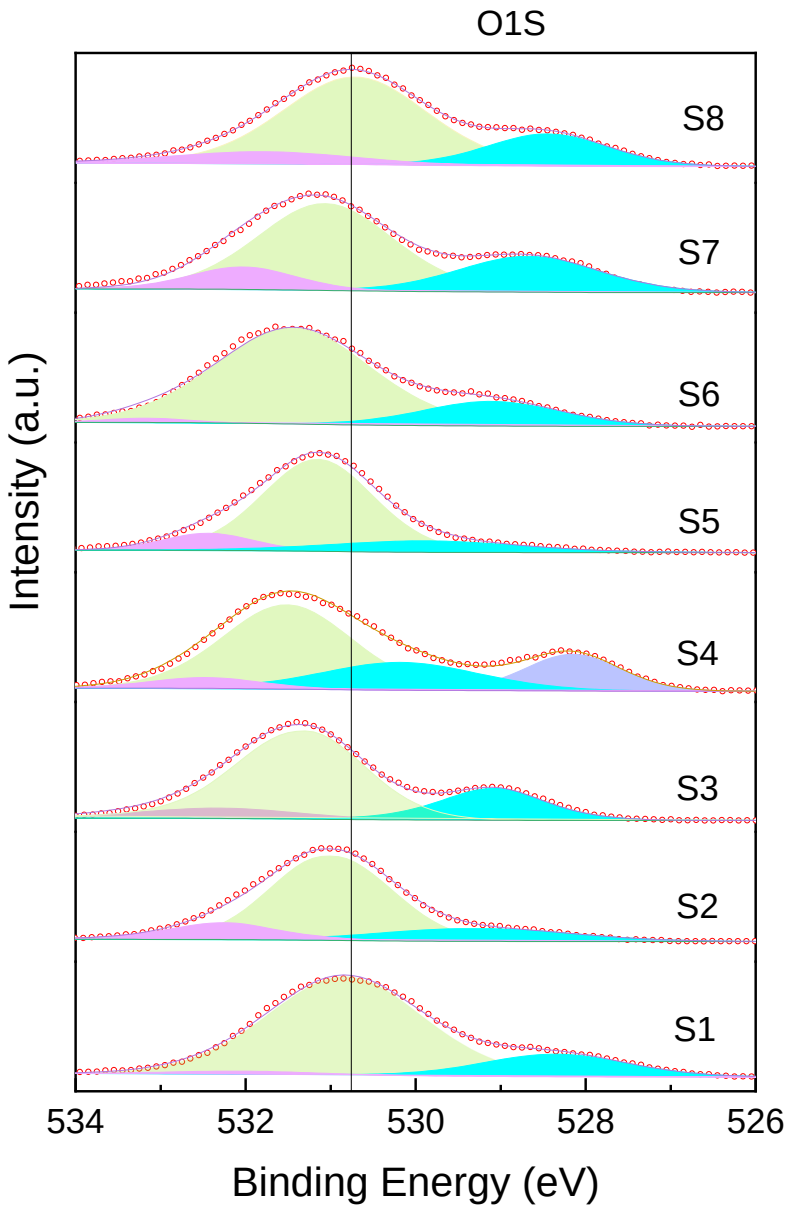

Figure S41: XPS spectra of O1s for S (1-8).

Table S48: Composition of the lattice oxygen, adsorbed oxygen, and adsorbed water in $BaCo_{\alpha}Ce_{\beta}Fe_{\gamma}Y_{\zeta}O_{3-\delta}$ nanocomposite.

Sample	Adsorbed water		Adsorbed oxygen		Lattice oxygen	
	Position (eV)	Percentage (%)	Position (eV)	Percentage (%)	Position (eV)	Percentage (%)
1	531.86	2.05	530.66	80.63	528.19	17.32
2	532.21	13.50	530.95	69.67	529.19	16.83
3	532.26	9.71	531.28	69.51	529.05	20.78
4	532.46	6.05	531.50	54.65	528.15	17.43
5	532.49	11.04	531.20	73.42	529.94	15.55
6	533.21	1.89	531.48	79.86	529.14	18.25
7	532.05	12.29	531.08	61.46	528.69	26.25
8	531.81	11.30	530.74	67.78	528.48	20.92

Note: Sample 4 has an additional highly oxidative oxygen peak at position 530.17 eV and with a relative percentage of 21.87 %

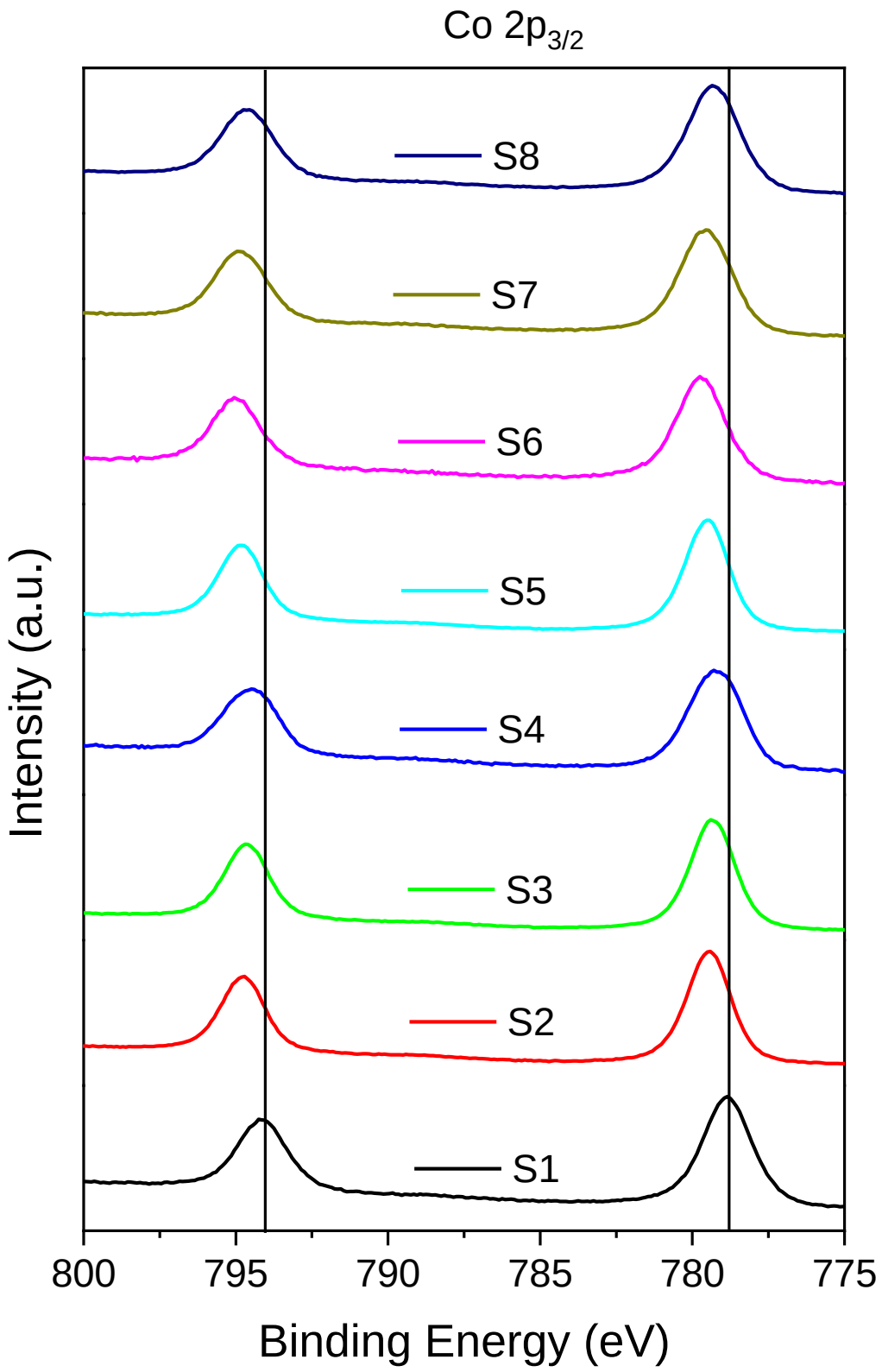

Figure S42: XPS spectra of Co2p for S (1-8).

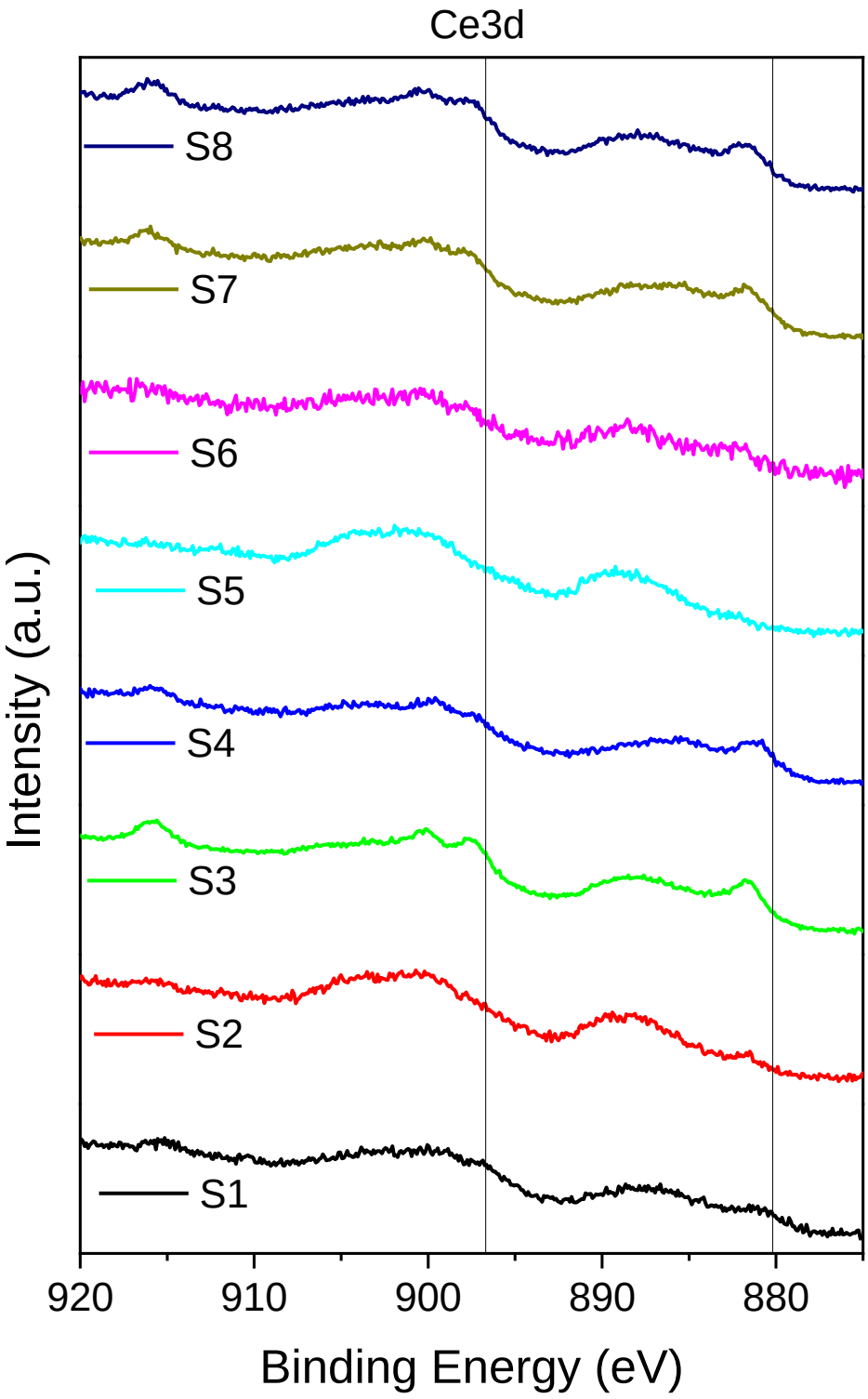

Figure S43: XPS spectra of Ce3d for S (1-8).

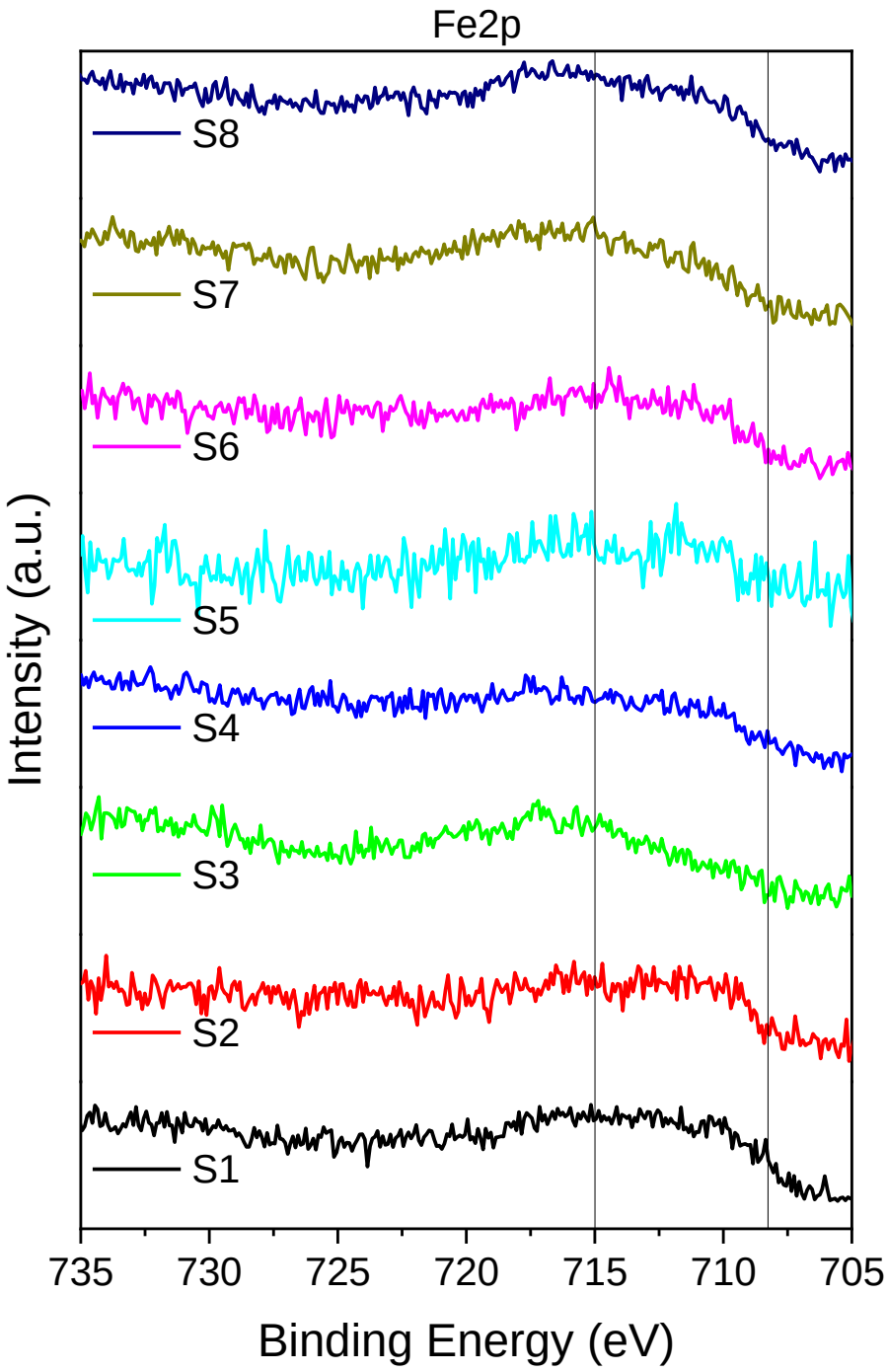

Figure S44: XPS spectra of Fe2p for S (1-8).

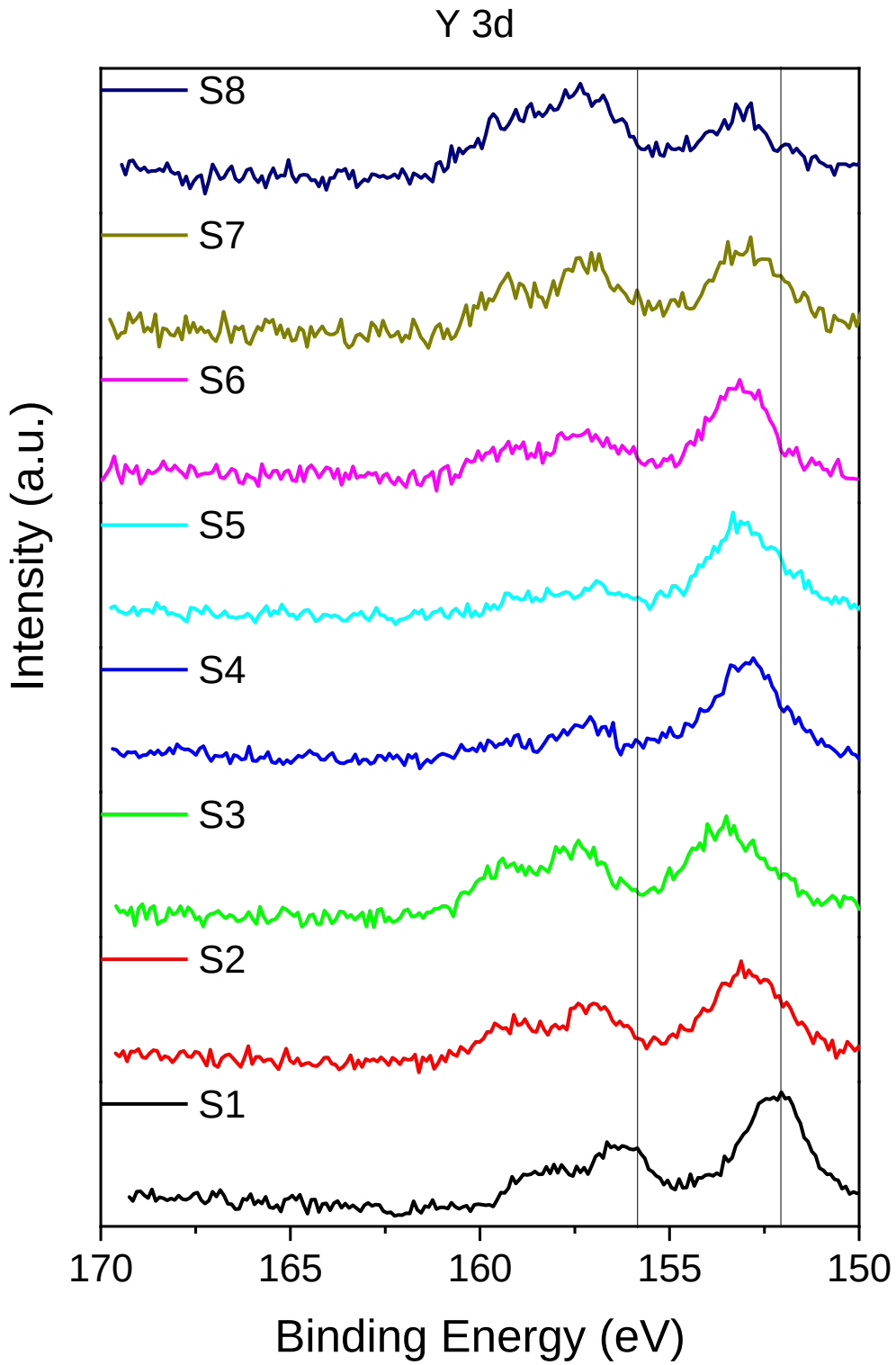

Figure S45: XPS spectra of Y3d for S (1-8).

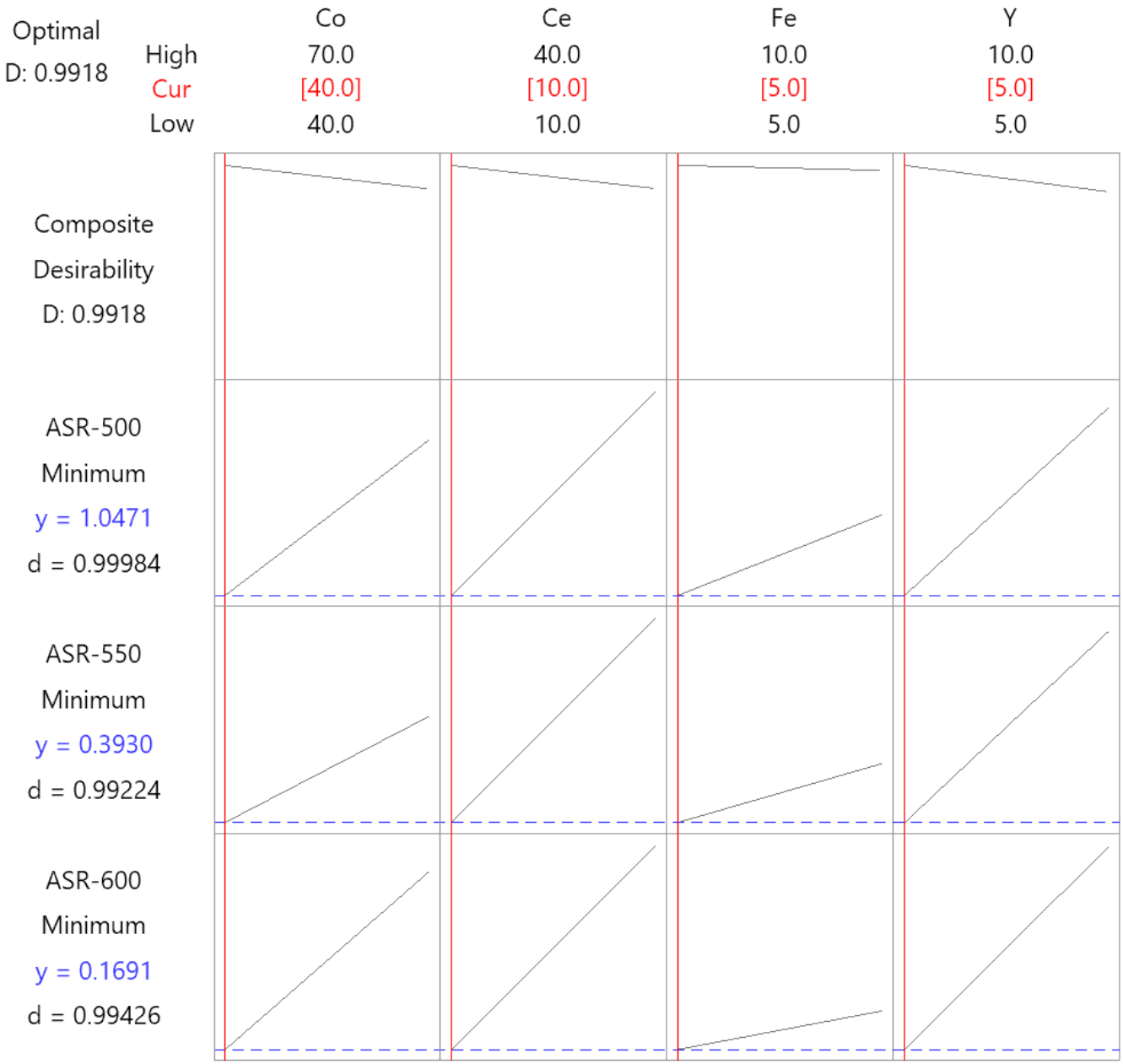

Figure S46: Response optimization system for ASRs of BCCFY series.

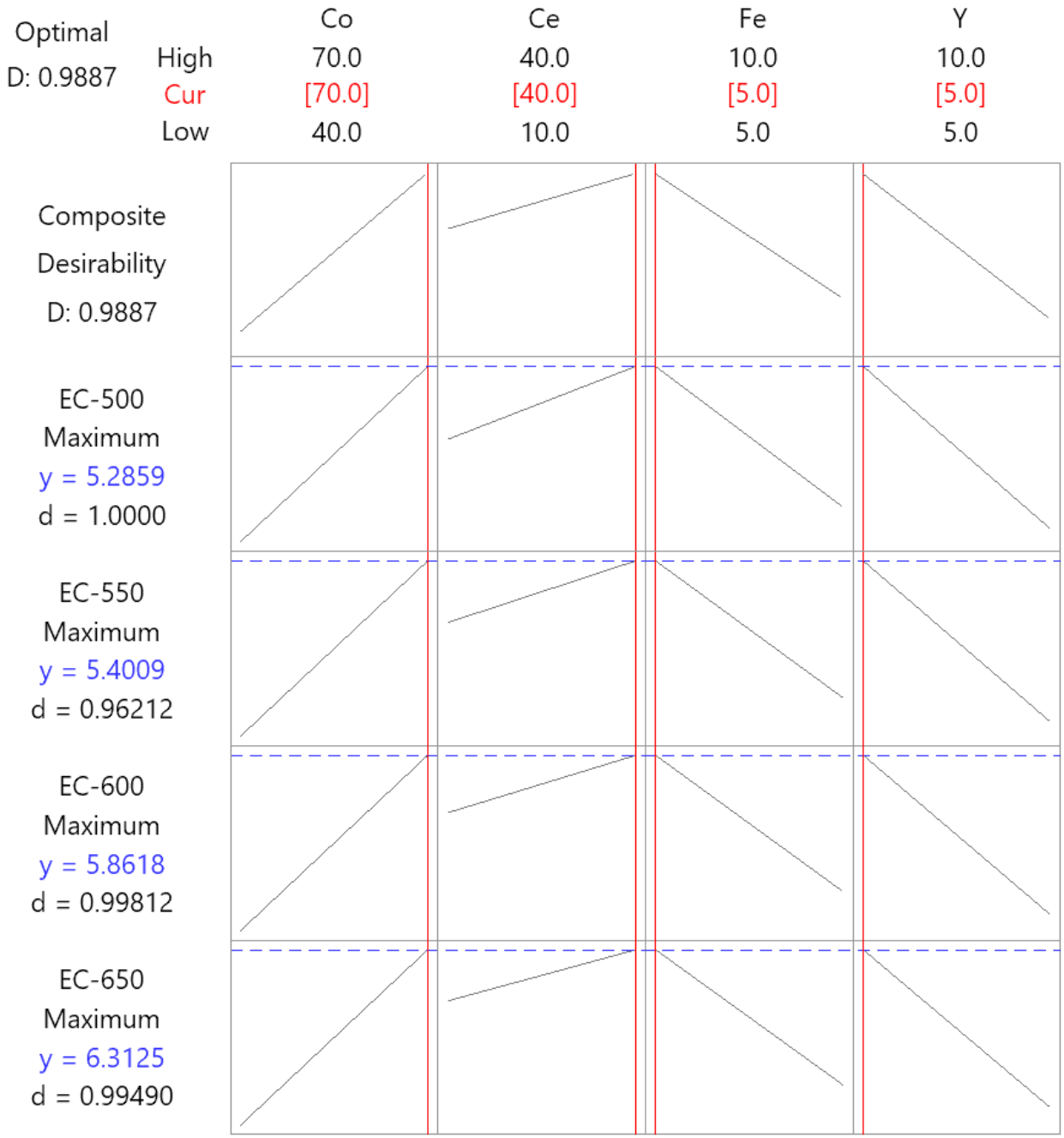

Figure S47: Response optimization system for ECs.

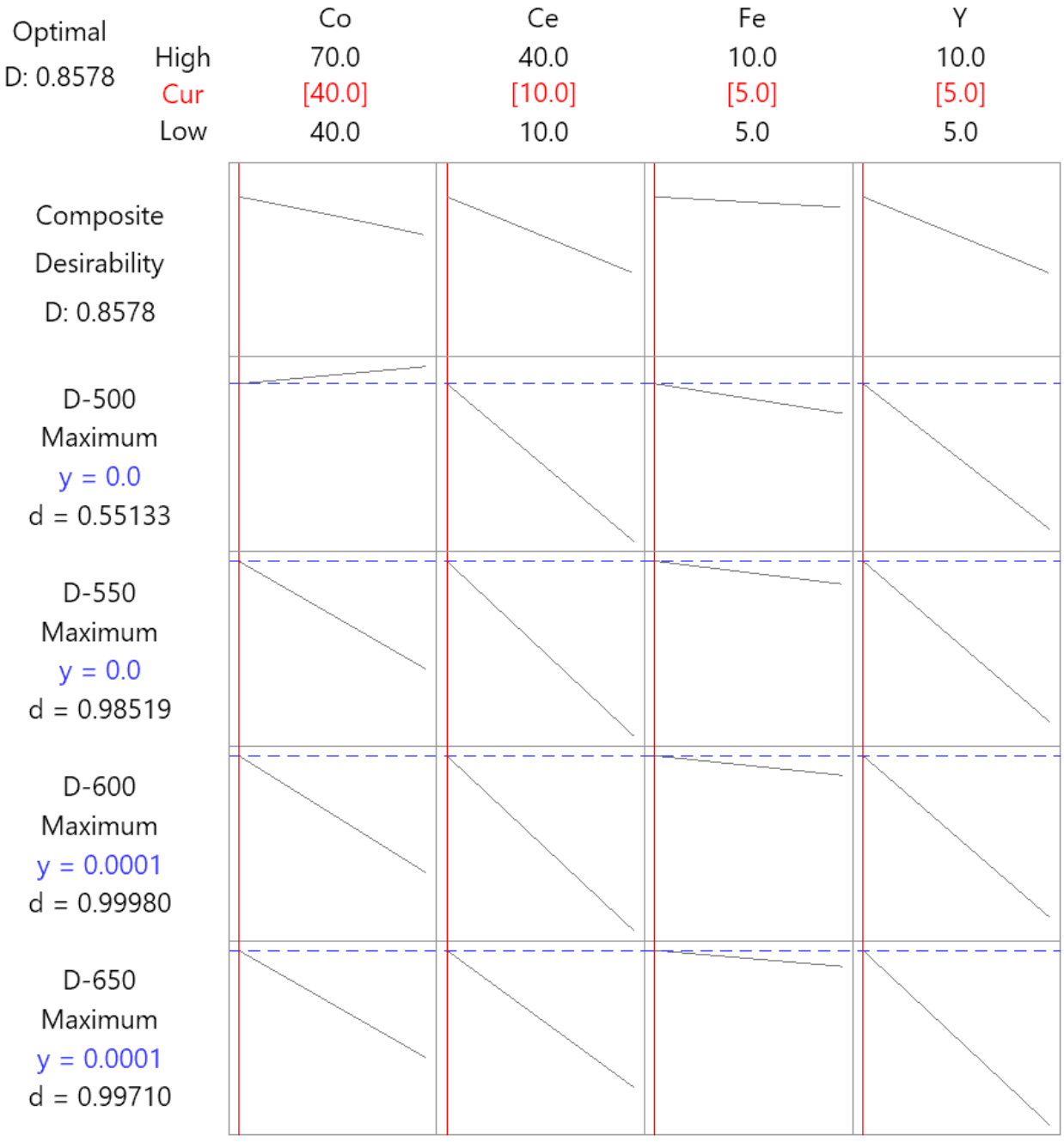

Figure S48: Response optimization system for D_{chem}.

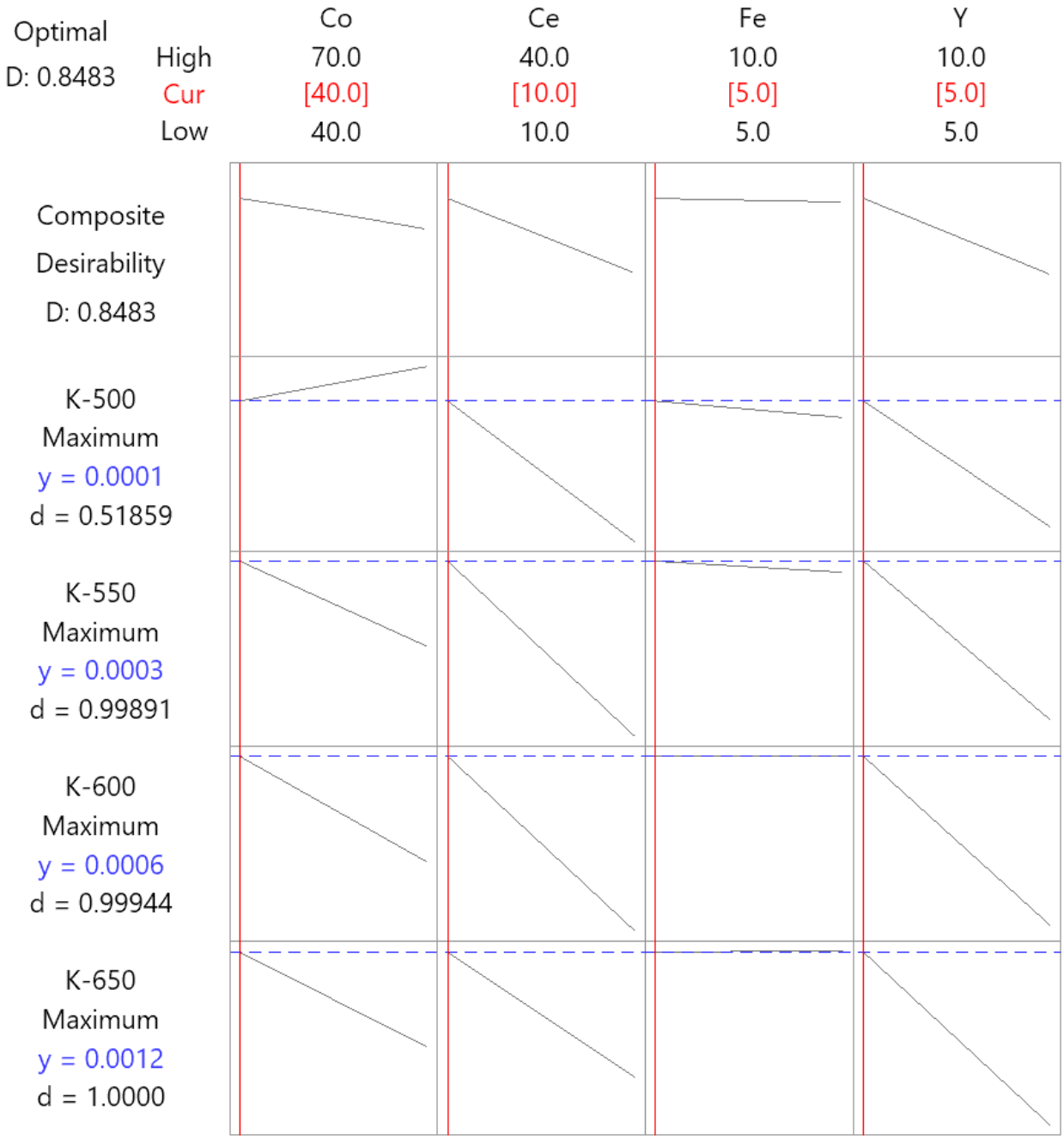

Figure S49: Response optimization system for k_{chem}.

Table S49: Joint optimization solution for all ASR responses.

Solution	Co	Ce	Fe	Y	ASR-500 Fit	ASR-550 Fit	ASR-600 Fit	ASR-650 Fit	Composite Desirability
1	40	10	5	5	1.04715	0.39305	0.169086	0.0871988	0.991822

Table S50: Joint optimization solution for all EC responses.

Solution	Co	Ce	Fe	Y	EC-500 Fit	EC-550 Fit	EC-600 Fit	EC-650 Fit	Composite Desirability
1	70	40	5	5	5.28591	5.40086	5.86178	6.31250	0.988662

Table S51: Joint optimization solution for all D_{chem} responses.

Solution	Co	Ce	Fe	Y	D-500 Fit	D-550 Fit	D-600 Fit	D-650 Fit	Composite Desirability
1	40	10	5	5	0.0000143	0.0000336	0.0000630	0.0001207	0.857820

Table S52: Joint optimization solution for all k_{chem} responses.

Solution	Co	Ce	Fe	Y	K-500 Fit	K-550 Fit	K-600 Fit	K-650 Fit	Composite Desirability
1	**40**	**10**	**5**	**5**	**0.0001412**	**0.0003257**	**0.0006127**	**0.00118**	**0.848256**

Table S53: Refined X-ray Diffraction Data for As-Synthesized BCCFY-1 Nanocomposite

Element	Wyckoff position	x	y	z	Occupancy
Phase 1 (Pm-3m; a=b=c=4.12147, 89 wt.%)					
Ba	1a	0	0	0	1
Co	1b	0.500	0.500	0.500	0.8
Y	1b	0.500	0.500	0.500	0.2
O	3c	0	0	0	1
Phase 2 (R-3c; a=b=6.22155 c=14.79442, 10 wt.%)					
Ba	6a	0	0	-0.2500	1
Ce	6b	0	0	0	0.8
Fe	6b	0	0	0	0.2
O	18e	0.4487	0	0.2500	1
Phase 3 (Pnma; a= 6.15758 b=8.79433 c=6.21294, 1 wt.%)					
Ba	4a	0.1230	0.2500	-0.0038	1
Ce	4b	0	0	0.5000	1
O1	4b	0.4910	0.0377	0.7302	1
O3	8d	0.2707	0.2500	0.0710	1

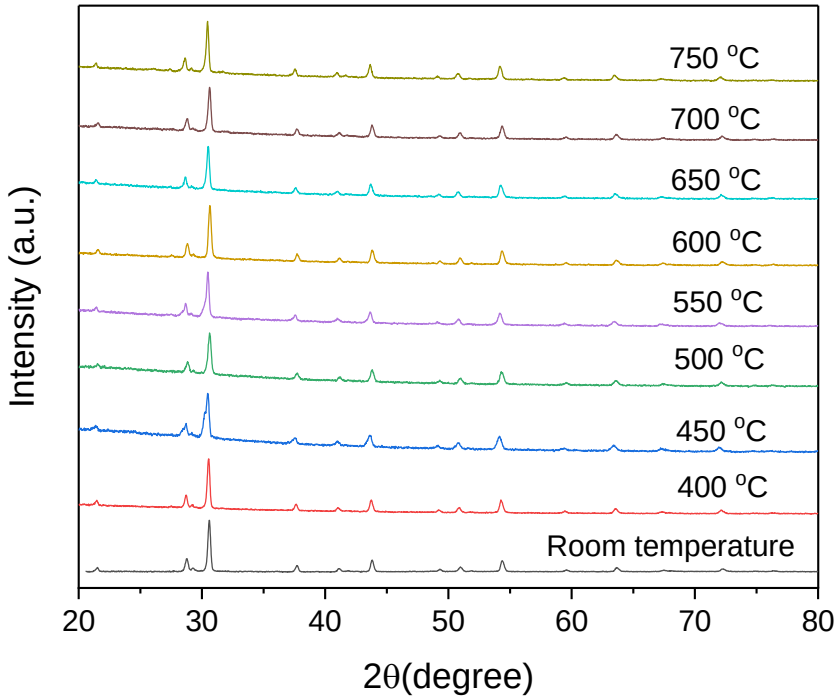

Figure S50: HT-XRD patterns of $BaCo_{0.667}Ce_{0.167}Fe_{0.083}Y_{0.083}O_{3-\delta}$ powder.

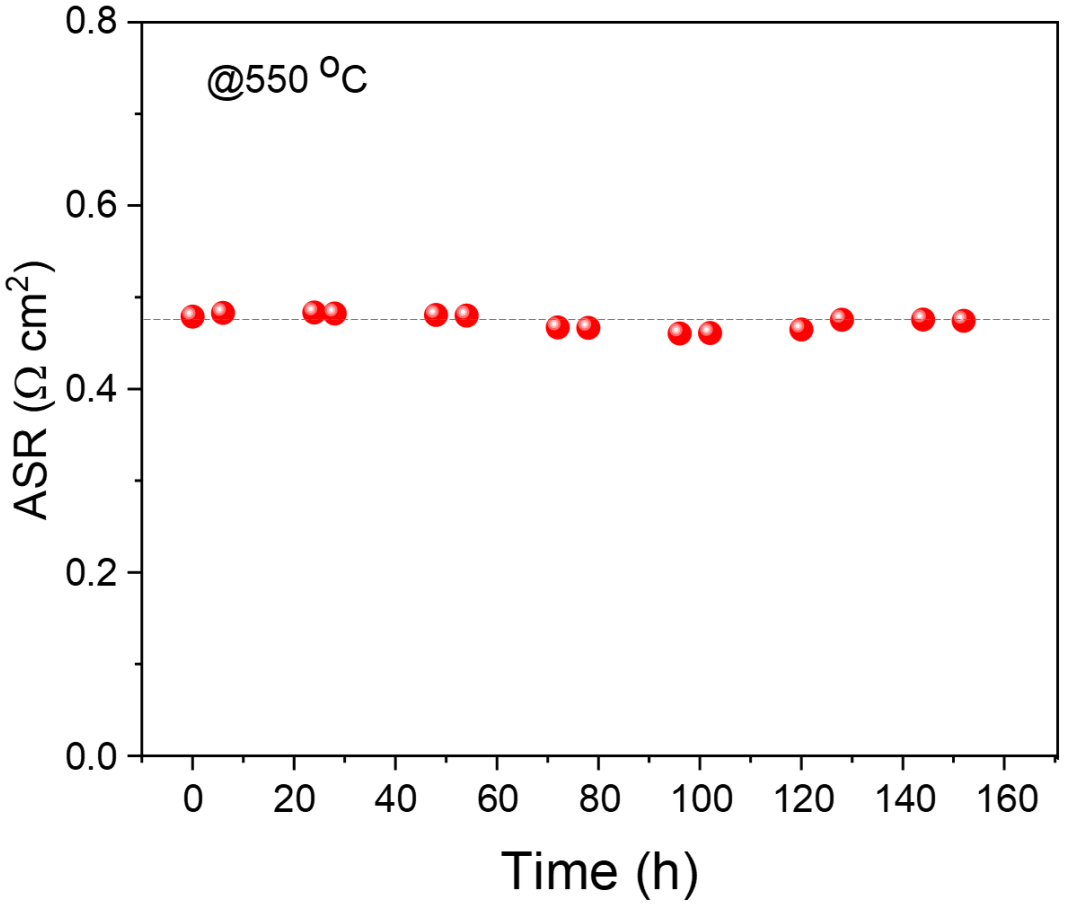

Figure S51: ASR stability of symmetrical proton conducting cell based on $BaCo_{0.667}Ce_{0.167}Fe_{0.083}Y_{0.083}O_{3-\delta}$ cathode material in 3% H_2O-air at 550 °C.

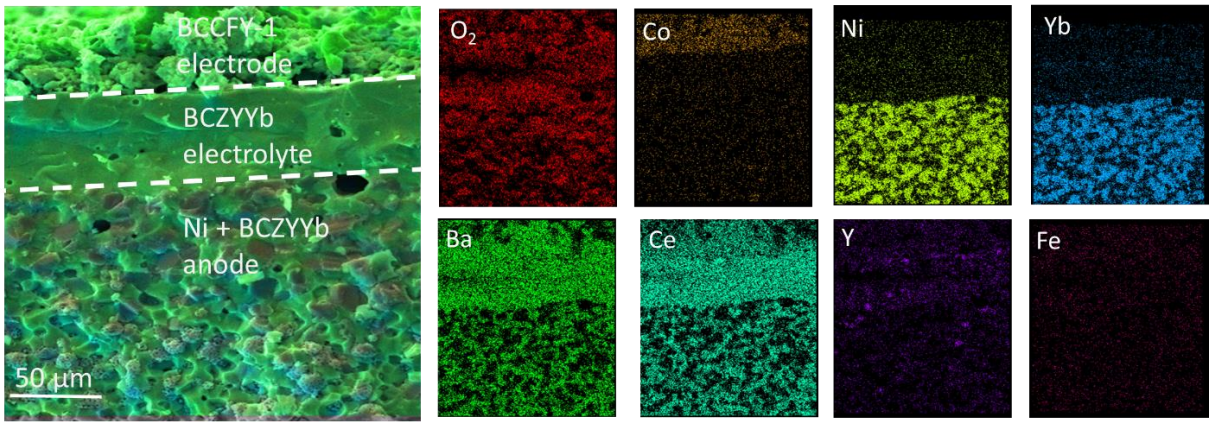

Figure S52: SEM image of Ni + BCZYYb | BCZYYb | BCCFY-1 and the elemental distribution of Ba, Ce, Y, Fe, O_2, Ni and Yb.

Table S54: Performance comparison of BCCFY cathode with previously developed cathode materials.

Cathode	Electrolyte	Anode	PPD (mW cm^{-2})		Ref.
			650 °C	600 °C	
BCF36	BCZY721	Ni+BCZY721	900	525	[6]
BCF55	BCZY721	Ni+BCZY721	276	192	[7]
BCF55	BCZYYb7111	Ni+ BCZYYb7111	175	133	[8]
BCFC	BCZYYb7111	Ni+ BCZYYb7111	287	237	[9]
BCCY	BCZYYb7111	Ni+ BCZYYb7111	985	743	[10]
BSCF	BCZY721	Ni+BCZY721	-	356	[11]
PBC	BCZY721	Ni+BCZY721	-	305	[12]
BCFY	BCZYYb7111	Ni+ BCZYYb7111	829	656	[13]
BYC	BCZY721	Ni+BCZY721	175	-	[14]
BCFN	BCZY721	Ni+BCZY721	70	40	[15]
BCCFZ	BCZYYb7111	Ni+ BCZYYb7111	1054	683	[16]
LNO-LNF	BCZY721	Ni+BCZY721	364	266	[17]
SFNb	BCZY721	Ni+BCZY721	-	428	[18]
BCFZY	BCZYYb7111	Ni+ BCZYYb7111	807	672	[16]
LSM-SDC	BCZYYb7111	Ni+ BCZYYb7111	-	580	[19]
LSCF6428- BCYb10	BCY91	Ni+ BCY91	-	150	[20]
PBC- BZYP	BZY20	Ni+BZY20	-	169	[21]
$PrBaCo_2O_{5+\delta}$	BCZY721	Ni+BCZY721	-	305	[12]
BCCFY-S1	BCZYYb7111	Ni+ BCZYYb7111	1421	942	This work

BCF36: $BaCe_{0.36}Fe_{0.64}O_{3-\delta}$, BCF55: $BaCe_{0.5}Fe_{0.5}O_{3-\delta}$, BCFC: $BaCo_{0.2}Ce_{0.4}Fe_{0.4}O_{3-\delta}$ BCCY: $BaCo_{0.7}Ce_{0.24}Y_{0.06}O_{3-\delta}$ BSCF: $Ba_{0.5}Sr_{0.5}Co_{0.8}Fe_{0.2}O_{3-\delta}$, PBC: $PrBaCo_2O_{5+\delta}$, BCFY: $BaCe_{0.16}Y_{0.04}Fe_{0.8}O_{3-\delta}$, BYC: $Ba_2YCu_3O_{6+\delta}$, BCFN: $BaCe_{0.5}Fe_{0.4}Ni_{0.1}O_{3-\delta}$, BCCFZ: $BaCe_{0.4}Co_{0.4}Fe_{0.1}Zr_{0.1}O_{3-\delta}$, , LNO-LNF: $La_2Ni\ O_{4+\delta}$-$LaNi_{0.6}Fe_{0.4}O_{3-\delta}$, SFNb: $SrFe_{0.95}Nb_{0.05}O_{3-\delta}$, BCFZY: $BaCo_{0.4}Fe_{0.4}Zr_{0.1}Y_{0.1}O_{3-\delta}$, LSM-SDC: $La_{0.75}Sr_{0.25}MnO_{3-\delta}$ - $Ce_{0.8}Sm_{0.2}O_{2-\delta}$, LSCF6428-BCYb91: $La_{0.8}Sr_{0.2}Co_{0.8}Fe_{0.2}O_{3-\delta}$ - $BaCe_{0.9}Yb_{0.1}O_{3-\delta}$, PBC- BZYP: $PrBaCo_2O_{5+\delta}$- $BaZr_{0.7}Y_{0.2}Pr_{0.1}O_{3-\delta}$, BCZYYb7111: $BaCe_{0.7}Zr_{0.1}Y_{0.1}Yb_{0.1}O_{3-\delta}$, BCZY721: $BaCe_{0.7}Zr_{0.2}Y_{0.1}O_{3-\delta}$,; BCY91: $BaCe_{0.9}Y_{0.1}O_{3-\delta}$, BCCFY-S1: $BaCo_{0.667}Ce_{0.167}Fe_{0.083}Y_{0.083}O_{3-\delta}$

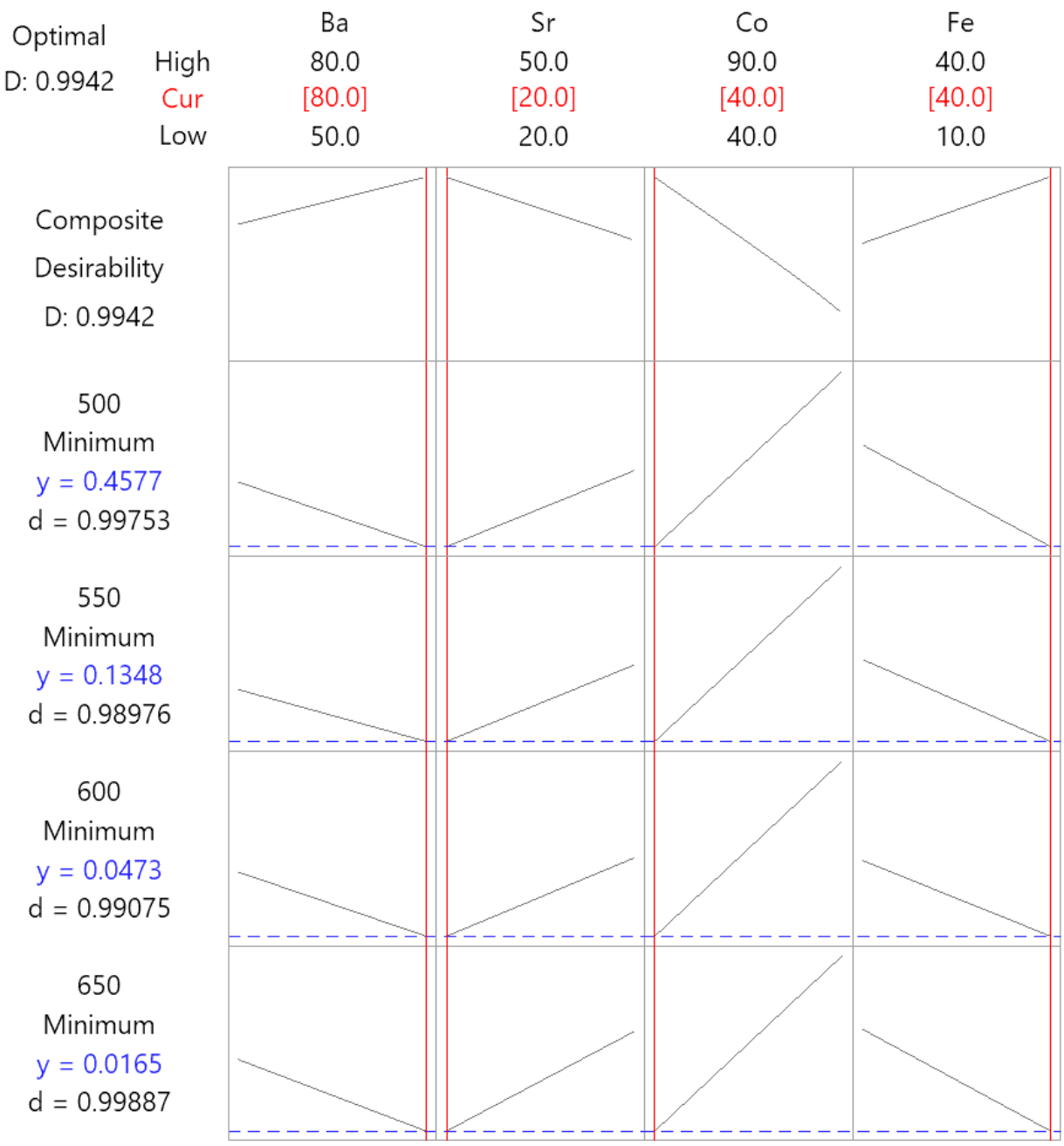

Figure S53: Response optimization system of ASR for BSCF series.

Table S55: Joint optimization solution for all ASR responses of BSCF series.

Solution	Ba	Sr	Co	Fe	500 Fit	550 Fit	600 Fit	650 Fit	Composite Desirability
1	80	20.0000	40	40.0000	0.457714	0.134790	0.047292	0.0165158	0.994220

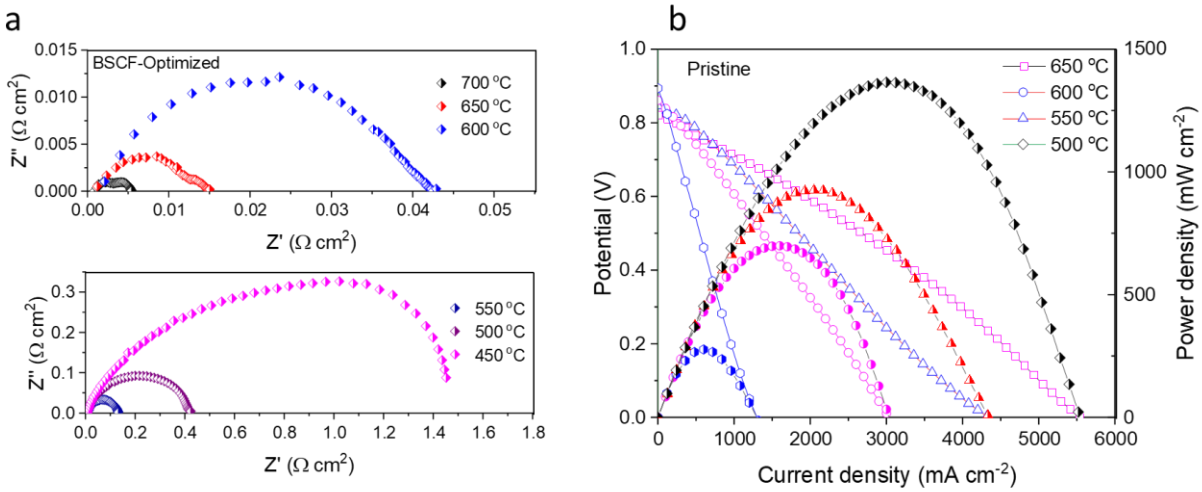

Figure S54: (a) Nyquist plots of BSCF-optimized|SDC|BSCF-optimized symmetrical cell from 450-650 ºC (b) I-V-P curves of Ni + SDC|SDC|BSCF-pristine from 500 – 650 ºC.

Table S56: Synthesized concentration for Samples 1 and 2 derived from the matrix of experiments.

Sample No.	Co	Ce	Fe	Y	$BaCo_{\alpha}Ce_{\beta}Fe_{\gamma}Y_{\varsigma}O_{3-\delta}$			
					α	β	γ	ζ
					(% mol. Concentration)			
1	-1	-1	-1	-1	66.67	16.67	8.33	8.33
2	-1	-1	+1	+1	57.14	14.29	14.29	14.29

Table S57: ICP-OES test data for Samples 1 and 2 having similar XRD profiles.

Sample number	Sample mass (g)	Final volume (mL)	Element	Element concentration in test solution (mg/L)	Dilution factor	Element concentration in digestion solution/original sample solution (mg/L)	Element concentration in the sample (mg/kg)
1	0.0441	10	Ba	21.4217	100	2142.1700	485752.83
	0.0441	10	Co	6.4809	100	648.0880	146958.73
	0.0441	10	Fe	0.6623	100	66.2308	15018.32
	0.0441	10	Ce	3.6424	100	364.2430	82594.78
	0.0441	10	Y	1.1467	100	114.6680	26001.81
2	0.0445	10	Ba	21.2592	100	2125.9200	477734.83
	0.0445	10	Co	5.3806	100	538.0640	120913.26
	0.0445	10	Fe	1.1213	100	112.1250	25196.63
	0.0445	10	Ce	3.1124	100	311.2420	69942.02
	0.0445	10	Y	1.9154	100	191.5350	43041.57

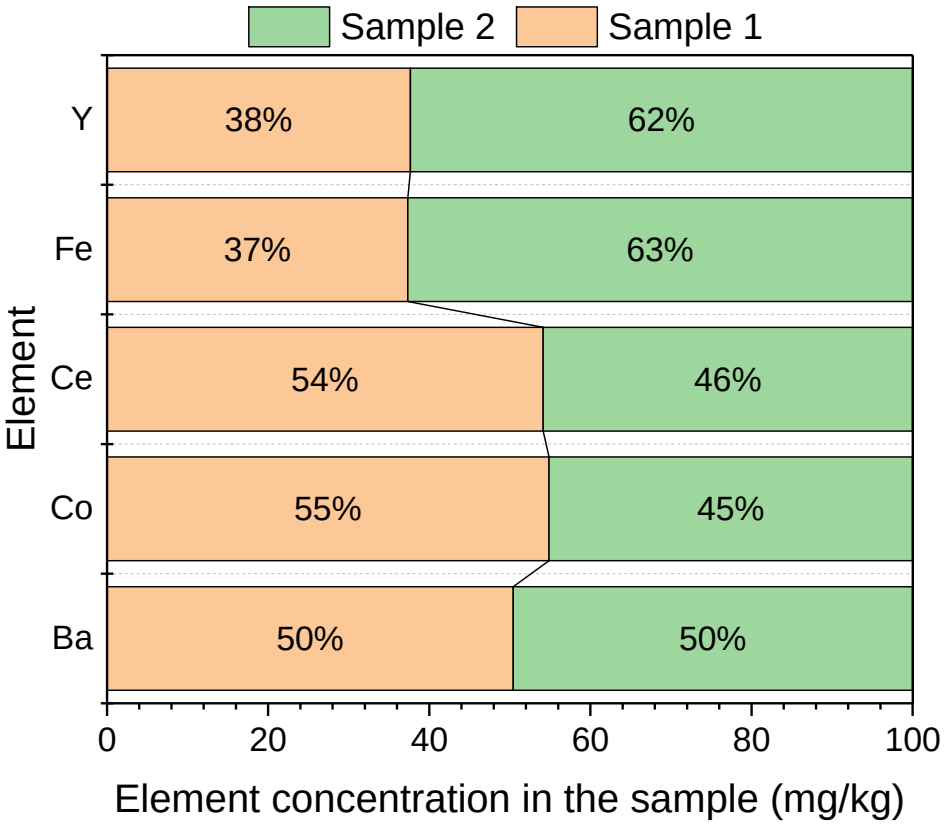

Figure S55: 100% stacked bar of the ICP-OES of samples 1 and 2 with similar XRD profile.

References

1. Minitab, Inc. (2020). MINITAB.
2. Danilov, N., Lyagaeva, J., Vdovin, G., Medvedev, D., Demin, A., and Tsiakaras, P. (2017). Electrochemical Approach for Analyzing Electrolyte Transport Properties and Their Effect on Protonic Ceramic Fuel Cell Performance. ACS Appl Mater Interfaces *9*, 26874–26884. 10.1021/acsami.7b07472.
3. Rodriguez-Carvajal, J. (1990). FULLPROF: a program for Rietveld refinement and pattern matching analysis. In satellite meeting on powder diffraction of the XV congress of the IUCr.
4. Chen, D., and Shao, Z. (2011). Surface exchange and bulk diffusion properties of Ba0.5Sr 0.5Co0.8Fe0.2O3-δ mixed conductor. Int J Hydrogen Energy *36*, 6948–6956. 10.1016/j.ijhydene.2011.02.087.
5. Lenth, R. v. (1989). Quick and easy analysis of unreplicated factorials. Technometrics *31*, 469–473. 10.1080/00401706.1989.10488595.
6. Tong, H., Fu, M., Yang, Y., Chen, F., and Tao, Z. (2022). A Novel Self-Assembled Cobalt-Free Perovskite Composite Cathode with Triple-Conduction for Intermediate Proton-Conducting Solid Oxide Fuel Cells. Adv Funct Mater *32*, 2209695. 10.1002/adfm.202209695.
7. Tao, Z., Bi, L., Zhu, Z., and Liu, W. (2009). Novel cobalt-free cathode materials BaCe x Fe 1 − x O 3 − ? for proton-conducting solid oxide fuel cells. *194*, 801–804. 10.1016/j.jpowsour.2009.06.071.
8. Zhao, Z., Zou, M., Huang, H., Zhai, X., Wofford, H., and Tong, J. (2022). Insight of BaCe0.5Fe0.5O3−δ twin perovskite oxide composite for solid oxide electrochemical cells. Journal of the American Ceramic Society, 1–15. 10.1111/jace.18643.
9. Zhao, Z., Cui, J., Zou, M., Mu, S., Huang, H., Meng, Y., He, K., Brinkman, K.S., and Tong, J. (Joshua) (2020). Novel twin-perovskite nanocomposite of Ba–Ce–Fe–Co–O as a promising triple conducting cathode material for protonic ceramic fuel cells. J Power Sources *450*, 227609. 10.1016/j.jpowsour.2019.227609.
10. Song, Y., Chen, Y., Wang, W., Zhou, C., Zhong, Y., Yang, G., Zhou, W., Liu, M., and Shao, Z. (2019). Self-Assembled Triple-Conducting Nanocomposite as a Superior Protonic Ceramic Fuel Cell Cathode. Joule *3*, 2842–2853. 10.1016/j.joule.2019.07.004.
11. Wan, T.-T., Zhu, A.-K., Li, H.-B., Wang, C.-C., Guo, Y.-M., Shao, Z.-P., and Savadogo, O. (2018). Performance variability of Ba0.5Sr0.5Co0.8Fe0.2O3−δcathode on proton-conducting electrolyte SOFCs with Ag and Au current collectors. Rare Metals *37*, 633–641. 10.1007/s12598-017-0942-5.
12. Lin, Y., Ran, R., Zhang, C., Cai, R., and Shao, Z. (2010). Performance of PrBaCo2O5+δ as a Proton-Conducting Solid-Oxide Fuel Cell Cathode. J Phys Chem A *114*, 3764–3772. 10.1021/jp9042599.
13. Zou, D., Yi, Y., Song, Y., Guan, D., Xu, M., Ran, R., Wang, W., Zhou, W., and Shao, Z. (2022). The BaCe0.16Y0.04Fe0.8O3-d nanocomposite: A new high-performance cobalt-free triple-conducting cathode for protonic ceramic fuel cells operating at reduced temperatures. J Mater Chem A Mater *10*, 5381–5390. 10.1039/d1ta10652j.
14. Zhang, Z., Xie, D., Ni, J., and Ni, C. (2021). Ba2YCu3O6+δ-based cathode material for proton-conducting solid oxide fuel cells. Ceram Int *47*, 14673–14679. https://doi.org/10.1016/j.ceramint.2021.01.242.
15. Ni, H., Yang, Y., Tian, Y., Wang, X., Shen, S., Zheng, K., Khan, M., Wang, S., and Ling, Y. (2021). Novel dual-phase symmetrical electrode materials for protonic ceramic fuel cells. J Mater Sci *56*, 19651–19662. 10.1007/s10853-021-06531-8.
16. Bello, I.T., Yu, N., Song, Y., Wang, J., Chan, T., Zhao, S., Li, Z., Dai, Y., Yu, J., and Ni, M. (2022). Electrokinetic Insights into the Triple Ionic and Electronic Conductivity of a Novel Nanocomposite Functional Material for Protonic Ceramic Fuel Cells. Small *18*, 2203207. 10.1002/smll.202203207.
17. Hou, J., Qian, J., Bi, L., Gong, Z., and Liu, W. (2015). cathode performance based on proton-conducting. 2207–2215. 10.1039/c4ta04397a.
18. Yuan, R., He, W., Zhang, C., Ni, M., and Leung, M.K.H. (2017). Cobalt free SrFe0.95Nb0.05O3−δ cathode material for proton-conducting solid oxide fuel cells with BaZr0.1Ce0.7Y0.2O3−δ electrolyte. Mater Lett *200*, 75–78. https://doi.org/10.1016/j.matlet.2017.04.103.
19. Chen, C., Dong, Y., Li, L., Wang, Z., Liu, M., Rainwater, B.H., and Bai, Y. (2019). High performance of anode supported BaZr0.1Ce0.7Y0.1Yb0.1O3-δ proton-conducting electrolyte micro-tubular cells with asymmetric structure for IT-SOFCs. Journal of Electroanalytical Chemistry *844*, 49–57. https://doi.org/10.1016/j.jelechem.2019.05.001.
20. Zunic, M., Chevallier, L., Deganello, F., D'Epifanio, A., Licoccia, S., Di Bartolomeo, E., and Traversa, E. (2009). Electrophoretic deposition of dense BaCe0.9Y0.1O3−x electrolyte thick-films on Ni-based anodes

for intermediate temperature solid oxide fuel cells. J Power Sources *190*, 417–422. https://doi.org/10.1016/j.jpowsour.2009.01.046.

21. Bi, L., Fabbri, E., Sun, Z., and Traversa, E. (2011). A novel ionic diffusion strategy to fabricate high-performance anode-supported solid oxide fuel cells (SOFCs) with proton-conducting Y-doped BaZrO3 films. Energy Environ Sci *4*, 409–412. 10.1039/c0ee00353k.